30602

NATIONAL LIBRARY
OTTAWA

BIBLIOTHÈQUE NATIONALE
OTTAWA

NAME OF AUTHOR.....Jun Amano.....

TITLE OF THESIS...Low Energy Ion Beam Deposition
....of Metallic Thin [redacted] Films
.....

UNIVERSITY....of Alberta.....

DEGREE FOR WHICH THESIS WAS PRESENTED.....Ph.D.....

YEAR THIS DEGREE GRANTED.....1976

Permission is hereby granted to THE NATIONAL LIBRARY OF CANADA to microfilm this thesis and to lend or sell copies of the film.

The author reserves other publication rights, and neither the thesis nor extensive extracts from it may be printed or otherwise reproduced without the author's written permission.

(Signed)...Jun Amano.....

PERMANENT ADDRESS:

19-5, Higashimine-machi,
Ota-ku, Tokyo
Japan

DATED.July 14,.....1976

NL-91 (10-68)

INFORMATION TO USERS

THIS DISSERTATION HAS BEEN MICROFILMED EXACTLY AS RECEIVED

This copy was produced from a microfiche copy of the original document. The quality of the copy is heavily dependent upon the quality of the original thesis submitted for microfilming. Every effort has been made to ensure the highest quality of reproduction possible.

PLEASE NOTE: Some pages may have indistinct print. Filmed as received.

Canadian Theses Division
Cataloguing Branch
National Library of Canada
Ottawa, Canada K1A 0N4

AVIS AUX USAGERS

LA THESE A ETE MICROFILMEE TELLE QUE NOUS L'AVONS RECUE

Cette copie a été faite à partir d'une microfiche du document original. La qualité de la copie dépend grandement de la qualité de la thèse soumise pour le microfilmage. Nous avons tout fait pour assurer une qualité supérieure de reproduction.

NOTA BENE: La qualité d'impression de certaines pages peut laisser à désirer. Microfilmee telle que nous l'avons reçue.

Division des thèses canadiennes
Direction du catalogage
Bibliothèque nationale du Canada
Ottawa, Canada K1A 0N4

THE UNIVERSITY OF ALBERTA

LOW ENERGY ION BEAM DEPOSITION OF METALLIC THIN FILMS

by

© JUN AMANO

A THESIS

SUBMITTED TO THE FACULTY OF GRADUATE STUDIES

AND RESEARCH IN PARTIAL FULFILLMENT OF THE REQUIREMENTS

FOR THE DEGREE OF DOCTOR OF PHILOSOPHY

DEPARTMENT OF ELECTRICAL ENGINEERING

EDMONTON, ALBERTA

FALL, 1976

THE UNIVERSITY OF ALBERTA

FACULTY OF GRADUATE STUDIES AND RESEARCH

The undersigned certify that they have read, and recommend to the Faculty of Graduate Studies and Research, for acceptance, a thesis entitled LOW ENERGY ION BEAM DEPOSITION OF METALLIC THIN FILMS submitted by JUN AMANO in partial fulfillment for the requirements for the degree of DOCTOR OF PHILOSOPHY.

Ronald P.W. Lawson
Supervisor

Douglas M. Sheppard

External Examiner

Date 12 July 1976

ABSTRACT

In order to improve thin film characteristics, such as, purity, adhesion and crystalline structure, for the application to high power laser optical coatings, an innovative thin film deposition method was developed. A low energy ion beam deposition system which permits precise control of deposition parameters was designed and constructed. Performance data are given for gaseous ion beams and ion beam deposited Pb and Mg films. The deposits were analyzed by Rutherford Backscattering analysis, transmission electron microscopy, scanning electron microscopy and X-ray diffraction analysis.

Both Pb and Mg films show the dependence on incident particle energy for their adhesion, thickness, surface coverage, and crystalline structure.

More controlled film characteristics are obtained by this deposition method than that of conventional deposition methods. The main characteristics of the films obtained by low energy ion beam deposition are as follows:

(1) Strong adhesion at higher deposition energies

(2) Pure homogeneous films

(3) Good surface coverage

(4) Oriented crystalline structure at higher deposition energies

Most importantly, the precise controllability of the deposition parameters and consequently precise control of film characteristics for specific applications, makes this technique a viable alternative to present film deposition methods.

Acknowledgments

The author wishes to thank his supervisor, Dr. R.P.W. Lawson, for his encouragement during the research work, and for his constructive criticisms and discussions during the writing of the present thesis.

The author would like to express his appreciation to the following people.

Dr. P. Bryce, for his initial design and construction of the system.

Mr. R. Schmaus, for construction of electronic systems.

Dr. G.C. Neilsen and researchers at the Nuclear Research Center, for use of the Van de Graaff Accelerator and experimental assistance with RBS analysis.

Dr. R. Henderson, for use of the TEM.

Dr. H. Seguin, for use of the X-ray diffractor.

Mr. G. Braybrook, for the SEM experiments.

The members of the machine shop headed by Mr. K. Doerrbecker, for their excellent craftsmanship.

Dr. W.A. Grant of the University of Salford and Dr. J.A. Davies of CRNL, for helpful correspondence.

The National Research Council of Canada and the University of Alberta, for financial support.

Ms. Barbara J. Gallaiford, for excellent typing of the manuscript.

Finally, the author wishes to thank Dawne Touchings for her patience and encouragement during this work and also for her proof-reading of the manuscript.

Table of Contents

Chapter		Page
1.	Introduction	1
	1.1 Background	1
	1.2 Conventional Thin Film Deposition Methods	3
	1.2.1 Vacuum Evaporation	3
	1.2.2 Sputter Deposition	8
	1.2.3 Ion Plating	9
	1.3 Present Study	12
2.	Low Energy Ion Beam Deposition Processes	14
	2.1 Introduction	14
	2.2 Phenomena During Collision Processes	15
	2.2.1 Secondary Electron Emission	15
	2.2.2 Sputtering	15
	2.2.3 Penetration and Damage	18
	2.3 Collision Model	18
	2.3.1 Interatomic Potential	20
	2.3.2 Collision Time	23
	2.3.3 Collision in the Center of Mass System	25
	2.4 Conclusions	29

Chapter		Page
3.	System Specification and Design	32
	3.1 Design Criteria	32
	3.1.1 Vacuum Requirements	33
	3.1.2 Ion Beam Requirements	35
	3.2 Deposition System	39
	3.2.1 Vacuum System	39
	3.2.2 Ion Beam System	44
	A. Ion Source	47
	B. Velocity Filter	52
	3.2.3 Substrate Chamber	57
	3.3 Substrate Preparation System and Storage System	66
	3.4 Conclusions	71
4.	Low Energy Ion Beam Deposition of Pb and Mg Thin Films and Analysis of Deposits	72
	4.1 Introduction	72
	4.2 Analytical Methods	74
	4.2.1 Composition Analysis	74
	4.2.2 Surface Structure Analysis	77
	4.2.3 Crystalline Structure Analysis	79

Chapter			Page
	4.3	Pb^+ Ion Beam Deposition and Analysis of Deposits	82
		4.3.1 Low Energy Pb^+ Ion Beam Deposition	83
		4.3.2 RBS and SEM Analyses	87
		4.3.3 TEM Analysis	98
	4.4	Mg^+ Ion Beam Deposition and Analysis of Deposits	103
		4.4.1 Low Energy Mg^+ Ion Beam Deposition	103
		4.4.2 RBS and SEM Analyses	107
		4.4.3 X-ray Diffraction Analysis	117
	4.5	Conclusions	118
5.		Limitations of Present System	123
	5.1	Limitations Due to the Nature of Deposition Method	123
	5.2	Limitations Due to the System	123
	5.3	Conclusions	127
6.		Conclusions	128
References			131
Appendix			143

List of Figures

Figure	Description	Page
1.1 (a)(b)(c)	Vapour pressure curves for the common elements [14]	5
2.1	Total electron emission yield for various ion energy on atomically clean surface [9, 10]	17
2.2	Self-sputtering yield for different atomic number of target by 45KeV ions [13]	19
2.3 (a)(b)	Self-sputtering yield at low ion energy [14]	19
2.4	General diagram of the interatomic potential	21
2.5	Interatomic potential of Cu for several common approximations [18]	21
2.6 (a)(b)(c)	Hard sphere collision model in (a) the laboratory system, (b) the center of mass system, and (c) the kinematics of velocity vector in the two systems	26
2.7	Average energy transfer and average retained energy for a carbon substrate	30
3.1	Required partial pressure of residual gases to produce pure films	36

Figure	Description	Page
3.2	General guide for space-charge effect [6]	38
3.3	Schematic diagram of differential pumping system	40
3.4	Schematic diagram of vacuum system (after A.V.S. standard 7.1 - 1966)	43
3.5 (a)	Low energy ion beam deposition system	45
(b)	Photograph of the low energy ion beam deposition system	46
3.6	Block diagram of the system electronics	48
3.7	Modified plug-in ion source and furnace	50
3.8	Schematic diagram of velocity filter	53
3.9	Mass selection of velocity filter	55
3.10	Substrate chamber configuration	58
3.11	Block diagram of data handling system	59
3.12	Typical 4 KeV ion beam profiles at substrate	61
3.13	Ion beam current cut-off characteristics	63
3.14	Space-charge expansion of Pb^+ ion beam	65
3.15	Photograph of substrates and substrate holders	67
3.16	Schematic diagram of a carbon arc evaporation system	69

Figure	Description	Page
3.17	Schematic diagram of a substrate storage system	70
4.1	Schematic diagram of the RBS system together with the data handling system	78
4.2	Schematic representation of electron scattering and diffraction pattern [10]	80
4.3	Pb deposit width as a function of incident ion energy	85
4.4	RBS spectrum of freshly-deposited 48eV Pb film	88
4.5	RBS spectra of center of Pb deposits	90
4.6 (a)(b) (c)(d)	Surface topographs of the center Pb deposits (a) 24eV, (b) 48eV, (c) 72eV, and (d) 121eV deposition energies	93
4.7	RBS scan of the 48eV Pb deposit	95
4.8 (a)(b)(c)	Surface topography of 48eV Pb deposit for various distances from deposition center. (a) deposition center, (b) 2mm off-center and (c) 4mm off-center	97
4.9 (a)(b)(c)	Electron diffraction pattern of (a) carbon thin film, (b) 48eV Pb on C film and (c) 121eV Pb on C film	99

Figure	Description	Page
4.10(a)(b)(c)	Electron diffraction pattern of (a) 24eV Pb on NaCl, (b) 48eV Pb on NaCl and (c) 121eV Pb on NaCl	100
4.11	Mg deposit width as a function of incident ion energy	106
4.12	RBS spectra of center of Mg deposits	109
4.13(a)(b)(c)(d)	Surface topography of the center of Mg deposits. (a) 24eV, (b) 48eV, (c) 100eV, and (d) 150eV deposition energies	113
4.14(b)(b)(c)	Surface topography of 24eV Mg deposits for various distances from deposition center, (a) deposition center, (b) 2mm off-center and (c) 4mm off-center	115
4.15(a)(b)(c)	Surface topography of 100eV Mg deposits for various distances from deposition center, (a) deposition center, (b) 2mm off-center, and (c) 4mm off-center.	116
4.16(a)(b)	X-ray diffraction pattern of (a) carbon substrate and (b) 100eV Mg deposit on same substrate	119
5.1	Plug-in ion source combined with furnace	125

List of Tables

Table	Description	Page
1.1	Comparison of thin film deposition methods	4
2.1	Main phenomena occurring during low energy ion beam deposition	16
2.2	Born-Mayer constants [20]	22
3.1	Estimated vacuum parameter	42
3.2	Detailed description of system power supply	49
3.3	Vaporization temperature of elemental metals	52
4.1	Properties of Lead (Pb) and Magnesium (Mg)	73
4.2	Operational condition for Pb^+ ion beam deposition	82
4.3	Statistical nature of Pb^+ deposition and analysis of deposits	84
4.4	Density and thickness of Pb deposits	89
4.5	Operational condition for Mg^+ ion beam deposition	103
4.6	Statistical nature of Mg^+ deposition and analysis of deposits	104
4.7	Density and thickness of Mg deposits	108

Chapter 1

Introduction

1.1 Background

A serious problem in the development and application of high-power lasers is damage to optical interfaces. This damage to optical interfaces generally determines the limit of laser performance [1]. Limitations to the properties of optical interfaces such as weak absorption, the presence of inhomogeneities or nonlinear susceptibility, are negligible for low-power lasers, but these limitations can cause catastrophic failure of interface materials in high-power laser systems.

Laser optical interfaces, the reflecting mirrors and the output windows, generally consist of dielectric or metallic coatings of single or multi-layer thin films. Thin films are mainly produced by deposition of film materials by vacuum evaporation or by sputter deposition onto a substrate of suitable materials.

As thin film technology has advanced, film characteristics such as purity, defect concentration, adhesion, and the range of materials that can be deposited in thin film form have been improved by various deposition techniques. Vacuum evaporation, the various modes of sputter deposition, and ion plating have been well documented as to their suitability for a wide range of thin film applications [2-5].

Inherent in the operation of such techniques is the inclusion of undesirable foreign impurities within the film [6-9]. These impurities

can originate at the source of the depositing particles; they can be desorbed from the walls of the enclosure, or they can be already present in the gas phase within the enclosure. Another disadvantage of "conventional" techniques is that the energy of the depositing particles is uncontrollable. In fact, using present techniques it is difficult, if not impossible, to independently control the many factors such as adhesion, sputtering, film damage, and purity that can affect film growth processes. Although those conventional techniques are perfectly adequate for most applications, certain critical processes, such as thin film coatings for high power laser optics, have not yet been perfected.

By further improvement of thin film characteristics, it would be possible to produce high-power laser optical interfaces which will withstand higher energy radiation.

Film characteristics can be improved by more precise control of deposition conditions. Most of the conventional methods use materials which may be in a neutral state, excited state, ionized state, or combinations of those. By selecting one particular state and manipulating the condition of the incoming material while it is in that state, more precise control of deposition parameters can be achieved. Ionized material may be easily controlled by manipulation of electric and magnetic fields.

When a low energy metallic ion beam impinges onto a substrate, deposition of material from the beam occurs [10-13]. When compared with conventional thin film deposition methods, this approach has the potential for controlling the above mentioned factors.

The purpose of this thesis is to present a theoretical analysis, an actual system design and the performance results of a novel thin film deposition method which utilizes low energy ion beams.

1.2 Conventional Thin Film Deposition Methods

The modern methods for thin film deposition are classified into two groups: physical methods and chemical methods. Physical methods include the deposition techniques which depend on evaporation or sputtering mechanism. On the other hand, chemical methods depend on a specific chemical reaction. In the following section only physical deposition methods which employ modern high vacuum technology are reviewed.

The physical deposition methods are broadly classified into three groups, (1) vacuum evaporation, (2) sputter deposition, and (3) combinations of (1) and (2), i.e. ion plating. The typical characteristics of those techniques are compared in Table 1-1.

1.2.1 Vacuum Evaporation

Vacuum evaporation is the most widely used technique for thin film fabrication. A very large number of solid materials can be vaporized by heating to sufficient temperatures. The vapour pressure curves for the common elements are shown in Figure 1-1 [14]. The condensation of the vapour onto a cooler substrate yields thin solid films. Detailed review of the vacuum evaporation is well documented in several sources [15, 16].

In vacuum evaporation, typical operational pressures are in the order of 10^{-6} Torr to ensure a straight-line path for vapour atoms. Thermal evaporation of solid materials can be achieved by direct or

Table 1.1

Comparison of Thin Film Deposition Methods

	(Torr) Vacuum Environment*	Incident Particle	Particle Energy	Particle Mass	Adhesion
Thermal Evaporation	$\sim 10^{-6}$	Atoms Molecules	Thermal Energy uncontrollable	Unselected	Fair
Sputtering	$10^{-1} \sim 10^{-6}$	Atoms Molecules	< 10eV uncontrollable	Unselected	Good
Ion Plating	$10^{-1} \sim 10^{-6}$	Atoms Molecules Ions	Variable Uncontrollable	Unselected	Excellent
Ion Beam Deposition	10^{-8}	Ions	Variable Controllable	Selected	Excellent (expected)

* During Deposition

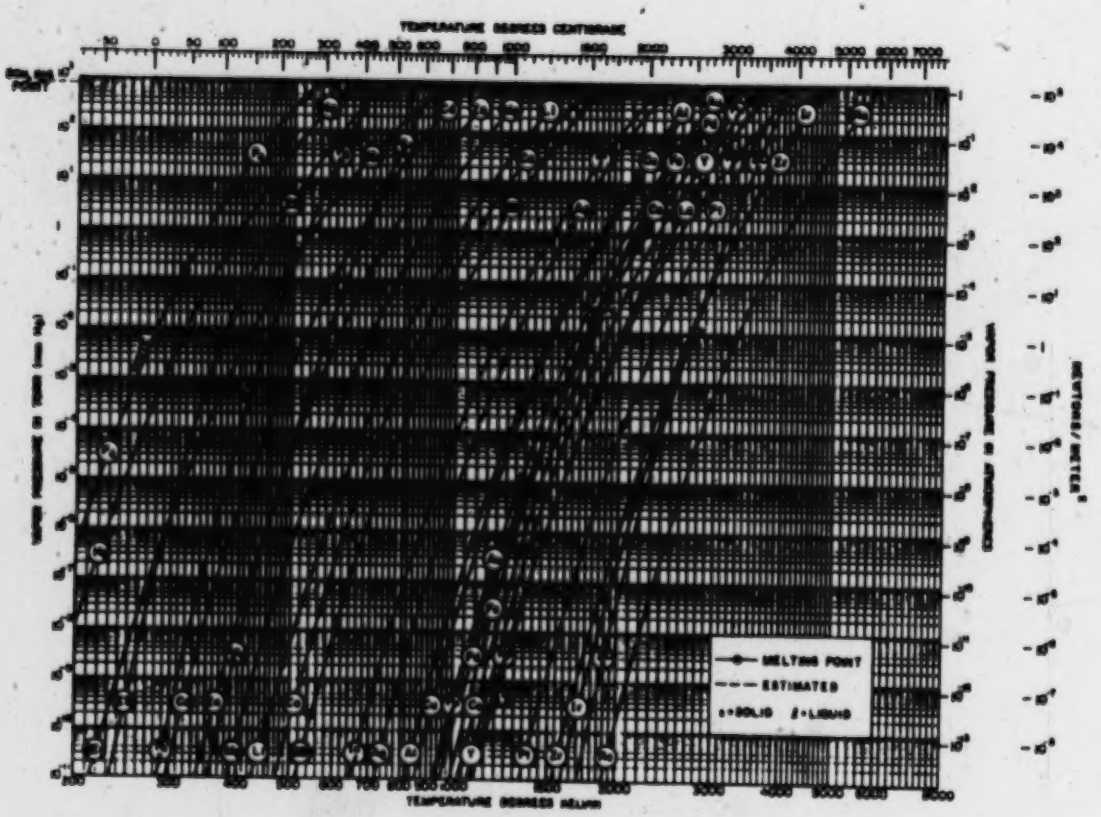

(A)

Figure 1.1 Vapour psesuure curves for the common elements (14)

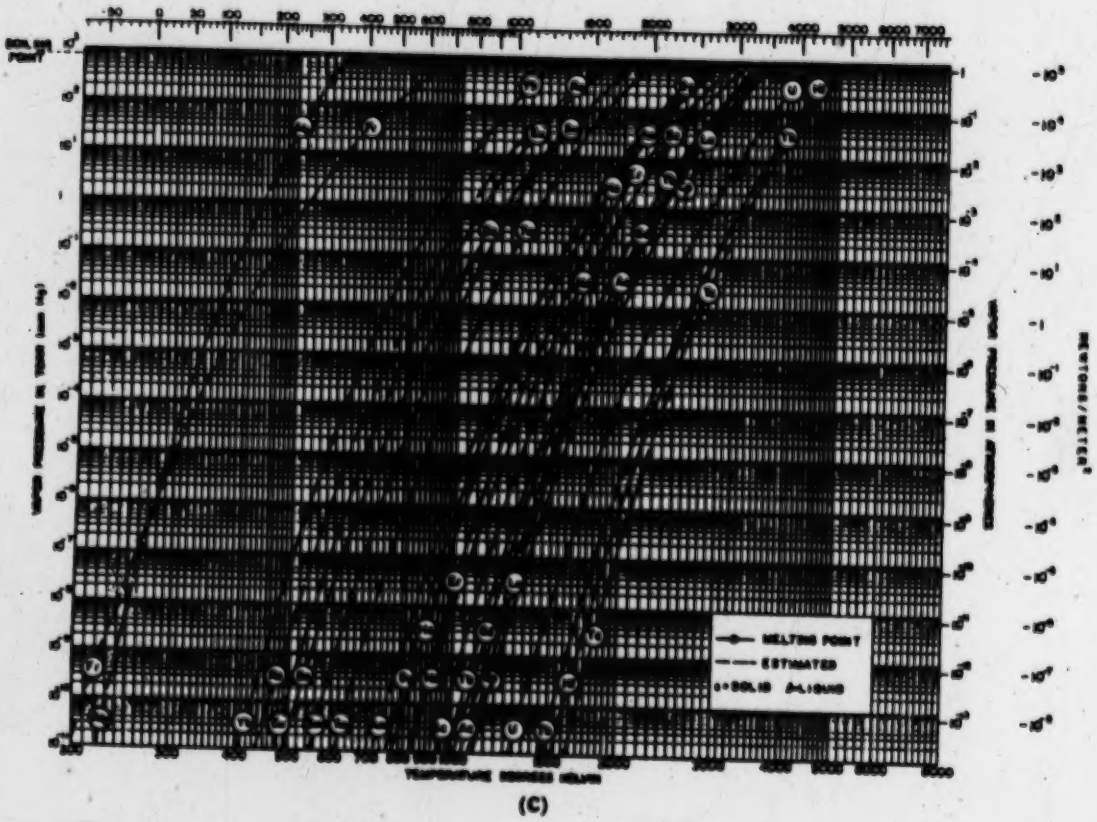

(C)

Figure 1.1

Figure 1.1

indirect heating, for example resistive heating and electron-bombardment heating.

By adaptation of UHV techniques and the e-beam evaporation method, a working pressure of $\sim 10^{-8}$ Torr is possible [9]. However, in vacuum evaporation techniques, the shadowing effect and possible contamination from the source or support materials can not be avoided.

1.2.2 Sputter Deposition

Sputtering is a process by which a surface of a material (target) is bombarded with particles of a sufficient energy to cause ejection of a surface atom. The ejected or sputtered atoms can be condensed onto a substrate surface, and the formation of a thin film will commence.

In addition to the ejection of surface atoms, secondary electrons are ejected from the substrate surface by the impact of bombardment. These free electrons can be accelerated in an electric field to cause further ionization of the residual gas and such ionization will result in further bombardment of the target surface, and a self-sustaining reaction will occur. Various modes of sputtering deposition systems, such as, glow discharge, reactive, getter, bias and R.F. sputtering, are based on this effect. The above sputtering deposition method typically require 20 to 100m Torr Argon pressure range to maintain the self-sustaining effect. In order to operate in a low pressure range, the increasing supply of ionizing electrons (triode and R.F. supported sputtering) or the use of a separate ion beam source (ion beam sputtering) is commonly used. Typical operational pressure of $\sim 10^{-5}$ Torr can be achieved by the above methods.

The application of sputtering to thin film deposition is well documented in several articles [17, 18]. The most recent ion beam sputtering method combined with ion milling has become one of the most important methods owing to the controllability of deposition parameters [19, 20].

The main advantages of sputter deposition as compared to vacuum evaporation are as follows:

(1) uniform coating for large and/or complex surface, because a large area deposition source (sputtering target) can be used rather than a point source;

(2) deposition of alloy and multicomponent films, because the composition of a sputtered film will often be the same as that of a sputtered target;

(3) good adhesion, because the substrate surface can be sputter-cleaned before deposition and/or because of the reactive nature of the sputtering environment;

(4) low temperature epitaxy, because the high energy flux can be provided to the substrate surface by the high energy electron bombardment.

The main disadvantage of sputter deposition is that the deposition rates are lower than that of vacuum evaporation because of the nature of the sputtering processes.

1.2.3 Ion Plating

Ion Plating, the third technique of vacuum deposition, was developed more recently than vacuum evaporation and sputter deposition.

Ion plating is a so-called "hybrid" technique which combines vacuum evaporation and sputter deposition. It has same advantages as those of sputter deposition and also the advantage of having a relatively high deposition rate.

In ion plating the substrate surface is subject to a high energy ion beam sufficient to cause sputtering before and during film formation. Usually, ion plating is carried out in a DC glow discharge system with a high negative voltage cathode substrate. The substrate is bombarded by energetic ions created by a gaseous discharge for a time sufficient to sputter-clean the surface contamination prior to the deposition of film material. The film material is thermally evaporated into a gaseous discharge, and some film atoms are ionized. The depositing particles at the substrate surface are considered to be [21];

(1) some of the energetic particles penetrate into the substrate surface;

(2) some are sputtered back to vacuum;

(3) some remain to begin film formation.

The glow discharge mode of ion plating is typically operated in a high pressure region (10^{-3} to 10^{-1} Torr). By adaptation of e-beam evaporation techniques, a wide range of materials can be deposited [22-25].

In order to reduce residual gas incorporation into the thin films, low pressure mode (10^{-6}-10^{-4} Torr) ion plating techniques have been developed, by using an ionization filament [26], RF coil [27],

combinations of ionization filament and RF coil [28], and external ion beam sources [29, 30].

Even for the improved mode of ion plating there are a number of unknowns in the process of film formation:

(1) Percentage of ionization of the depositing materials.

(2) Energy of the depositing particles.

(3) Degree of ionization of the depositing particles - singly charged or multiply charged ions.

(4) Species of the depositing materials.

If deposition is carried out by the ion beam, itself, which is extracted from the ion source by various extraction voltages, the depositing material will consist of only ionized material, and the energy of the depositing particles can be determined precisely. Furthermore, if a one mass ion beam with a single mass to charge ratic is chosen, the deposition of homogeneous films with known energy, charge state and mass can be achieved.

All preceeding conditions are satisfied in the present study of the low energy metallic ion beam deposition method. In this method, the ion beam is extracted from the separate ion source with various extraction voltages. The extracted ion beam is mass-separated and mass-selected by a velocity filter and is deflected toward the substrate. The depositing materials consist of homogeneous ion beams with known energy and mass.

If the ion plating is defined as the process in which film deposition and ion bombardment take place at the same time, the present study of low energy ion beam deposition method can be

classified as an elaborate mode of ion plating.

1.3 Present Study

The purpose of the present study is to design, to construct and to analyze the performance of a low energy ion beam depostion system. The system as designed and constructed not only has the advantages of ion plating including: the ability to sputter-clean of the substrate surface, provision of a high energy flux to the substrate surface by ion bombardment, possible physical mixing of the film material with the substrate surface, and increase of nucleation density of thin films [5], but also achieves minimization of residual gas incorporation by UHV techniques, homogeneity of the incident particle by mass separator, and controllability of the incident particle energy.

Chapter 2 reviews the processes which occur during low energy solid ion bombardment onto a solid substrate.

In Chapter 3, the design criteria necessary for the construction of the low energy ion beam deposition system is discussed. Following the specification of the system, the construction and performance tests of the system are described.

Chapter 4 describes Pb^+ and Mg^+ ion beam deposition and analysis of deposits by various diagnostic methods, such as, Rutherford Backscattering analysis, electron microscopy analysis, and x-ray diffraction analysis.

In Chapter 5, the limitations of the present system and possible solutions for those limitations are described.

Chapter 6 summarizes the present study. Advantages of the low

energy ion beam deposition method compared with existing deposition methods are discussed.

Chapter 2

Low Energy Ion Beam Deposition Processes

2.1 Introduction

The processes that will occur during low energy solid ion beam deposition are:

1) when an energetic ion approaches a conductive substrate surface, electron capture or electron emission will occur and consequently the incident ion will be neutralized;

2) the neutralized ion (energetic atom) will then lose its kinetic energy by collision with a substrate atom or atoms. It is assumed that this collision is elastic because of low incident particle energy. If the incident particle energy is sufficiently large, the sputtering of a substrate atom or surface damage will occur;

3) after losing its kinetic energy, the incident atom will be adsorbed on the substrate surface or entrapped into the sub-surface;

4) adsorbed adatoms will diffuse over the surface and film nucleation and growth will start to take place;

5) after the initial coverage of the surface by adatoms, the above process will be repeated by atoms of the same species, and the self-sputtering effect becomes the most influential factor for further film growth.

Some of the above phenomena are well investigated by various researchers [1-7]. In this chapter, each phenomenon which occurs

during low energy ion beam bombardment is briefly reviewed. A theoretical collision model which is suitable for low energy ion beam deposition is outlined after these phenomena are reviewed.

2.2 Phenomena During Collision Processes

The main phenomena which are believed to be occurring during low energy ion beam deposition are summarized in Table 2.1.

2.2.1 Secondary Electron Emission

For ion energies <1keV, the secondary electron emission process is governed by potential emission. In this process, an electron tunnels from the conduction band of the solid surface to an unfilled state of the incident ion. As a result the ion is neutralized and a second electron is sufficiently excited to be emitted to vacuum [8]. This process is shown to be almost independent of the kinetic energy of the incident particle but is dependent on its potential energy of excitation. Figure 2.1 shows examples of total electron yield with low incident ion energy [9,10]. The electron emission yield decreases as the mass of the incident ion increases.

2.2.2 Sputtering

Sputtering, the ejection of atoms of a solid by energetic atoms or ions, has been very intensively studied [11,12]. Sputtering yields strongly depend on the following factors: ion energy, ion species, ion charge, target materials and directional effect.

For the ion beam deposition, the self-sputtering, that is sputtering of a target with ions of the same element, govern the film build-

Energy	Collision Model	Secondary Electron Emission	Sputtering	Penetration	Surface Damage
25-500eV	binary	potential emission yield: $10^{-1} \sim 10^{-2}$	linear increase yield: ~ 1 at 500eV	a few lattice constant• up to 10A	up to tens of vacancy and inter-stitial

Table 2.1 Main Phenomena Occurring During Low

Energy Ion Beam Deposition

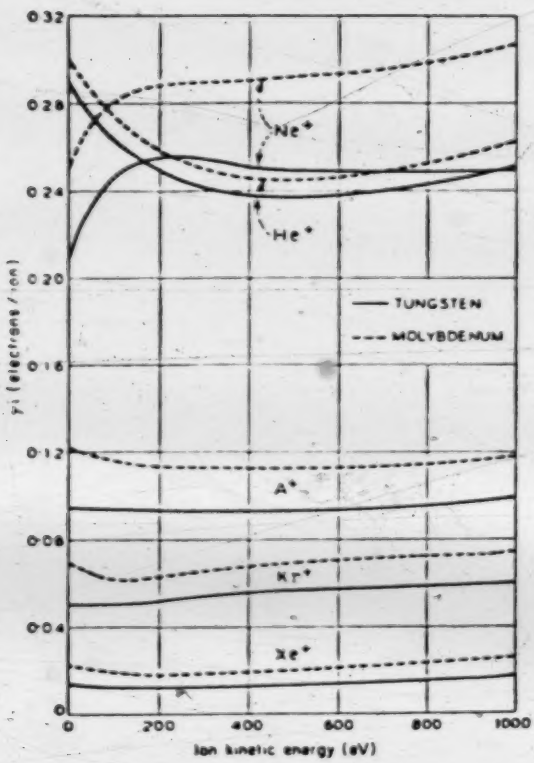

Figure 2.1 Total electron yield for low ion energy on atomically clean surface. (9,10)

up process. But it is known that self-sputtering is not in principle different from other sputtering processes.

The following figures show the self-sputtering yeild for various atomic numbers of the target by 45keV ions [13], Figure 2.2, and the self-sputtering yield at low ion beam energy [14], Figure 2.3(a), (b).

2.2.3 Penetration and Radiation Damage

After the initial collision, a incident particle looses its kinetic energy and is deflected into a new trajectory. It may then travel some distance before another collision with a lattice atom. During the collision processes, if the transferred energy from the incident particle to the lattice atom exceeds the lattice binding energy (typically $\sim$ 25eV [15]), radiation damage will take place. After the collisions, if the remaining energy of the incident particle still exceeds the lattice binding energy, farther penetration will occur. It is extremely difficult to measure the penetration depth for low energy incident particle. However, the mean range of 500eV, X_e^+ in W was measured at approximately 5Å [16].

Because of the extremely small penetration, the damage is confined to a thin layer of the solid surface. In general, light mass particles can penetrate the solid without causing damage; on the other hand, the heavy mass particles can produce damage and collision sequences without deep penetration into a solid [17].

2.3 Collision Model

There are two basic problems in formulating low energy atomic collision mechanisms.

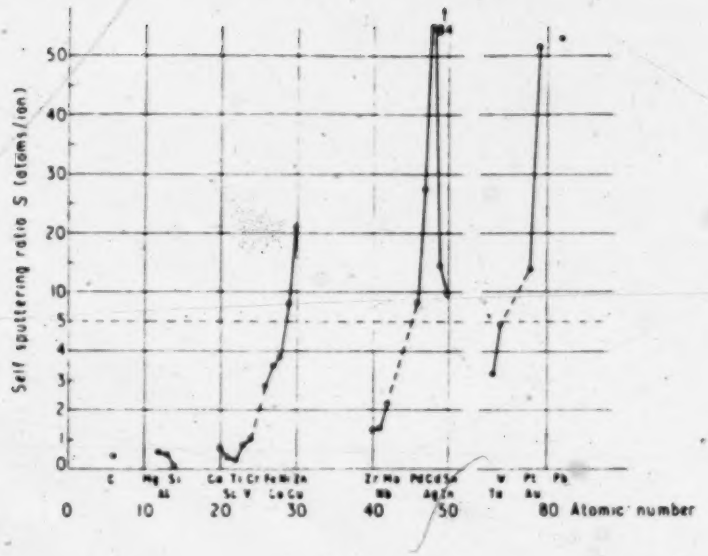

Figure 2.2 Self-sputtering yield versus atomic number of target by 45 KeV ions (13).

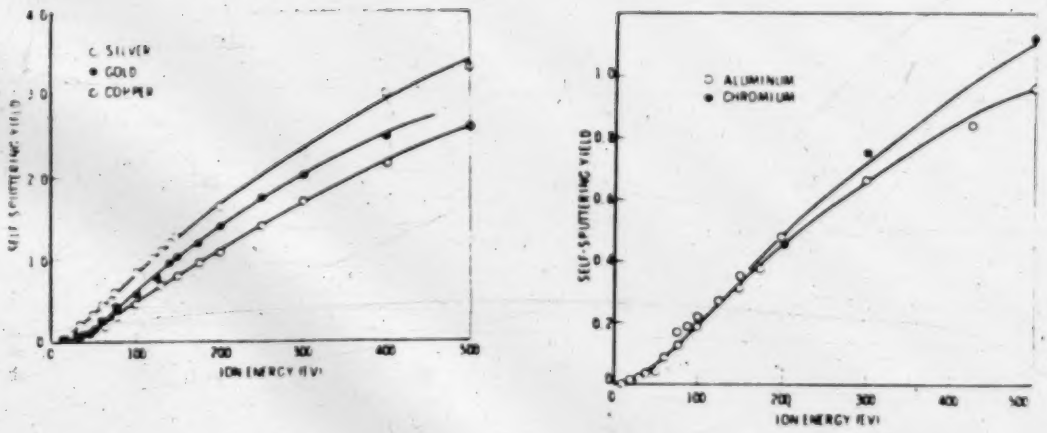

(a) (b)

Figure 2.3 Self-sputtering yield at low ion energy (14).

(1) a suitable choice of the interatomic potential,

(2) a suitable choice of a collision model, i.e. either binary collision or a multi-body collision.

2.3.1 Interatomic Potential

At this time, a definite analytical expression for the interatomic potential which is valid for all interaction distances does not exist. The general form of interatomic potential is shown in Figure 2.4. This potential is considered to be composed of two forces. For large atomic separation, the attractive Coulomb force is dominant. On the other hand, for small atomic separation, the central field repulsive force is dominant. The repulsive force varies substantially with the interatomic distance. The former force represents the crystal binding force and the latter the interaction potential force.

Figure 2.5 shows several approximations of the interatomic potential of the repulsive force [18]. For relatively large interatomic separation, the Born-Mayer potential is most suitable, and for small separation, the Coulomb potential is suitable.

Therefore, for a low energy atomic collision mechanism, the Born-Mayer potential can be considered to be most satisfactory at present. This potential is written as

$$V(r) = A \exp \left[\frac{-r}{a} \right] \text{ eV}$$

where A, a are constant.

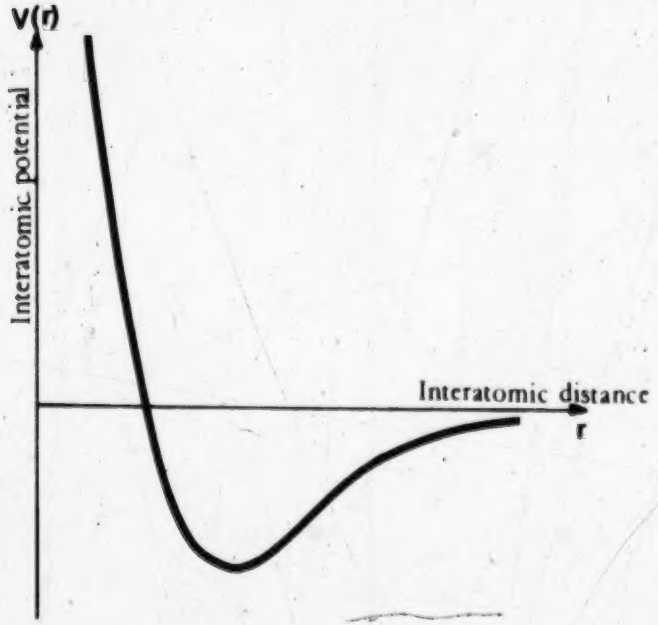

Figure 2.4 General diagram of the interatomic potential.

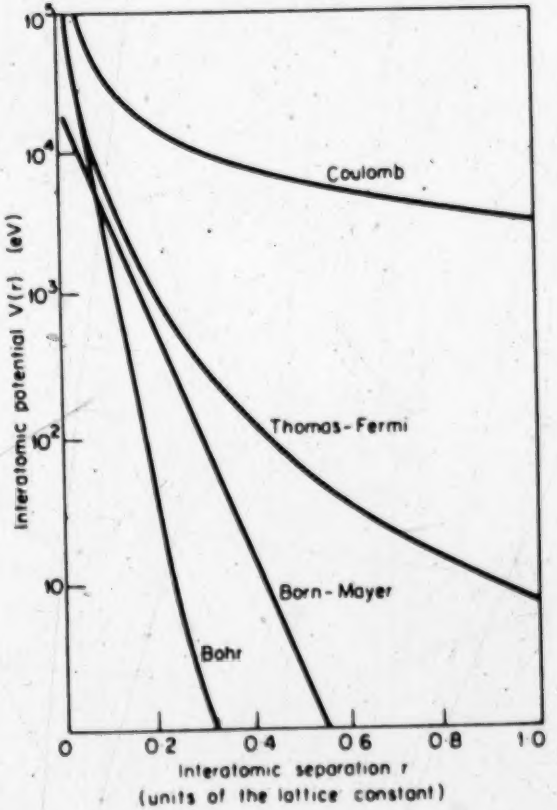

Figure 2.5 Interatomic potential of copper for several common approximation (18).

Atomic Number Z	Element	A(eV)	$\frac{1}{a}$ ($\mathring{A}^{-1}$)
6	C	1316.1	3.80959
12	Mg	3829.0	3.69813
29	Cu	13919	3.56137
47	Ag	28318	3.52735
50	Sn	31025	3.52458
79	Au	59473	3.49989
82	Pb	62904	3.50092

Table 2.2 Born-Mayer Constants [20].

A and a are determined from the elastic moduli and their dependance on pressure and shock waves [19]. Recently the values of A, a have been calculated by using the Thomas-Fermi-Dirac (TFD) approximation for nearly every element [20]. Table 2.2 lists values for A and a of few elements.

2.3.2 Collision Time

If the lattice has sufficient time to dissipate energy during collision, the binary collision model is valid. In other words, if the collision time is much shorter than that of the lattice vibration, the low energy atomic collisions are considered to be two body events [21].

In the following passage, the collision time under the influence of the Born-Mayer potential is investigated.

For a Born-Mayer interaction, the energy loss, ΔE, and the total transferred momentum, ΔP, due to the interaction potential can be calculated by first order perturbation theory (momentum approximation) [10], if E is very small compared to the projected energy.

The total transferred momentum ΔP is given as [10] :

$$\Delta P = \frac{2A}{v_0}\sqrt{\frac{\pi p}{2a}}\, e^{\frac{-p}{a}} \qquad \text{for } \frac{p}{a} \gg 1$$

where $v_0 = \sqrt{\frac{2E_0}{m_0}}$

m_0 = projectile mass

E_0 = projectile energy

p = impact parameter - closest approach distance

Then,

$$\Delta P = A \sqrt{\frac{2m_0}{E_0}} \sqrt{\frac{\pi}{2} \frac{p}{a}} e^{-\frac{p}{a}}$$

The collision time is defined as [10].

$$\Delta t = \frac{\Delta P}{F_{max}}$$

where $F(r)_{max}$ is the force at closest approach i.e.

$$F(r)_{max} = \frac{A}{a} e^{-\frac{p}{a}} \quad \text{at} \quad r = p$$

therefore,

$$\Delta t = \sqrt{\frac{m_0}{E_0}} \sqrt{\pi a p}$$

or

$$E_0 = \frac{\pi m_0 a p}{(\Delta t)^2}$$

The collision time for the incident particle of 10eV energy can be estimated using the above equation. Assuming:

$a \sim 0.28\mathring{A}$ (from Table 2.2)

$p \sim 2\mathring{A}$ (one half of typical lattice constant)

$m_0 \sim 100 \times 1.66 \times 10^{-27}$ kg

then

$\Delta t \sim 1 \times 10^{-14}$ sec.

The period of the lattice vibration is roughly $\sim 10^{-13}$ sec [23], which corresponds to an energy loss of 7eV. If the incident particle energy is bigger than 10eV, namely, the collision time is much shorter than that of the lattic vibration, the effects of the lattice vibration on the collision events are negligible. Therefore, the collisions become isolated two-body events. The energy loss due to the interaction potential is also very small for low energy collision.

Consequently, for the ion energy range of ion beam deposition (25eV - 500eV), the simple two-body hard sphere collision model with the impact parameter $p = 2R$ can be used to evaluate the amount of energy transferred or remaining with each collision partner.

2.3.3 Collision in the Center of Mass System

The two-body collision system (Laboratory System) is further simplified by the mathematically equivalent center of mass system, Figure 2.6. In the laboratory system, the incident particle, M_0, is deflected by an angle, θ_L, and the struck particle, M_1, will move off at a certain angle. The deflection angle and velocities after collision depend on the masses of the incident and struck particles

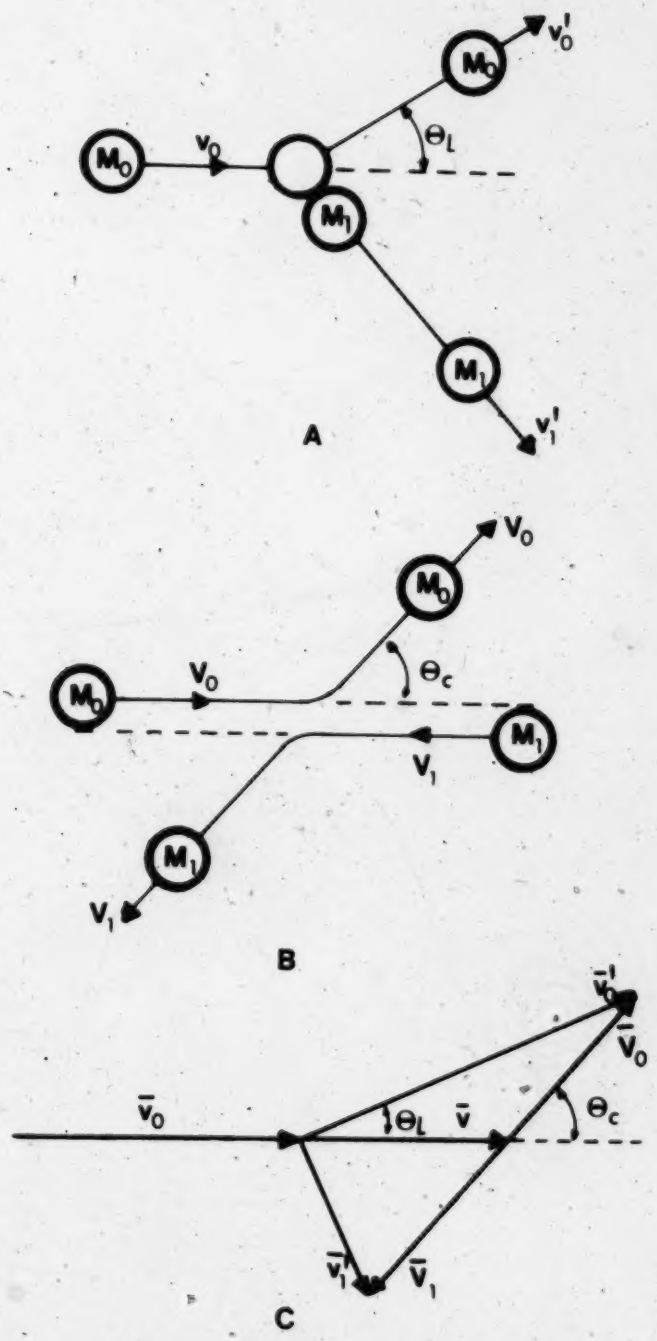

Figure 2.6 Hard sphere collision model in (a) the laboratory system, (b) the center of mass system, and (c) kinematics of velocity vectors in the two systems.

respectively and on incident particle energy E_0. On the other hand, in the center of mass system, the two particles always have equal and opposite momenta. For an elastic collision, the kinetic energy remains constant, and all four momenta (incoming and outgoing) are equal in magnitude. Therefore, each particle leaves the collision at the same velocity with which it arrived. These velocities are:

$$V_0 = \frac{M_1}{M_0 + M_1} v_0 , \quad V_1 = \frac{M_0}{M_0 + M_1} v_0$$

In order to find the recoil energy E_2 in the laboratory system, the addition of velocity vectors can be used. Because the two systems are in relative motion with a vectorial velocity ($\bar{v}$) of the center of mass, Figure 2.6 (c). Therefore:

$$v_0'^2 = V_0^2 + v^2 - 2V_0 v \cos(\pi - \theta_c)$$

$$v_0'^2 = \frac{v_0^2}{(1 - A')^2} (1 + A'^2 + 2A' \cos\theta_c)$$

where

$$A' = \frac{M_1}{M_0}$$

similarly

$$(v'_1)^2 = V_1^2 + v^2 - 2V_1 v \cos\theta_c$$

$$(v'_1)^2 = \left(\frac{2v_o}{1 + A'} \sin \frac{\theta_c}{2} \right)^2$$

The energy transfer, T, from the incident particle to the struck particle in collision is then:

$$T = \frac{1}{2} M_0 (v_0 - v_0')^2$$

$$= \frac{1}{2} M_1 (v_1')^2 = \frac{2 M_1 v_0^2}{(1 + A')^2} \sin^2 \frac{\theta}{2}$$

now

$$v_0^2 = \frac{2E_0}{M_0}$$

therefore,

$$T = \frac{4 M_1 M_0}{(M_0 + M_1)^2} E_0 \sin^2 \frac{\theta}{2}$$

The maximum energy transfer is

$$T_m = \frac{4 M_1 M_0}{(M_0 + M_1)^2} E_0 \text{ at } \theta = -\pi$$

and minimum energy transfer is zero,

therefore,

$$T = T_m \sin^2 \frac{\theta}{2}$$

The retained energy, E_2 of the incident particle is,

$$E_2 = E_0 - T$$

$$= E_o\{1 - \frac{4 M_0 M_1}{(M_0 + M_1)^2} \sin^2 \frac{\theta}{2}\}$$

Because all collisions are equally probable, the average energy transfer is simply:

$$T_a = \frac{1}{2} T_m = \frac{2 M_0 M_1}{(M_0 + M_1)^2}$$

Also, the average retained energy is:

$$E_{2a} = E_0 - \frac{1}{2} T_m$$

Figure 2.7 shows T_a and E_{2a} for a carbon substrate as a function of incident energy E_0 for the incident particles of Lead (Pb) and Magnesium (Mg).

2.4 Conclusion

For the ion energy range of ion beam deposition (25eV to 500eV), it is theoretically demonstrated that the two-body hard sphere collision model is valid for an evaluation of the energy transfer mechanism.

The maximum secondary yields by heavy ion bombardment is roughly 0.1 for this energy range. Namely a maximum of 10% of the total ion current at a target is considered to be caused by the secondary

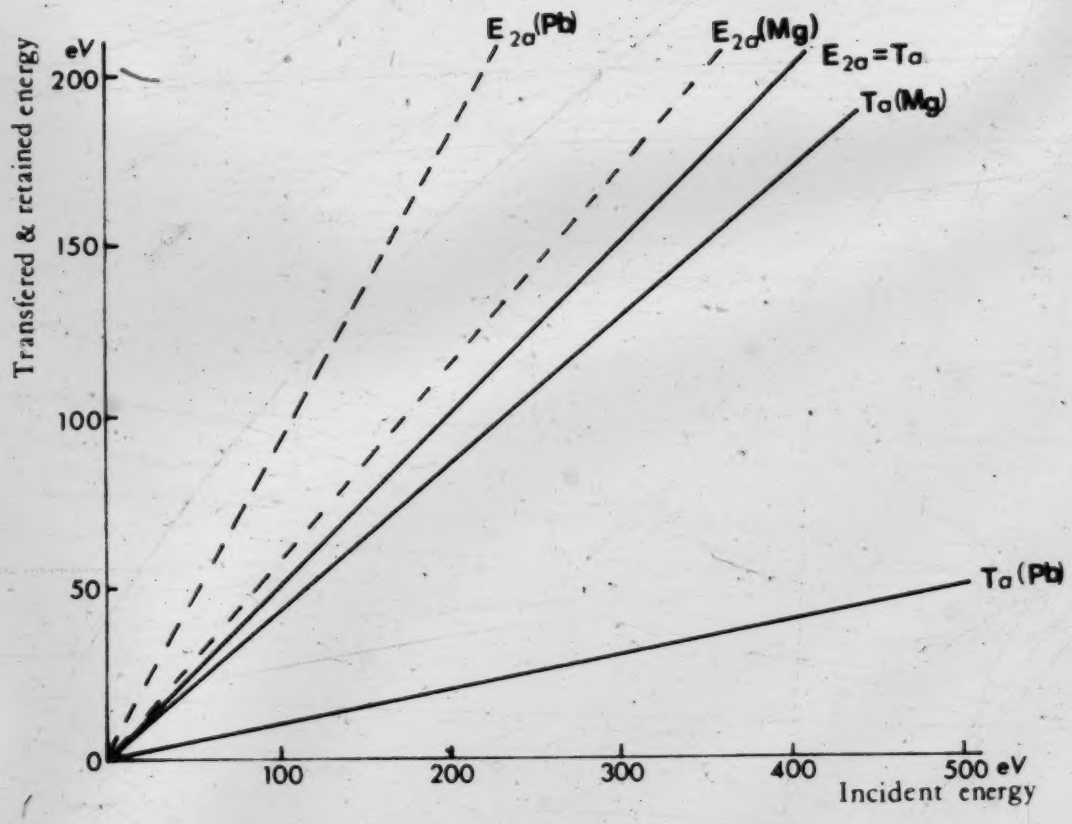

Figure 2.7 Average transfered energy Ta and average retained energy E_{2a} for a carbon substrate.

electron emission.

Self-sputtering yields vary significantly with different materials. For high sputtering yield materials, such as, copper (Cu), Silver (Ag) and Gold (Au), yields approach unity at the incident energy of 150eV. On the other hand, low sputtering yield materials, such as Aluminum (Aℓ) and Chromium (Cr), yields approach unity at 500eV.

Ion penetration and radiation damage, for the energy range of 25eV to 500eV, are confined to at the most a few atomic layers of the solid surface.

Chapter 3

System Specifications and Design

In this chapter the design criteria necessary for the fabrication of thin films by ion beam deposition are considered. Following these specifications, the construction and performance of a prototype deposition system are described.

3.1 Design Criteria

The basic requirements of a deposition facility for the production of high purity, adherent thin films are:

(1) the pressure in the substrate chamber must be sufficiently low that residual gas contamination is minimized during deposition;

(2) the material comprising the film should be as clean as is practicable to maintain film purity;

(3) the arrival rate of the material at the substrate should be such that the film is built up within a reasonable time schedule;

(4) the arrival energy of the depositing material should be easily adjustable to maintain efficient film build-up with minimal film removal or substrate/film damage;

(5) the low energy ion beam should not be seriously affected by space-charge expansion.

These requirements, being basic requirements only, are not intended to be complete in themselves nor are they intended to be independent from each other. They are considered to be most important and so must be well specified and easily controlled.

The first requirement can be satisfied by adopting ultra-high vacuum techniques, moderated by the constraint of requirement three. Requirement two can be solved by the adaptation of a mass separator.

3.1.1 Vacuum Requirement

For any thin film deposition system the background pressure and the operational pressure during deposition have a significant effect on film characteristics. The main advantages of an ion beam deposition system are: the operational pressure in the vicinity of the substrate can be kept in the UHV range by a differential pumping system, and the formation of impurity layers on the substrate can be avoided by bombardment of the substrate with coating material if a sufficiently dense beam is used. This feature can be quantified by considering the balance between film material arrival and contamination at the substrate surface [1].

The rate of adsorption of background gas molecules is given by:

$$\frac{dn_a}{dt} = s\nu$$

ν = number of impinging molecules

s = sticking coefficient

From the kinetic theory of gas flow [2]

$\nu = \frac{1}{4} n v_a$

$n = \frac{N}{v}$: molecular density

v_a = average velocity

$v_a = (\frac{8kT}{\pi m})^{1/2}$

then

$$\nu = \frac{1}{4} \frac{N}{V} \left(\frac{8kT}{\pi m} \right)^{1/2}$$

$$= \frac{1}{4} \frac{P}{kT} \left(\frac{8kT}{\pi m} \right)^{1/2}$$

$$= \frac{P}{(2\pi mkT)^{1/2}}$$

$$\frac{dn_a}{dt} = s\nu = \frac{sP}{(2\pi mkT)^{1/2}} = 3.5 \times 10^{22} \frac{sP}{(MT)^{-1/2}} \quad sec^{-1} cm^{-2}$$

M = molecular weight of the gas

$m = m_0 M$

$m_0 = 1.66 \times 10^{-24}$ g : unit molecular weight

P = pressure in torr

For the condition of maximum residual gas contamination, s=1 at T = 300°K

$$\frac{dn_a}{dt} = 2 \times 10^{21} \frac{P}{\sqrt{M}} \quad sec^{-1} cm^{-2}$$

Now the rate of arrival of the elements of an ion beam can be given by

$$\frac{dn_i}{dt} = \frac{J}{e}$$

For singly-charged ions at a current density J = 20 $\mu A cm^{-2}$

$$\frac{dn_i}{dt} = 1.25 \times 10^{14} \quad sec^{-1} cm^{-2}$$

In order to produce pure thin films:

$$\frac{dn_i}{dt} >> \frac{dn_a}{dt}$$

hence

$$\frac{P}{\sqrt{M}} << 6.3 \times 10^{-8}$$

Figure 3-1 shows the above relationship.

In order to obtain highly pure films, the partial pressure must be well below the line in Figure 3-1.

3.1.2 Ion Beam Requirement

If the ion energy is sufficiently low so that unity condensation coefficient prevails at the substrate, the deposition time, t, for a singly charged particle is given by:

$$t = \frac{eN}{I}$$

where

N = total number of particles deposited

I = ion current (Ampere)

e = electric charge = 1.6×10^{-19} Coulomb

If the ion beam deposit of mass M is condensed into a thin film of area A and thickness d, then

$$N = \frac{Ad\rho N_{avo}}{M}$$

where N_{avo} = avogadro number = 6×10^{23}

$$t = \frac{e}{I} \frac{Ad\rho N_{avo}}{M}$$

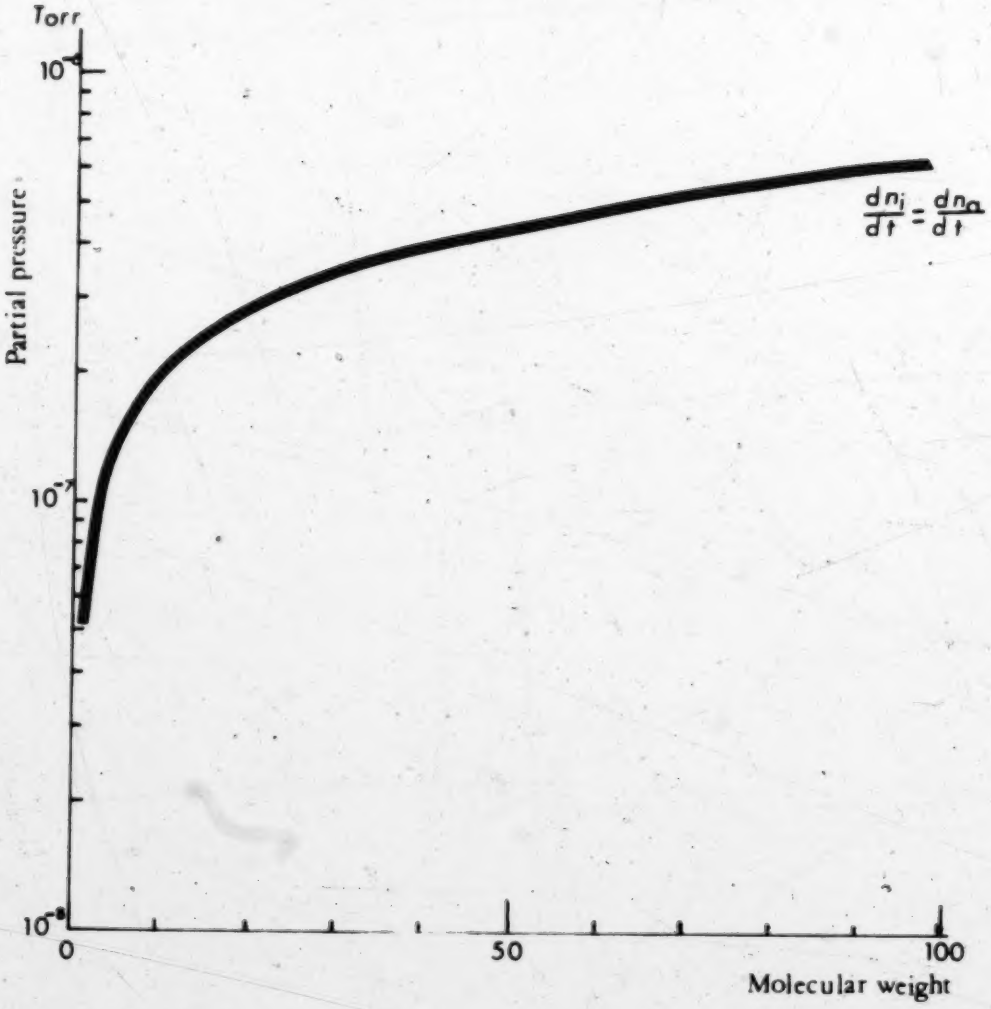

Figure 3.1 Maximum allowable partial pressure of residual gases to produce pure films.

For $I = 20\ \mu A$, $A = 1\ cm^2$, $d = 1000\mathring{A}$

$\rho = 5\ gm\ cm^{-3}$, $M = 200$

$t = 1.2 \times 10^3$ sec

and for $A = 6.25\ cm^2$, $t = 2$ hours.

Therefore, in order that the film is built up within a reasonable time schedule, a minimum ion current of several μA is required.

The deposition time is longer than that of conventional methods. However, the deposition time is much shorter than the operational time of a typical ion source and as a consequence very stable deposition is possible.

Many ion sources are commercially available, each of which is suitable for a wide range of materials [3]. At low extraction energies the ion current densities are in the low μA range; extraction efficiency is improved by increasing the extraction voltage such that keV ion beams are generated. In order to control the beam energy to minimize sputtering and substrate/film damage, a beam retarding system becomes necessary. Also it is desirable to make the most efficient use of the current available from the ion source at the target. One of the factors limiting this ion current collecting efficiency is space-charge effect in the external field free region [4,5,6]. The positive charges within an ion beam create a transverse electric force and cause the beam to spread out.

The general guide for the range of ion beam parameters, for which space charge is important in determining beam behavior, is given in Figure 3-2 [6]. Above the line space-charge effects can be dominant and below the line space-charge effect will probably not be dominant for ion beam of $M = 30$. For other M, $I \propto \frac{1}{\sqrt{M}}$ correction is

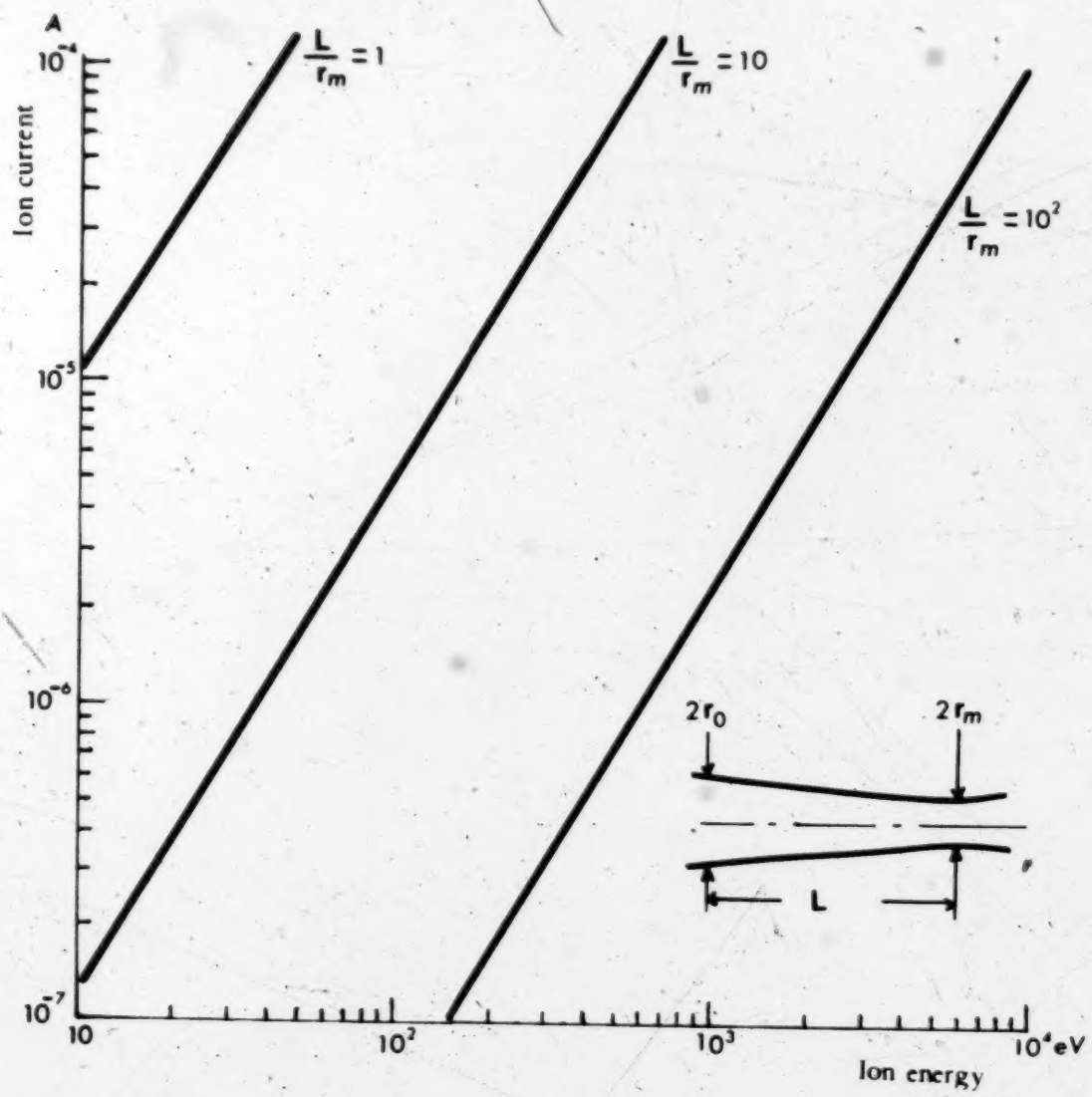

Figure 3.2 General guide for space-charge effect (6).

required.

For convergent ion beams less than 100eV and more than μA range, the focusing distance and diameter of the minimum spot size is roughly the same.

3.2 Deposition System

In accordance with the above design criteria, a proto-type ion beam deposition system has been built. During the translation from design to operational facility, various sub-criteria evolved. The construction of the main system was such that a wide range of operational freedom was allowed.

3.2.1 Vacuum System

The basic parameters for designing a vacuum system are:

(1) the total system comprises an ion source, ion beam transportation chamber and substrate chamber;

(2) pressure in the ion source is $\sim 10^{-3}$ torr (typical ion source operational pressure);

(3) pressure in the substrate chamber is 10^{-8} torr or less.

In order to satisfy the above requirements, the three stage differential pumping system was constructed.Figure 3-3 shows a schematic diagram of the pumping system and the basic parameters.

The basic relationships between these parameters are:

$$Q = S_1P_1 + C_1(P_1-P_2)$$

$$C_1(P_1-P_2) = C_2(P_2-P_3) + S_2P_2$$

$$C_2(P_2-P_3) = S_3P_3$$

The differential pumping slits have to allow the depositing ion beams to pass between the two chambers. The size of C_1 is

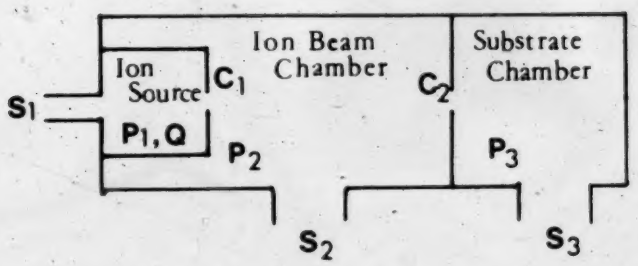

$P_1 = 10^{-3}$ Torr

$P_3 = 10^{-8}$ Torr

C_1 & C_2; Conductance of holes

$S_1, S_2,$ & S_3; Effective pumping speeds

Figure 3.3 Schematic diagram of differential pumping system.

determined by the ion source operational characteristics and is generally between 0.020"ϕ to 0.040"ϕ [7]. The conductance of an aperture for air at 20°C in molecular flow region is given by [8]:

$$C = 11.6\ A \qquad \ell\ sec^{-1}$$

where

A = aperature area (cm^2)

Then $0.02\ \ell\ sec^{-1} \leq C_1 \leq 0.09\ \ell\ sec^{-1}$

Assume $C_1 = 0.06$ ℓ/sec and $P_1 >> P_2 = 5 \times 10^{-7}$ torr

$$Q \simeq P_1C_1 + P_1S_1$$
$$\simeq 6 \times 10^{-5} + S_1 \times 10^{-3}$$

Assuming $Q \simeq 10^{-4}$ torr $\ell\ sec^{-1}$, then $S_1 \simeq 0.4\ \ell\ sec^{-1}$. The aperture size of C_2 is determined by the mass separation characteristics of velocity filter (see next section), and 4mm x 40mm slit size was found to be satisfactory. This aperture size yields $C_2 = 18\ \ell\ sec^{-1}$. Again assume $P_2 >> P_3 = 10^{-8}$ torr, then

$$S_2 = \frac{C_1P_1 - C_2P_2}{P_2} \simeq 100\ \ell\ sec^{-1}$$

$$S_3 = \frac{C_2(P_2 - P_3)}{P_3} \simeq 900\ \ell\ sec^{-1}$$

The above estimated value is summarized in Table 3-1.

	Ion Source	Ion Beam Chamber	Substrate Chamber
Effective pumping speed ($\ell \cdot s^{-1}$)	0.4	100	900
pressure (Torr)	10^{-3}	5×10^{-7}	10^{-8}
conductance	$C_1 = 0.1\ \ell\ sec^{-1}$	$C_2 = 18\ \ell\ sec^{-1}$	

Table 3-1 Estimated Vacuum Parameter

A diagram of a vacuum system which satisfies this estimation is shown in Figure 3-4. The design of this system permits a wide range of diagnostic attachments to be added such as ISS [9] and SIMS [10,11].

The whole system is bakable at an intermediate temperature (up to 200°C because of the use of a polyimide insulator). Partial baking of the substrate chamber is also possible by surrounding it with heating tape.

The substrate chamber is pumped by a Balzers TVP251 turbo molecular pump (p.s. = 70 ℓ/s) and a Varian Ti-ball sublimation Pump (p.s.> 1000 ℓ/s) generating a total effective pumping speed of over 1000 $\ell\ sec^{-1}$. The ion beam chamber is pumped by a liquid nitrogen trapped Edwards 6-inch diffusion pump (p.s. = 600 $\ell \cdot s^{-1}$), the pumping stack having an effective pumping speed of over 100 ℓ/s. The ion source is roughed out by the gas handling plant rotary pump and final pumping is through the anode hole.

Ion source maintenance or changing of substrate can be carried out without breaking the complete vacuum when the 6-inch gate valve between the substrate and the ion gun chamber is closed.

After outgassing the ion source, the ultimate pressure in the ion beam chamber stabilized at 10^{-8} Torr without bakeout. The pressure

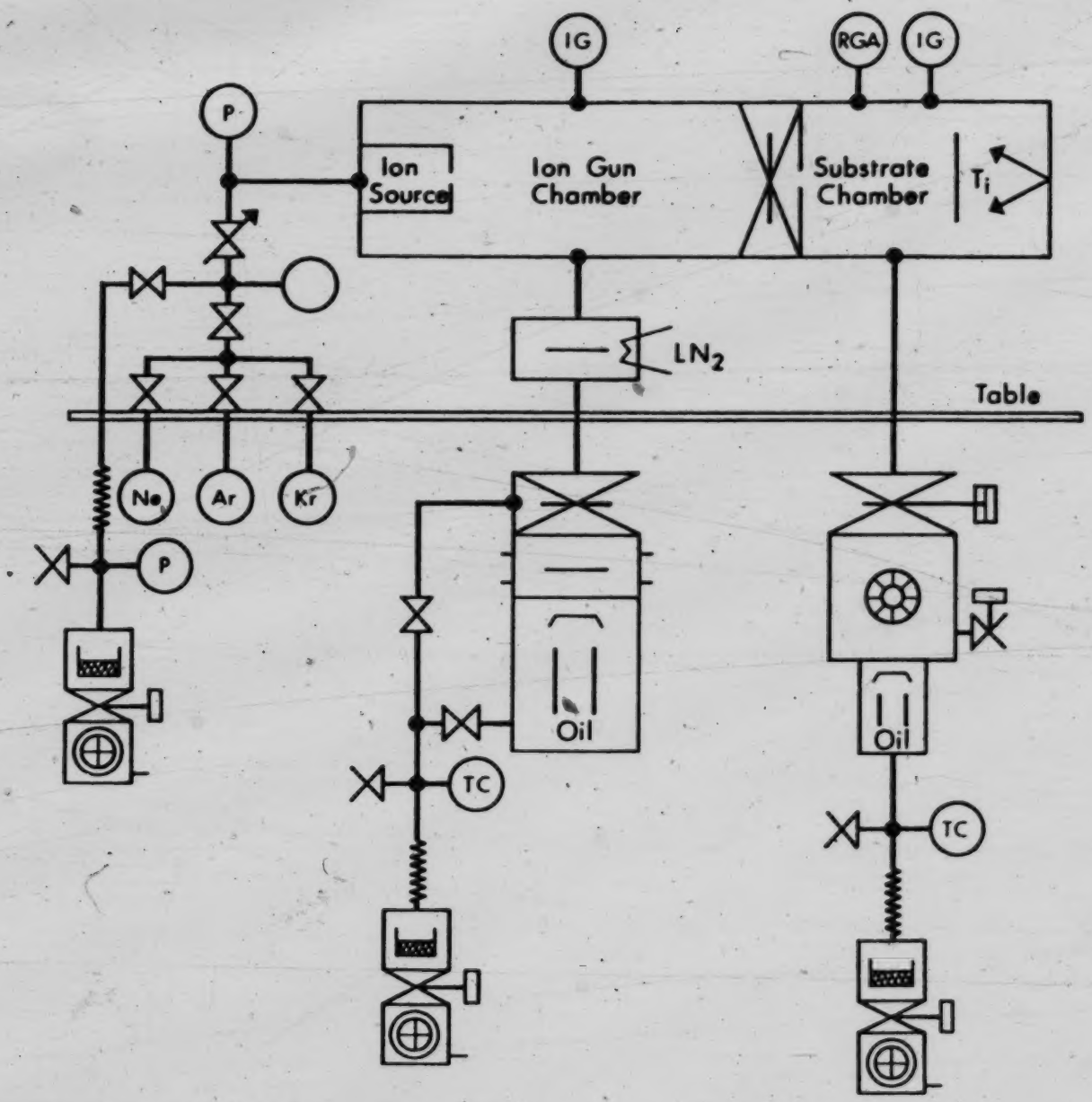

Figure 3.4 Schematic diagram of vacuum system.
(after A.V.S. Standard 7.I - 1966)

during operation varies from the order of 10^{-7} to 10^{-8} Torr depending on the support gas or materials being ionized. A turbo-molecular pump was chosen for the substrate chamber because it is essentially maintenance-free. Since the pumping speed of the turbo-molecular pump is low for light gases and hydrogen is the major residual gas constituent after a normal bake at 200°C, a small air-cooled diffusion pump was added as a booster pump between the turbo-molecular pump and its trapped rotary pump. Because this diffusion pump was started after the turbo-molecular pump had reached operational speed (after 15 minutes), oil backstreaming from the untrapped diffusion pump was prevented from reaching the substrate chamber. The hydrogen partial pressure was found to fall by a factor of 2 when the diffusion pump was deployed. Further reduction of the hydrogen partial pressure follows the activation of the sublimation pump. Typical operating pressures in the substrate chamber are 10^{-8} - 10^{-9} Torr; partial pressure analysis using an A.E.I. Minimass RGA yields gauge readings of $1x10^{-9}$ Torr for mass 2 and $1x10^{-10}$ Torr for mass 18. No other residual gases can be detected by this mass spectrometer. The pumping performance of the facility was therefore considered to meet design specifications.

3.2.2 Ion Beam System

In order to satisfy the design criteria, the Colutron ion beam system Model G-2 was chosen. This system is small, bakable, and versatile. Figure 3-5(a) shows a schematic of the ion source, ion beam transportation system, the drift space provided by the gate valve, and the substrate chamber. Figure 3-5 (b) shows a photograph of the system. The main components consist of the ion source with

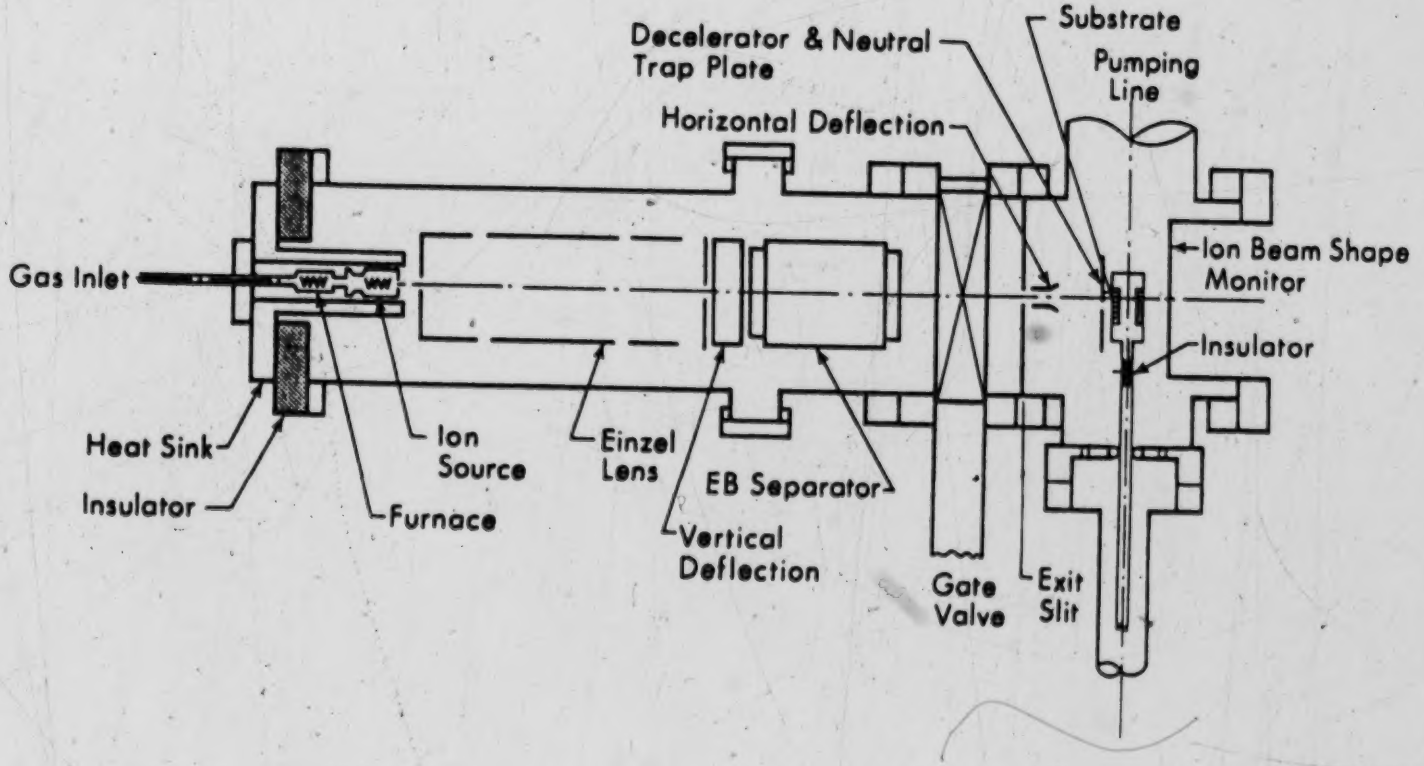

Figure 3.5(a) Low energy ion beam deposition system

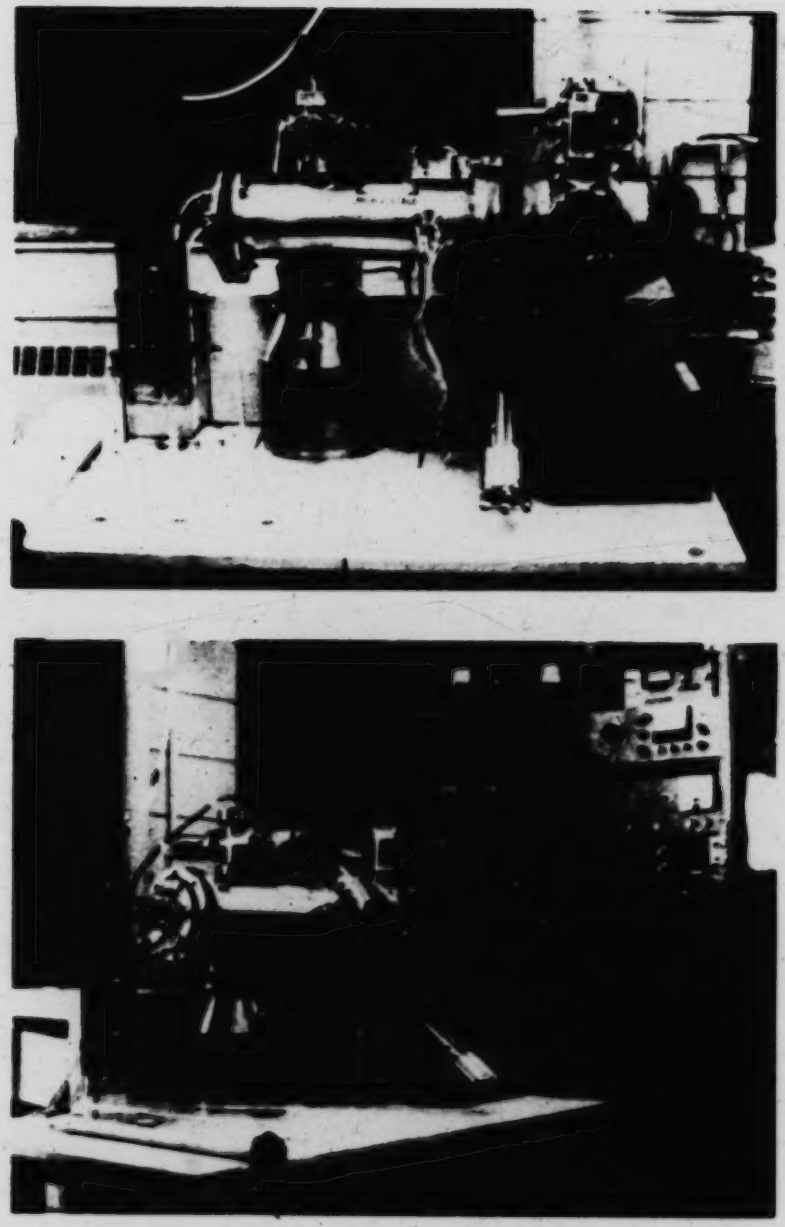

Figure 3.5 (b) Photograph of the low energy ion beam deposition system.

a low-energy spread of 0.2eV, acceleration and focusing system, vertical deflection plates, and a ExB velocity filter by which the beam profile may be altered at will [12,13]. The quoted system specification is as follows [7].

Ion Current: several μA

Resolution : $M/\Delta M \simeq 400$ after a drifting distance of 50 cm.

Where M is the center mass and ΔM is the full width at half maximum (FWHM).

Figure 3-6 shows a block diagram of the system electronics. The following Table 3-2 describes the details of each power supply.

A. Ion Source

The ion source operates on a low-voltage arc discharge principle at low pressure [14,15,16]. It consists of a hot thermionic cathode and an anode with a small hole in the center. The cathode is heated to a temperature sufficient to cause thermal electron emission. A low D.C. voltage applied between the cathode and the anode causes a region of spare charge limited potential to form around the cathode. Electrons are accelerated through this space-charge region and ionize the gas in the interaction region, forming a plasma region (the positive column) around the anode. By generating such a plasma, and by extracting the ions from the plasma region through the hole in the anode, an ion beam with small energy spread is obtained.

The ion source itself was modified somewhat by adding a small resistance heated furnace behind the ion source, Figure 3-7, in order

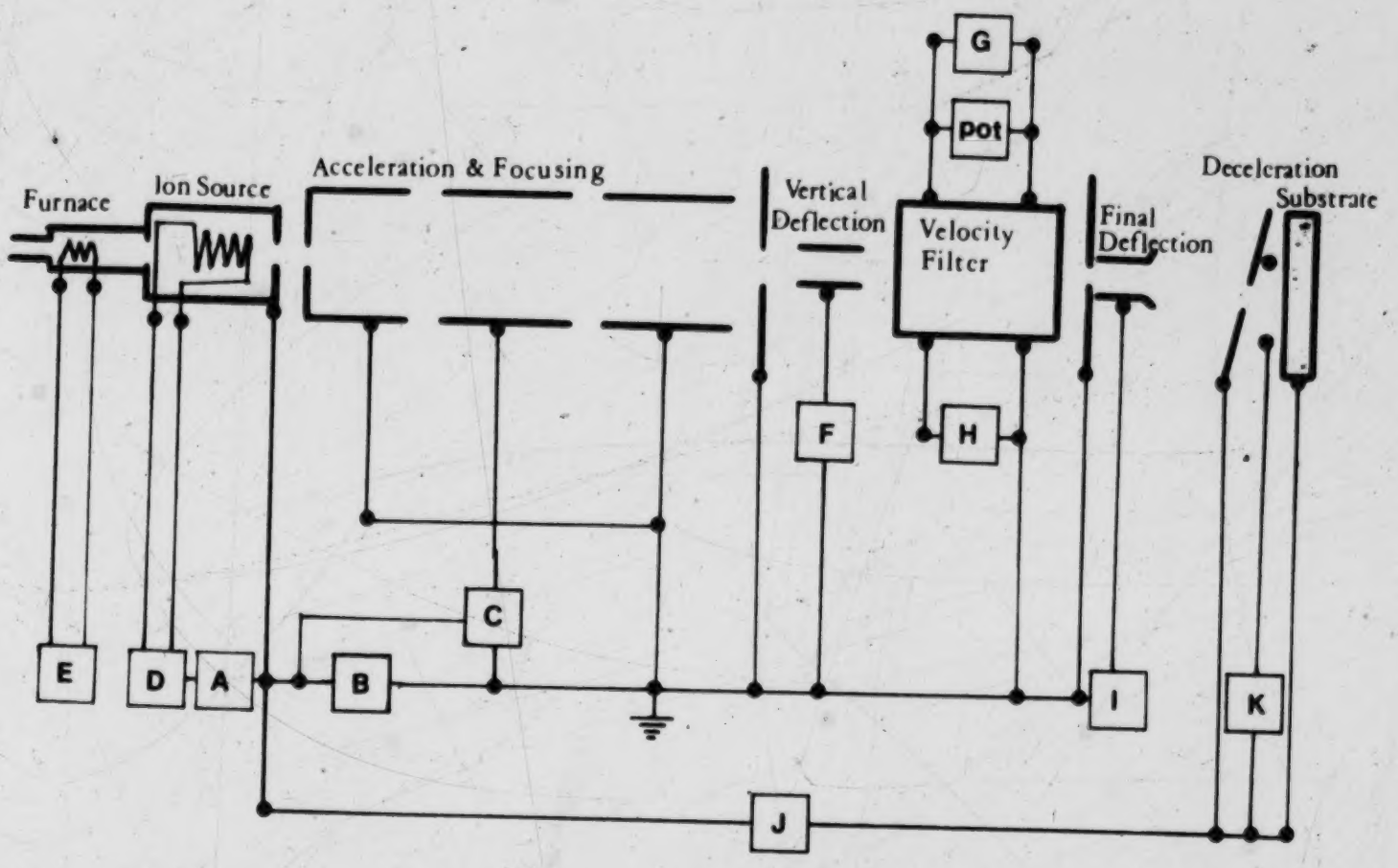

Figure 3.6 Block diagram of the system electronics.

Table 3-2 Power Supply

System	Model	Range	Regulation	Stability
A Anode	Kepco HB6AM	325Vx600mA	0.01%	0.01%
B Acceleration	Fluke 408B	0-6kV	0.01%	0.01%
C Einzel lens	High Voltage Stabilizer IC (723) Regulator	0-5kV	1%min	1%min
D Filament	Canadian Research Institute MRP16-20 with modified IC(723) regulator	16Vx20A	0.1%	0.1%
E Furnace	Unregulated A.C. power supply	15Vx22.5A	-	-
F Vertical deflector	Kepco ABC 425	0-425V	0.05%	0.05%
G Velocity filter plate	Lambda LPD-425FH	0-250V	0.01%	0.02%
H Magnet	Canadian Research Institute MRP 16-16 with modified IC(723) regulator	16Vx16A	0.1%	0.1%
I Final deflection	Brandenburg 472R	10V-2100V	0.01%	0.01%
J Ion Energy	IC(723) Regulated D.C. power supply	0-500V	0.1%	0.1%
K Electron filament	Unregulated A.C. power supply	15Vx15A	-	-

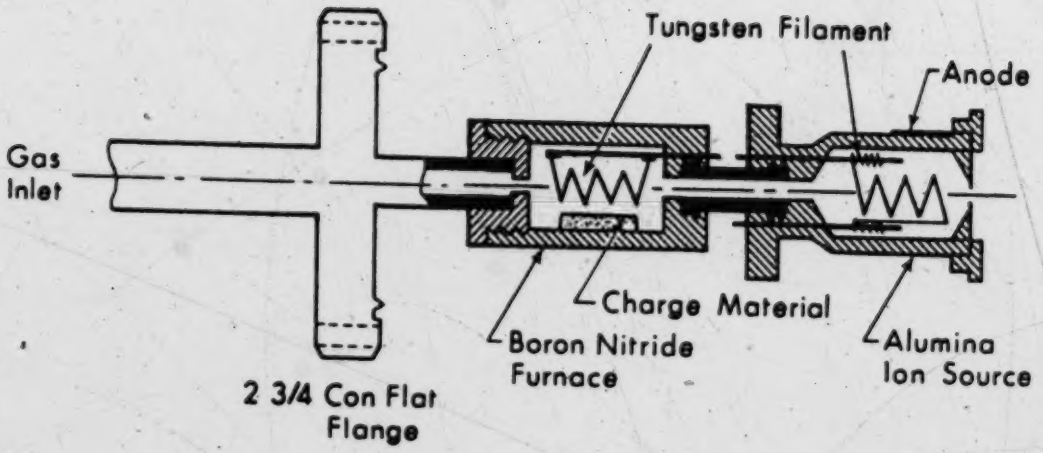

Figure 3.7 Plug-in ion source with furnace.

to produce long-lifetime operation when running solid materials. Considerable benefits accrued from this addition when compared with the original design, which required that a solid charge be inserted into the discharge region of the filament loop. These benefits are as follows:

a) the charge could be added and the system sealed completely, eliminating sliding feedthroughs which frequently broke vacuum;

b) the plasma shape in the source remained unchanged;

c) the operational lifetime of the ion source was increased;

d) alloying and other interactions of the ion source filament with the charge material was eliminated;

e) the vaporation rate was more controllable.

Investigations of the performance of the ion source without the furnance were carried out by using several gases [17]. It has been proven that the ion source produces gaseous ion currents of several μA. Under these operational conditions, the temperature of the thermionic cathode was measured at about 2000°C. The ion source wall temperature was estimated to be about 1500°C by inserting a stainless steel tube containing a thermo-couple.

With the addition of a furnace, ion beams of element metals have been generated and in the case of Mg and Pb, supporting gases are not necessary. In the case of Pb ion beams, the furnace and source have operated for over 100 hours with one charge. In the case of Mg the operational time of one charge is about 50 hours. Table 3-3 shows vaporization temperature of the elemental metals which have been used

to date. In the case of Cu and Ag, the condensation of vapor between the furnace and ion source was a limiting factor in obtaining sufficiently high current density ion beams. The details of this problem will be discussed in Chapter 5.

Materials	Mass	Vap.Temp. for 10^{-2} torr(°C)
Mg	24.3	440
Pb	207.2	715
Ag	107.9	1030
Cu	63.5	1260

Table 3-3

Vaporization Temperature of Elemental Metals

B. Velocity Filter

The ion beam is extracted by floating the source and gas handling plant assembly up to 4KV and grounding the extracting electrode. An Einzel lens (unipotential electrostatic lens) is combined with this extraction electrode and provides a means of focusing the ion beam without changing the ion energy [18]. Mass separation and beam profiling was carried out by the $E_x B$ velocity filter which consists of a magnet, a pair of electrostatic deflection plates and sets of guard rings, which latter ensure a uniform electrostatic field. A selected class of ions will pass straight through the filter, while ions with different mass or velocity will be deflected. Figure 3-8 shows a simplified diagram of the velocity filter mechanism.

The mass selection rule of the velocity filter is given as:

$$M = 2eV_a \left(\frac{B}{E} \right)^2$$

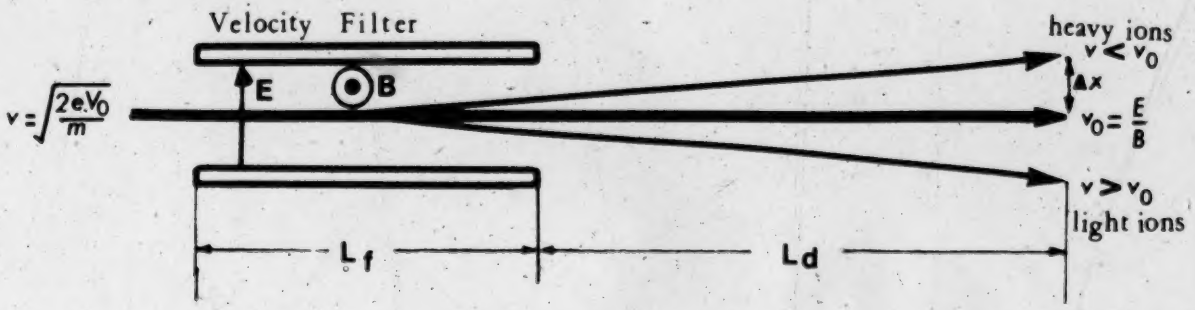

Figure 3.8 Schematic diagram of velocity filter.

where M is the mass which passes straight through the filter,

e is the ionic charge

V_a is accelerating voltage or ion energy

B is magnetic field strength

E is electric field strength

Assuming $B \alpha I$ and $E \alpha V_p$

where I is velocity filter magnet current

V_p is velocity filter plate voltage

$$M \alpha V_a \left(\frac{I}{V_p} \right)^2$$

For a variable Va(2KV to 4KV), the optimum mass selection condition of the velocity filter was examined.

At high V_p it was impossible for heavy masses to pass straight through the filter. On the other hand, at low V_p or high V_a, it was difficult to obtain a good line shaped beam and the dispersion was small (refer to mass separation rule). For overall requirements, it is found than an acceleration voltage of V_a=4 KV and plate voltage V_p= 100 V produce the optimized condition. The following relationship between the molecular weight and magnet current was experimentally determined and plotted on Figure 3-9.

$$M = 3.24\ I^2 \text{ for } V_p = 100V \text{ and } V_a = 4\ KV$$

From Figure 3-9 an ion beam of maximum $\sim$ 600 molecular weight can be selected by the velocity filter without severe distortion of the ion beam shape. This characteristic shows a good potentiality for

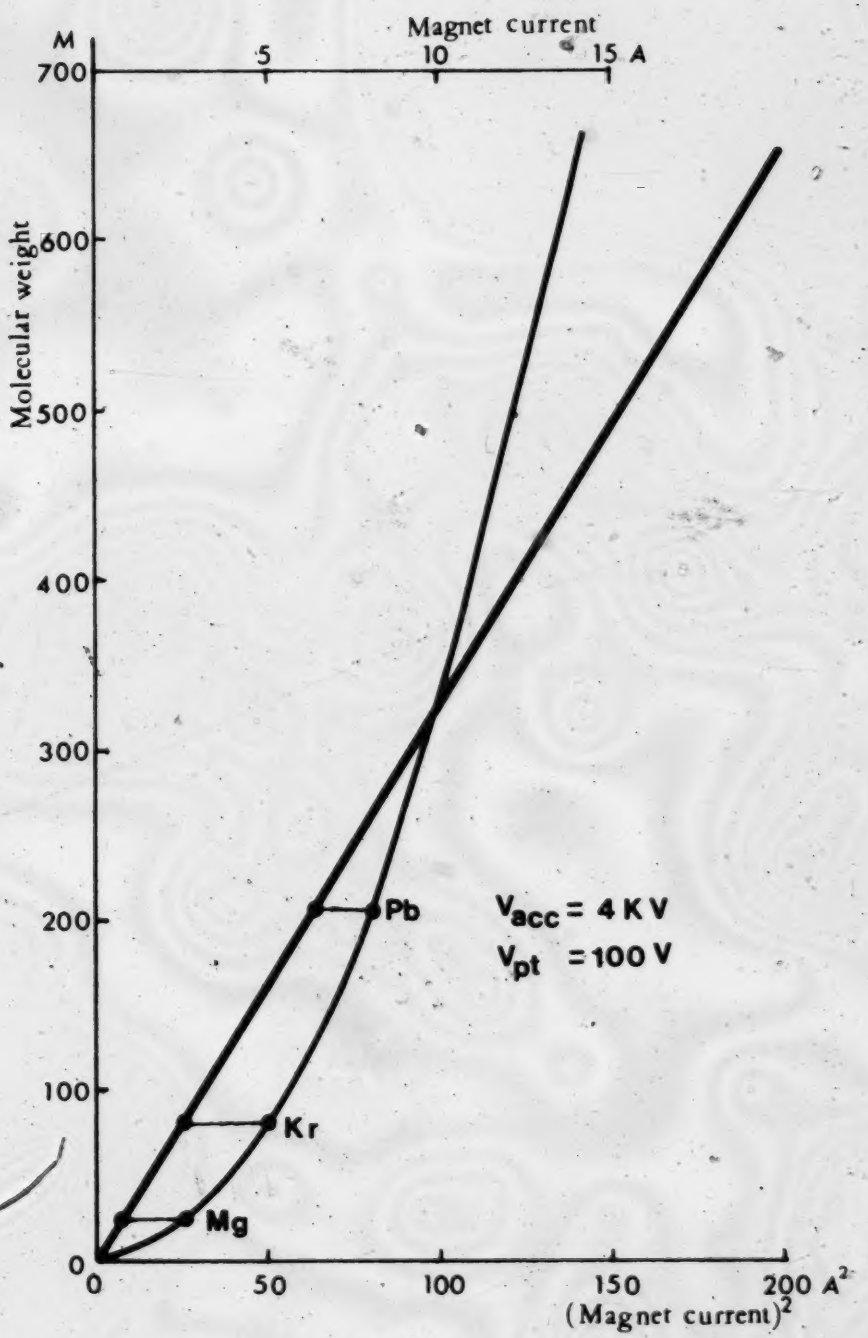

Figure 3.9 Mass selection of velocity filter.

depositing a wide variety of materials.

The mass separation rule of the velocity filter is given as [6]

$$\Delta X = \frac{\Delta M}{M} \frac{L_f E}{4V} \left(\frac{L_f}{2} + L_d \right)$$

where ΔM is mass difference at FWHM

Setting $E = 5.6 \times 10^3$ v/m (plate voltage 100 volts)

$V = 4 \times 10^3$ V (accelerating voltage)

$L_f = 0.15$m (G-2 gun velocity filter)

$L_d = 0.11$m (present exit slit position)

$$\Delta X = \frac{\Delta M}{M} \times 10^{-2} \text{ m}$$

Choosing $\Delta X = 2 \times 10^{-3}$ m,

$\frac{M}{\Delta M} \simeq 5$ is obtained.

Even when ion beams of only slightly differing molecular weights are considered, such as Mg^+ (24) and N_2^+ (28), $\frac{M}{\Delta M} = 3$. The exit slit functions as a differential pumping slit and as a first stage eliminator of unwanted ion beams.

Therefore, the capacity of the velocity filter to produce single mass ion beams in spite of a short drifting distance is quite satisfactory.

Also, the velocity filter is used to focus the ion beam into a line-shape image for the convenience of wide-area deposition.

3.2.3 Substrate Chamber

The substrate chamber consists of an ion beam exit slit, an electrostatic deflector, a decelerator, an electron emission filament, and a substrate assembly. Figure 3-10 shows the substrate configuration.

Figure 3-11 shows the data handling system. The ion current was optimized by minimizing the decelerator current and maximizing the substrate current. The total ion dosage was measured by the current integrator coupled with Digital/Analog converter. By this method constant total ion dosage was monitored even when the ion current was varied during deposition.

The mass-selected ion beam passes through the exit slit and is deflected towards the substrate. Neutral particles, radiated from the ion source and/or created in the ion beam chamber, are undeflected and strike the decelerator plate. The desired ion beams will pass through the decelerator opening and reach to the substrate.

The decelerator consists of a simple flat plate machined from type 304 stainless steel with a slit in the center. Several designs of decelerator configurations have been developed for isotope collections [10,20]. Many of the designs are concerned with deceleration to 1KV or more, and for low ion current density brams. The present design is very simple, but very practical for high ion current density beams, because the design allows the substrate to be located close behind the decelerator plate. For example, with this decelerator configuration, 15μA of Mg^+ ion beams with 20eV energy were collected at the substrate.

The decelerator plate is located 53mm from the exit slit, and

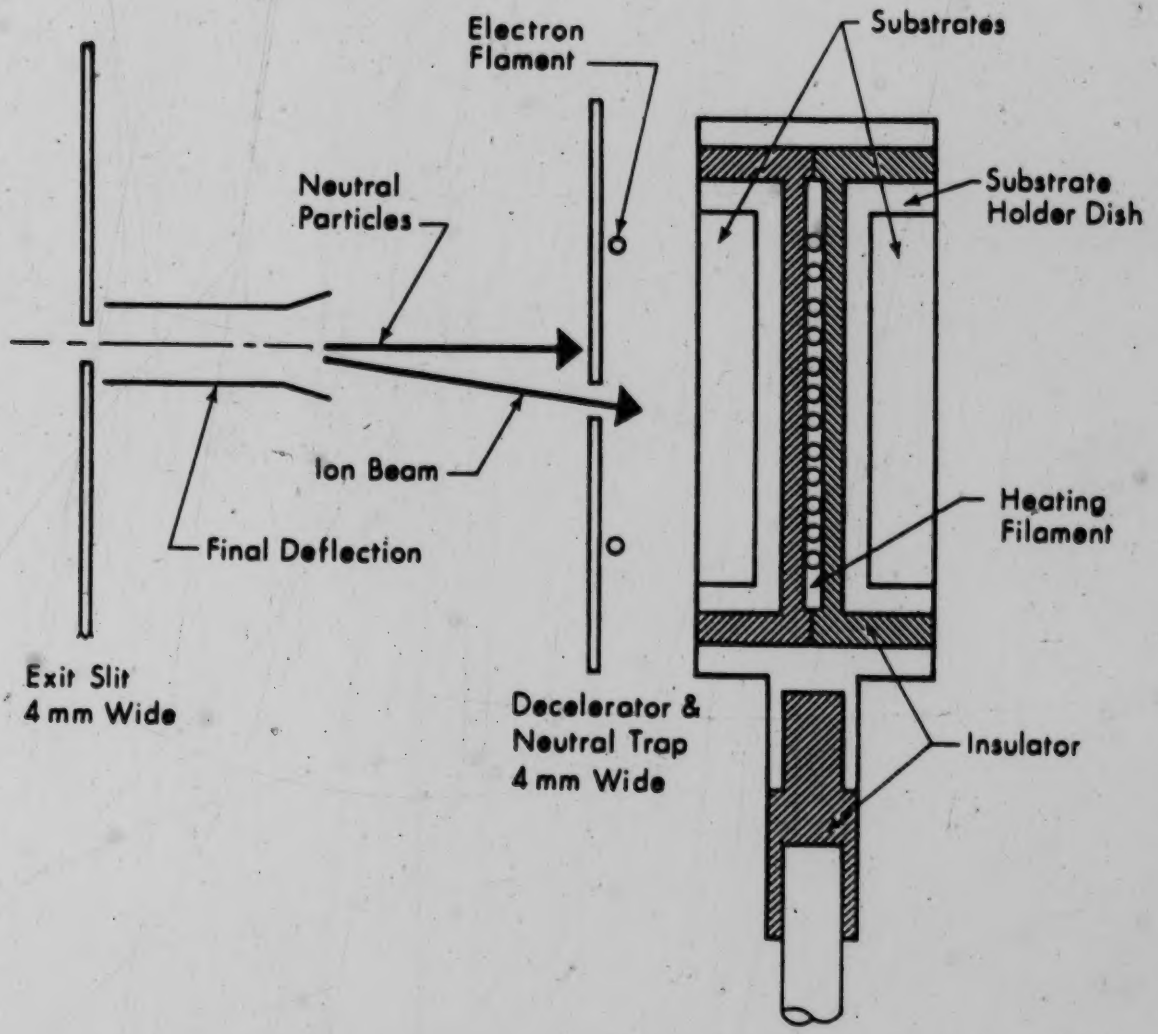

Figure 3.10 Substrate chamber configuration.

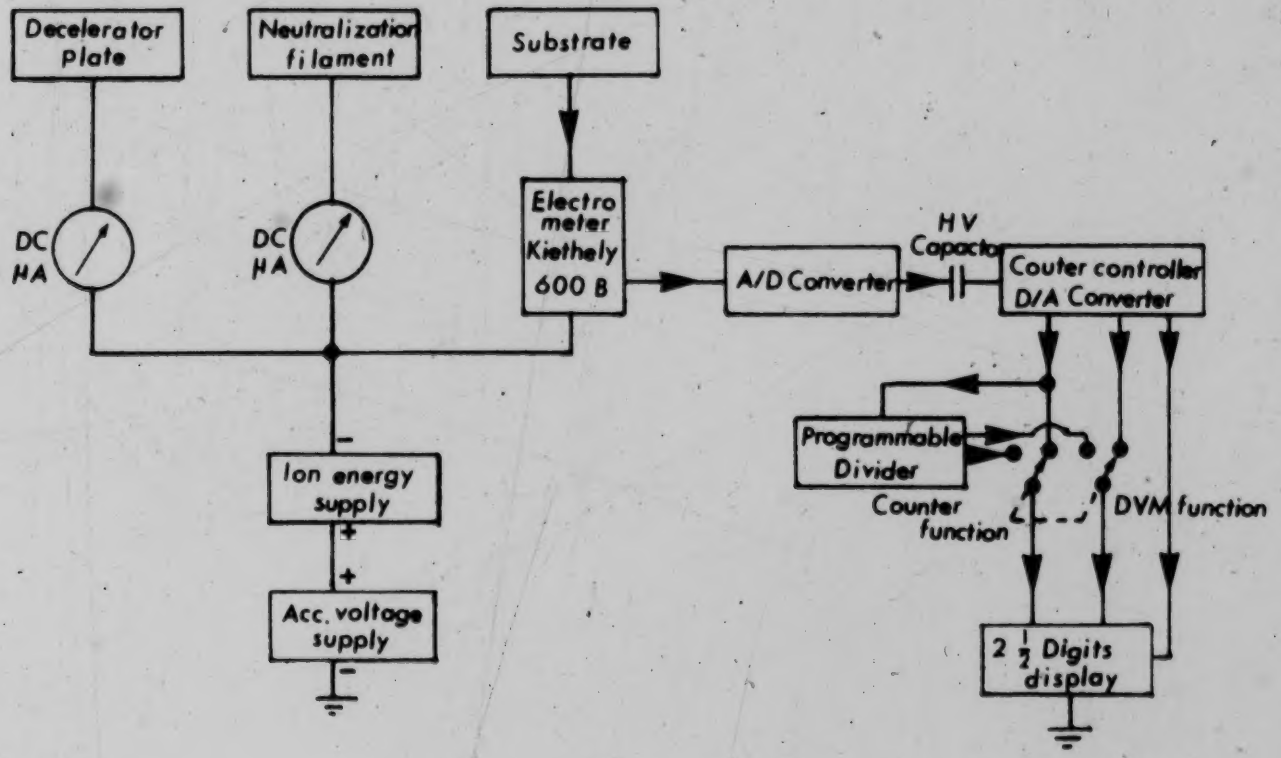

Figure 3.11 Block diagram of data handling system.

its opening is located 5 mm to 6mm to one side of the main beam line axis. The 4 keV ion beam of a selected mass is deflected off the beam axis by a potential of + 250 volts on one deflector plate. The other plate is grounded. The deflector plate is push-pull configuration to ensure a uniform electrostatic field on the off-axis ion beams. The mass resolution at the decelerator plate with 4mm to 5mm-wide opening is calculated as $M/\Delta M = 10$ for a total drifting distance of 0.18m. Therefore, even with such a short ion beam drifting distance, adequate mass separation is carried out for the deposition of desired ion beams. Higher resolution for isotope separation is not necessary and, because of the reduction of ion current, is not desirable for this application.

Figure 3-12 shows the profile of well focused 4 keV ion beams of several gases, within the limitations of the short drift length. The ion beam of each element is scanned electrostatically, and the ion beam profile monitored by a target mounted behind the 0.4mm slit plate. The dashed lines in Figure 3-12 show the 4mm wide decelerator openings. When an ion beam consists of several isotopes, about 10% of the total ion current is lost by the 4mm opening decelerator. When the 5mm opening decelerator was used, about 5% of the total ion current was lost. Most of the thin film deposition was carried out by using the 5mm opening decelerator which was located 6 mm off the beam axis.

The ion beam is decelerated by applying the ion source voltage (4kV) minus a variable negative voltage (0-500 volts) to the decelerator plate and to the substrate. The ion beam energy is

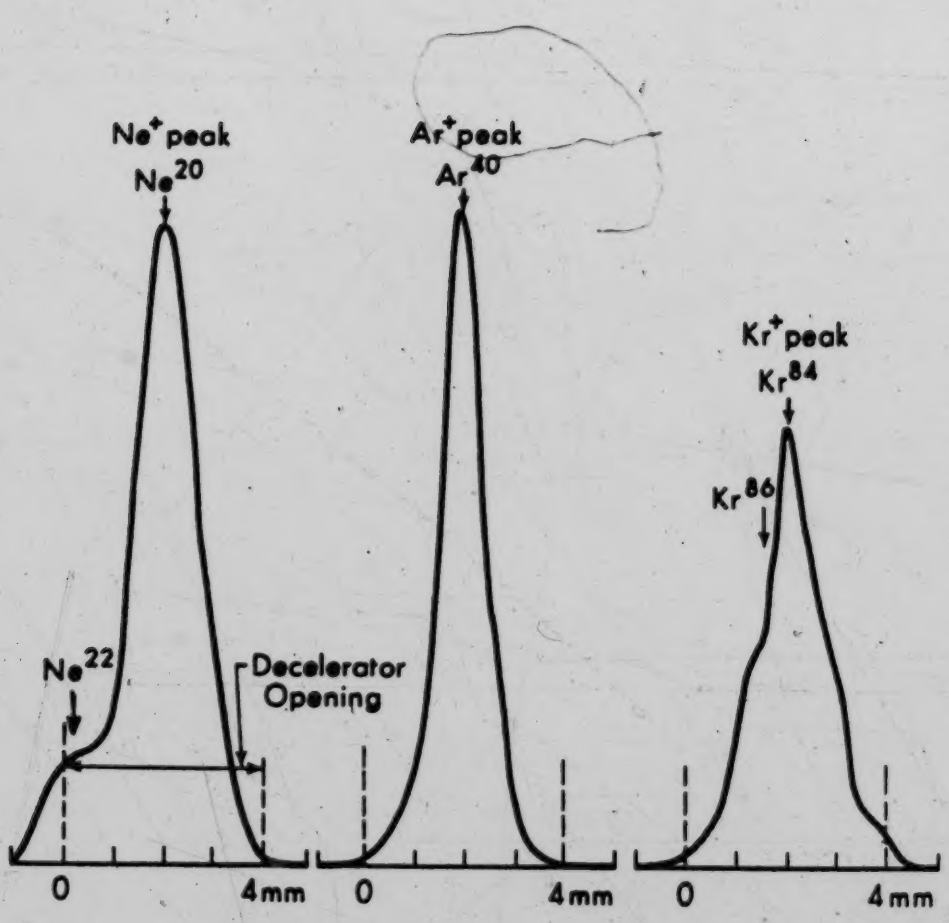

Figure 3.12 Typical 4 KeV ion beam profile at substrate.

defined by this negative voltage. At a very low energy (below 20eV), the energy spread (transverse velocity components) causes serious ion beam spreading [21]. For an ideal ion beam which has only axial components of velocity, the ion beam cut-off will occur when the ion beam energy is zero. However, in practice, the ion current is reduced as the beam energy decreases. Figure 3-13 shows a typical ion current cut-off curve. At an energy of 20eV, about 30% of the incoming beam is lost due to the accelerator-decelerator geometry and the transverse spreading of the ion beam. In order to improve these characteristics, the decelerator was tilted 10° with respect to the in-line beam axis, i.e. the deflected ion beam experienced a normal retarding potential. Significant improvement was not observed for the ion current cut-off curve. Consequently, the reduction of a ion current in a low energy range is considered to be caused by the energy spread of the ion beam which in turn is controlled by both the plasma temperature of the ion source and the accelerator geometry.

After passing through the decelerator opening, the beam enters the field free region between the decelerator and the substrate. Initially, the beam is strongly focused by the single aperture lens (the decelerator plate) and subsequently spreads out because of space-charge expansion.

The focusing distance of the single aperature lens, f, is given as [22]

$$f = \frac{4(V-V_o)}{E_1 - E_2}$$

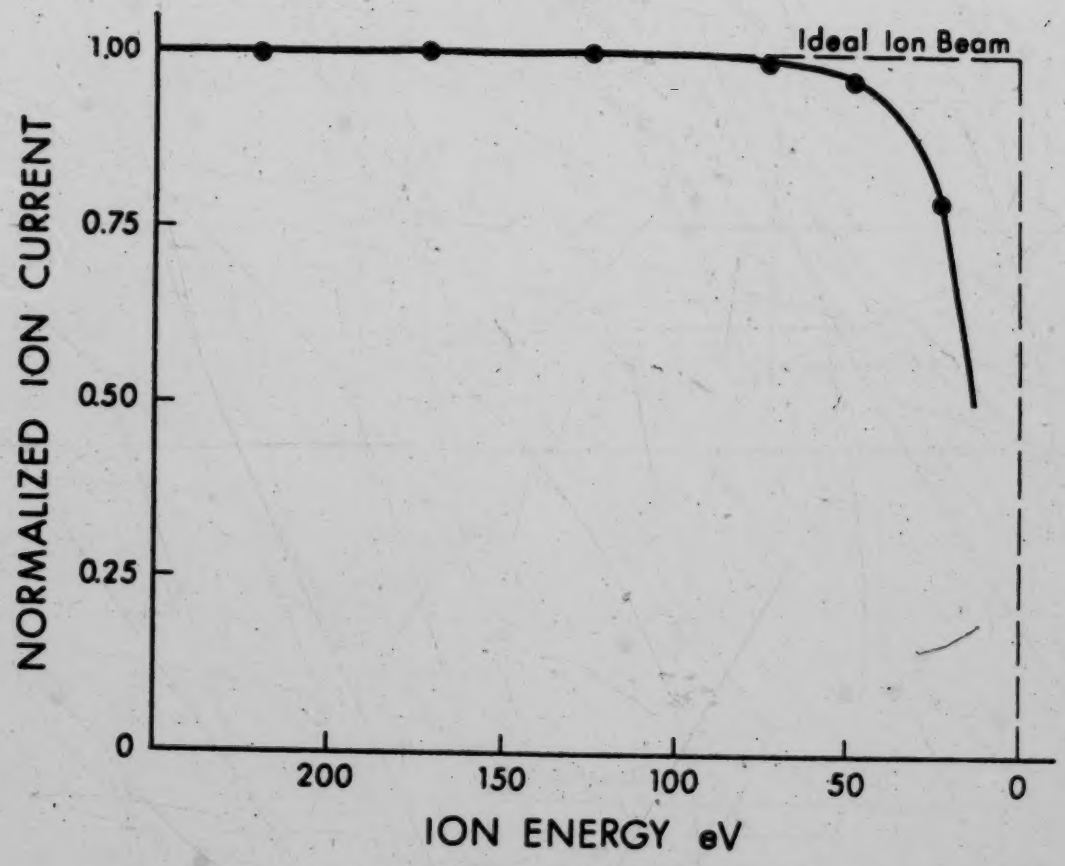

Figure 3.13 Ion beam current cut-off characteristic.

V = decelerator potential

V_o = initial ion energy

E_1 = electric field before decelerator, $E_1 = \frac{V_o}{d}$

E_2 = electric field after decelerator $E_2 = 0$

then

$$f = \frac{4(V-V_o)}{-\frac{V}{d}} = 4\left(\frac{V_o}{V} - 1\right)d$$

Setting d = 53 mm, V_o = 4KV, the estimated focusing distance is as follows:

100 eV ion beams f = 5 mm

300 eV ion beams f = 17 mm

The effect of the space charge expansion was then investigated by fixing the distance between the decelerator and the substrate as 10 mm. Figure 3-14 shows the 6μA Pb^+ ion beam profile for various energy levels. The substrate was replaced by a 0.4mm slit plate and the beam profile monitor was installed immediately behind this opening. The beam profile was obtained by mechanical movement of the whole substrate assembly.

The greatest measurable ion beam spreading was about 4 mm wide. The measured spreading differed from the ion beam spreading estimated in section 3.1.2, because of the strong focusing effect of the decelerator plate. In addition a shift in the position of the ion beam occurred, because of the transverse velocity component in ion beam.

If the substrate is an insulator, the surface charges must be neutralized so as to prevent surface charge built up which causes

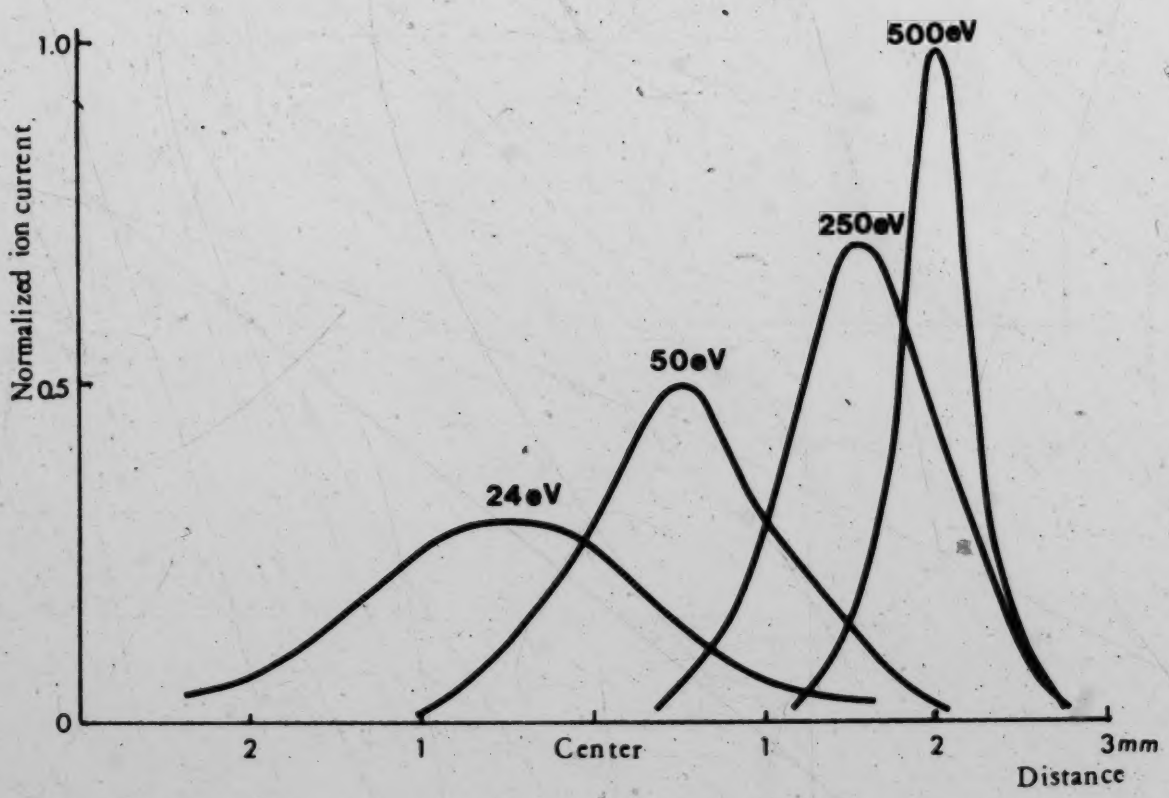

Figure 3.14 Space-charge expansion of Pb ion beam.

reflection of ion beams by an electrostatic force [23]. In order to overcome this surface charge build-up, a thermal electron emission source consisting of a 0.015" dia. Th-W loop is placed a few mm in front of the substrate. In order to neutralize the surface charge, it was found that the electron emission current had to be approximately twice as much as the ion current.

The average temperature rise of the substrate assembly caused by this thermal electron emission filament was measured to be ∿100°C by using a conventional Pt-Pt 13% Rh thermocouple located at the ceramic substrate holder. However, higher local temperatures are expected because of the loop configuration of the filament.

Several different substrate holders were made to accommodate substrates of different sizes and shapes which were used in various diagnostic analyses. Figure 3-15 shows photographs of different substrates and substrate holders.

3.3 Substrate Preparation System and Storage System

In most of the deposition experiments, a carbon substrate was used, because of its good electrical conductivity, its low sputtering yield and its low atomic mass. The latter characteristic yields better results in identifying impurities by Rutherford Backscattering analysis.

A commercially available high purity fine grain carbon graphite manufactured by Poco Graphite, type AXE-5Q1 (1.00"ϕ x 0.625"), was used as a substrate material for RBS analysis (Figure 3.15(a)). This graphite has a total ash range of 5 ppm or less [24].

For the transmission electron microscope analysis, a specimen thickness has to be less than 1000 Å for electron transmission.

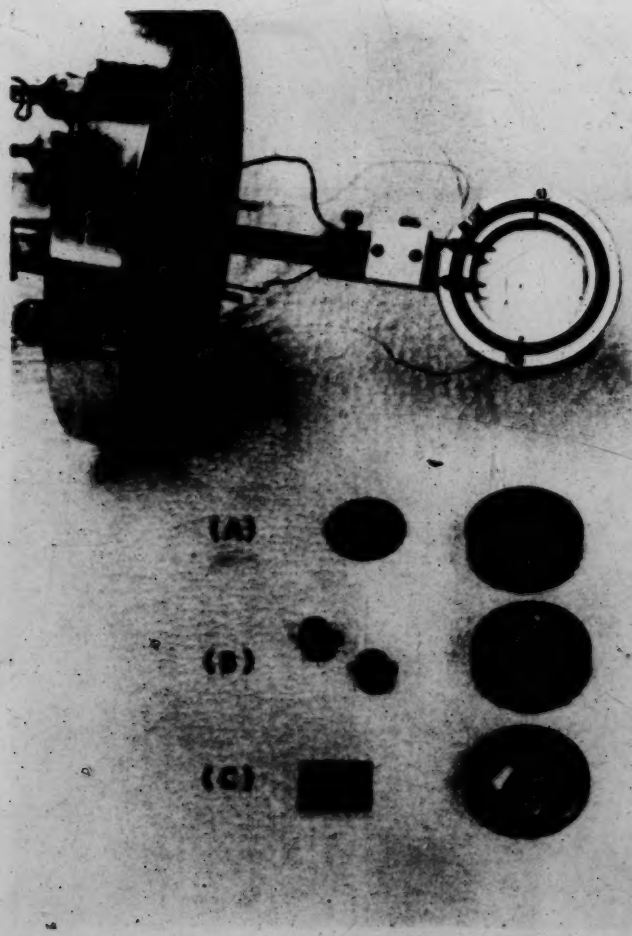

Figure 3.15 Photograph of substrates and substrate holders.

Therefore, a self-supporting carbon thin film deposited on a Corning cover glass (#1, 22 mm eq) was used as a substrate (Figure 3.15(c)). Figure 3.16 shows a schematic diagram of a carbon arc evaporation system which was built for this purpose. The glass plates were placed above the arc to avoid any large pieces of debris falling onto it. The thickness of the carbon films was monitored by an optical color change which varies with the number of arc discharges. In general 20 to 30 arc discharges yield a light brown coloration of glass plate which correspond to carbon film thickness of 100-200 Å [25,26].

For the scanning electron microscope analysis, the specimen was prepared by direct deposition onto a SEM specimen holder made out of a carbon rod manufactured by Union Carbide, type ATJS (Figure 3.15(b)).

An air-cleaved NaCℓ single crystal was also used as a substrate for TEM analysis in order to investigate the possibility of epitaxial film growth.

After deposition, every substrate specimen was kept inside a storage system in order to minimize atmospheric contamination, particularly oxidation of freshly deposited metallic films. Figure 3.17 shows a schematic diagram of the substrate storage system built for this purpose. After the substrate was placed inside the bell-jar, the system was pumped down to about 10^{-2} Torr by a Varian VacSorb pump cooled with liquid nitrogen for longer storage time. Industrial grade purity Argon was then admitted into the system until several torr Argon pressure was reached. Every time the system was opened to air, this procedure was repeated.

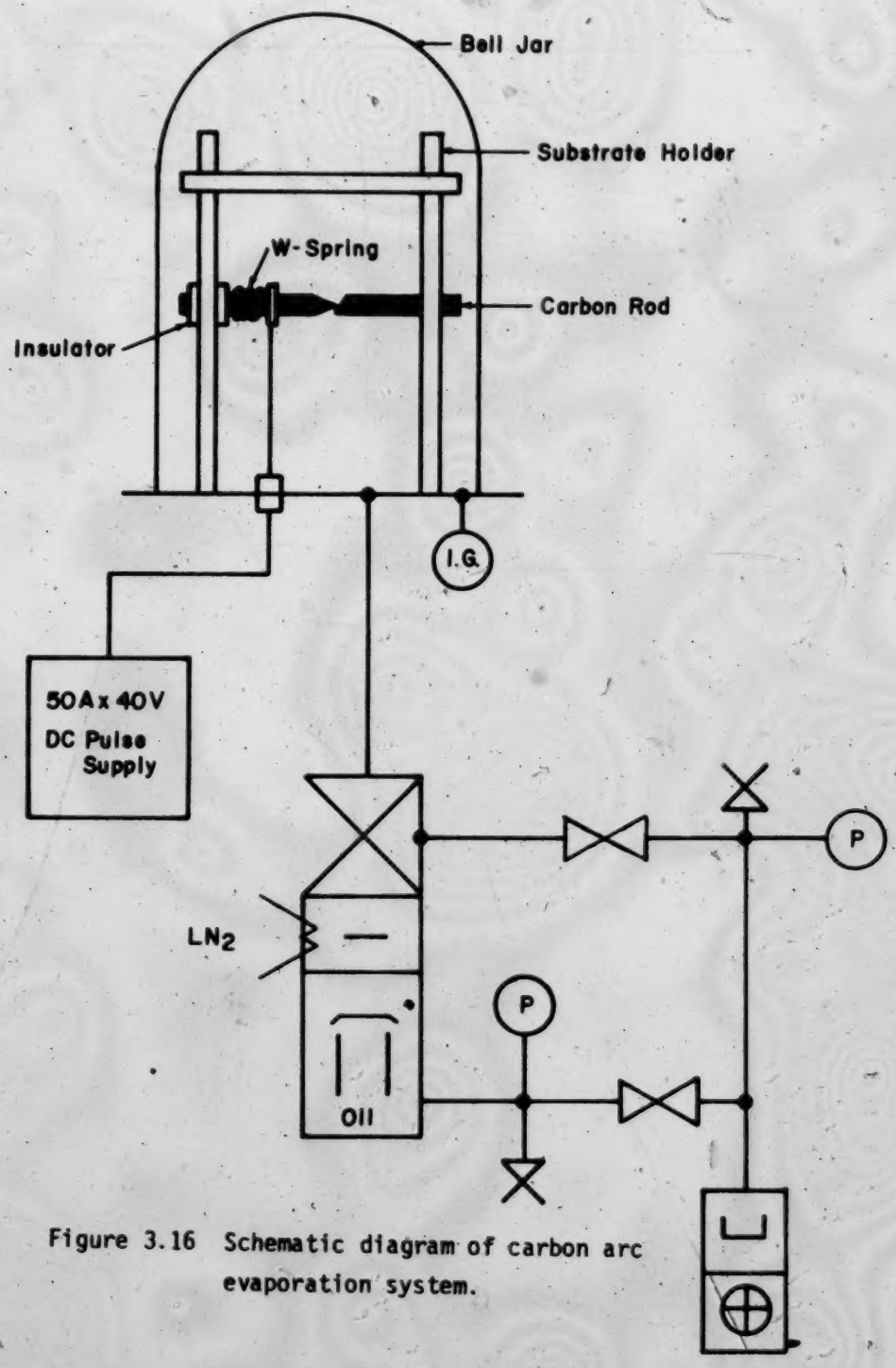

Figure 3.16 Schematic diagram of carbon arc evaporation system.

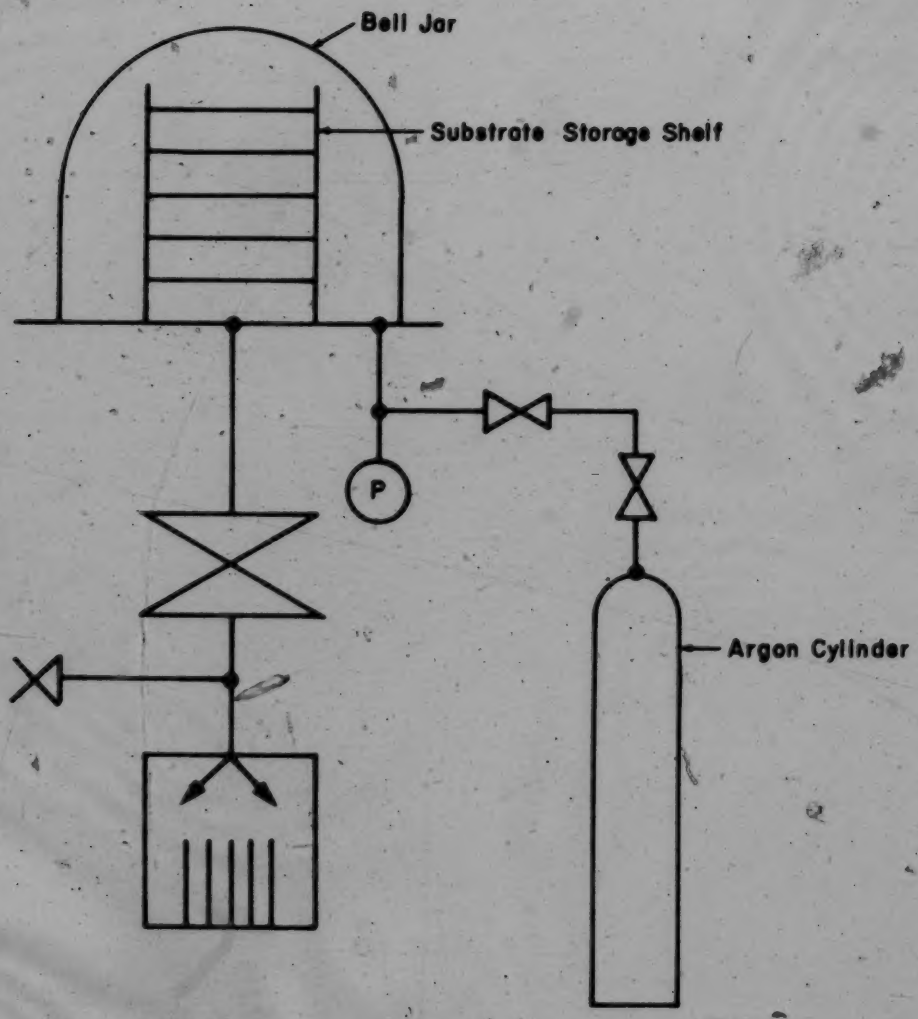

Figure 3.17 Schematic diagram of substrate storage system.

3.4 Conclusion

The prototype ion beam deposition system has met the operational requirements for the production of highly pure thin films. The operational characteristics are as follows:

Vacuum condition	: 10^{-8}-10^{-9} Torr in substrate chamber
Ion Current	: 5μA to 20μA at substrate
Mass Selection	: 0 - 600 a.m.u.
Mass Separation	: $M/\Delta M = 10$
Ion Energy	: 10eV - 4keV
Substrate	: metal, semiconductor, insulator, various sizes and shapes.

Chapter 4

Low Energy Ion Beam Deposition of Pb and Mg Thin Films and Analysis of Deposits

4.1 Introduction

Lead (Pb) and Magnesium (Mg) thin film were deposited by the proto-type ion beam deposition system described in Chapter 3.

Pb and Mg were chosen as deposition materials for the following reasons:

(1) low vaporization temperatures,

(2) large mass difference,

(3) large sputtering yield difference.

Table 4.1 shows the physical properties of Pb and Mg.

The film characteristics, such as composition, purity, thickness, surface structure and crystalline structure were investigated by using various diagnostic methods. The relationships between the incident particle energies and the consequent film characteristics was the main interest of the investigations.

This chapter is divided into three sections. In the first section, the various techniques which were used to analyse the deposits are described. In the second section, the results of Pb ion beam deposition and film analysis are presented. In the final section, the results of Mg ion beam deposition and subsequent analysis of the deposits are described.

Element	Symbol	Atomic No.	Atomic Weight	Vaporization Temperature at 10^{-3} torr (°C)	Solid Density gm/cm^3	Solid Crystal Structure	Isotope and Natural Abundance (%)	Sputtering Yield
Magnesium	Mg	12	24.31	383	1.74	Hexagonal	$^{12}Mg^{24}$ 78.7 $^{12}Mg^{25}$ 10.13 $^{12}Mg^{26}$ 11.17	low
Lead	Pb	82	207.19	625	11.34	F.C.C.	$^{82}Pb^{204}$ 1.48 $^{82}Pb^{206}$ 23.6 $^{82}Pb^{207}$ 22.7 $^{82}Pb^{208}$ 52.3	High

Table 4.1 Properties of Pb and Mg

4.2 Analytical Methods

In order to investigate characteristics of Pb and Mg thin films in terms of compositional and structural properties, the following analytical techniques were used in this research work;

composition	:	Rutherford Backscattering (RBS) Analysis
surface structure	:	scanning electron microscopy (SEM)
crystalline structure	:	transmission electron microscopy (TEM) and X-ray diffraction Analysis

4.2.1 Composition Analysis - RBS Analysis

When MeV light ion beams are incident on to a target, the incident particles lose their kinetic energy in the target because of nuclear collisions. By measuring the energy spectrum of backscattered particles, information about the mass identification and depth distribution of target materials, as well as atomic identification of impurities, can be obtained with typical depth resolution of 100 to 300Å [1,2]. This technique is most suitable for thin film systems of thicknesses of several thousand Angstroms. The application of RBS analysis to various thin film studies, such as interdiffusion and growth process has been discussed in detail in a recent conference [3].

The energy loss mechanism of the incident ion is divided into two processes:

(1) individual scattering events due to the Coulomb repulsion between the nuclei of the incident ion and a target atom,

(2) collisions between the ion and the electrons of the target atom.

The first process provides information about the atomic mass of the target material. The mathematical representation is [4].

$$E = K_M E_o$$

E : the energy of the backscattered particle

E_o : the energy of the incident particle

K_M : the kinematic recoil factor

$$K_M = \left(\frac{M_o \cos\theta + \sqrt{M_o^2 - M_1^2 \sin^2\theta}}{M_o + M_1} \right)^2$$

M_o : atomic mass of the incident particle

M_1 : atomic mass of the target particle

If $\theta \simeq 180°$ and $M_o > M_1$, then

$$E = \left(\frac{M_o - M_1}{M_o + M_1} \right)^2 E_o$$

The second process provides information about the depth perception of the target material by using existing electronic stopping power data of the target material. The mathematical re-

presentation is expressed as:

$$\Delta E = [s]t$$

ΔE : energy width of the signal spectrum

t : thickness (depth) of the target material

$[s]$: energy loss parameter

For regions near the surface $[s]$ can be written as [4].

$$[s] = K_M \frac{dE}{dx}\Big|_{E_o} + \frac{1}{|\cos\theta|} \frac{dE}{dx}\Big|_{K_M E_o}$$

$\frac{dE}{dX}$: the electronic stopping power of the target material.

Therefore t is calculated by:

$$t = \frac{\Delta E}{K_M \frac{dE}{dX}\Big|_{E_o} + \frac{1}{|\cos\theta|} \frac{dE}{dX}\Big|_{K_M E_o}}$$

The RBS analysis was carried out by 2.8 MeV to 3 MeV $^4He^+$ ion beams obtained by a 5.5 MeV Van de Graaff accelerator. This energy range was chosen because of the stability of the accelerator and absence of nuclear resonances [5,6]. The ions backscattered through 170° were collected by a silicon surface barrier detector with an active area of 25 mm^2 and 500 μm sensitive depth (ORTEC

A-016-025-500). The quoted alpha resolution of this detector is 15.4 KeV FWHM [7]. The detector was placed 12 cm from the target. He^+ ion currents of ~100nA were used to obtain each backscattering spectrum over a 15 minute period for this target - detector configuration. Figure 4.1 shows a schematic diagram of the RBS system together with the data handling system. The total counts were adjusted by pre-setting the total ion current dosage at the target. The signals from the detector were amplified and analyzed by a multichannel analyzer. The analyzed spectrum was taken by Honeywell 516 minicomputer. The final data printouts or drawings were made by SDS 940 minicomputer.

4.2.2 Surface Structure Analysis

The surface topography was investigated by using a Cambridge Stereoscan, model S-4, scanning electron microscope. The SEM is one of the most versatile instruments for the examination of the microstructure of solid surfaces [13, 14]. In the SEM, the secondary electrons ejected by the high energy electron bombardment provide information of the surface structure of the specimen. A three-dimensional image of the surface topography can be obtained in the microscope because of its large depth of field. Specimen preparation is relatively easy for SEM. A thin film of Pb and Mg was directly deposited onto a carbon specimen holder which was then placed into the microscope and tilted at 45° with respect to the incident electron beam in order to give depth contrast in the micrographs.

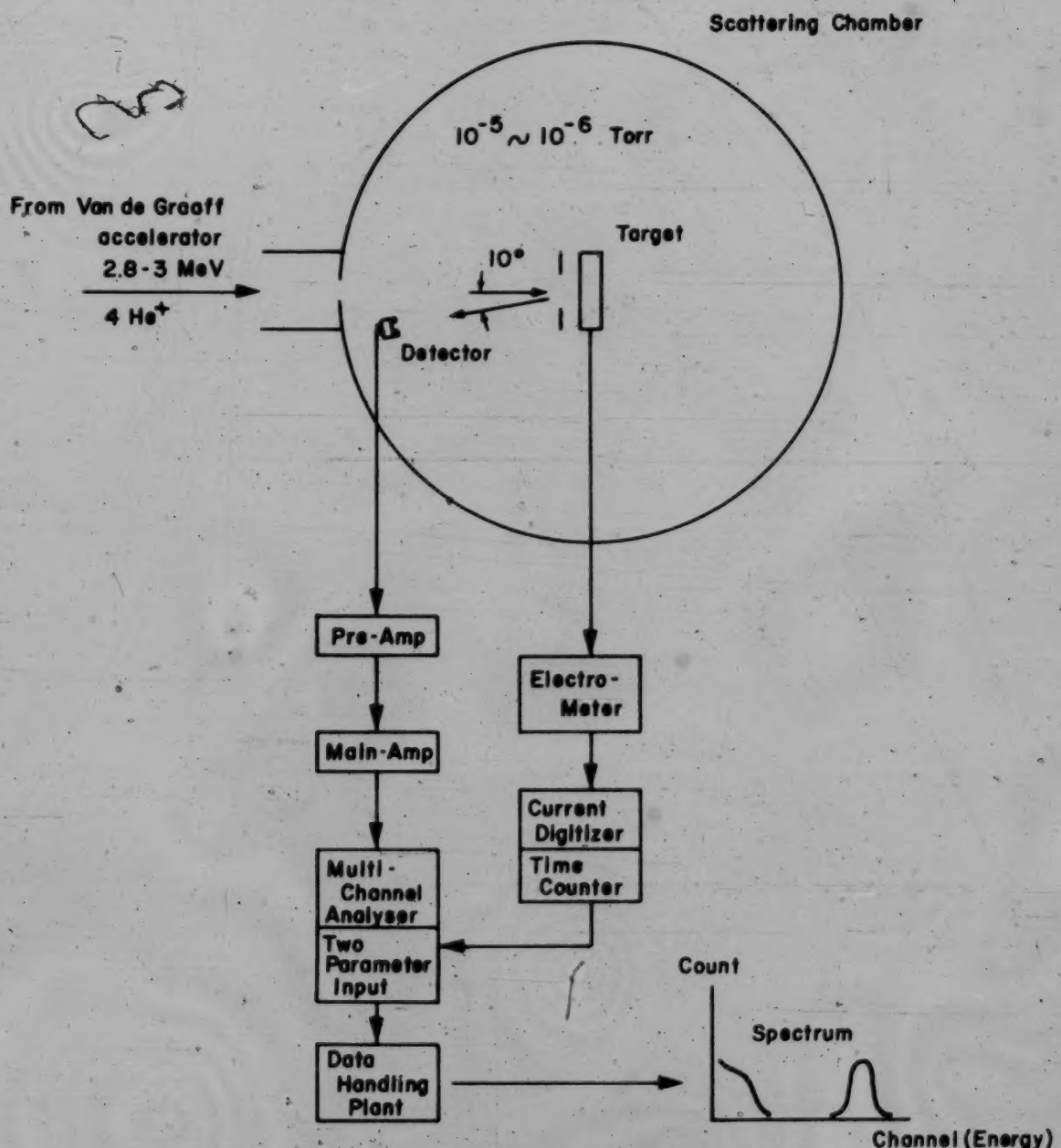

Figure 4.1 Schematic diagram of RBS system with data handling system.

4.2.3 Crystalline Structure Analysis

One of the well established methods for analysis of thin film structure is transmission electron microscopy [8, 9]. The crystal structure and crystalline orientation as well as microstructure of the thin film can be determined by using the TEM. The crystal structure and crystalline orientation is determined from the transmission electron diffraction patterns of the thin films. The microstructure is obtained by imaging the thin film at a high magnification.

The diffraction pattern will be regularly spaced diffraction spots for a single crystal specimen and will be in the form of concentric rings for a polycrystalline specimen. Figure 4.2 shows a schematic representation of the electron scattering, intensity distributions and final diffraction patterns from the single crystal and the polycrystalline specimen [10]. The diffraction maxima occurs when the electron waves, which are scattered by particular lattice plane orientation, are in phase and combine constructively as the electrons pass through a crystalline specimen. Electron waves scattered from the lattice planes lying at all other orientations will be out of phase and interact destructively, and consequently no diffraction maxima will occur.

A particular advantage of transmission electron diffraction is that a diffraction pattern of a selected small area of the specimen, which may be a single crystal, can be easily obtained by controlling

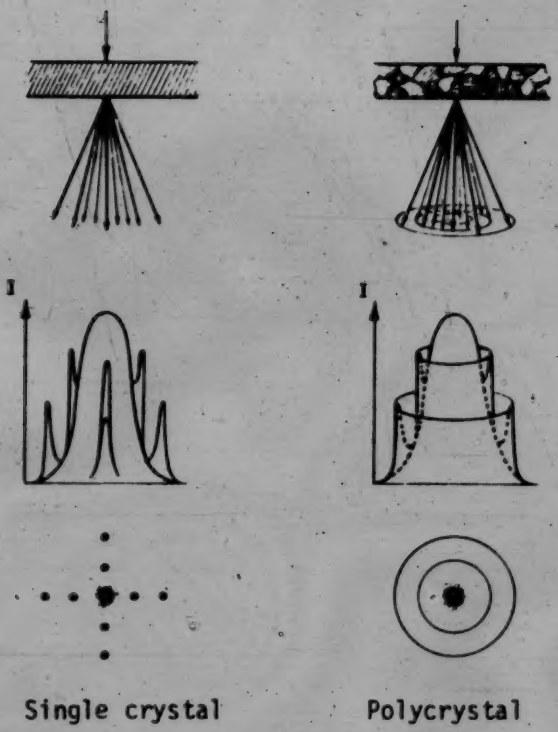

Figure 4.2 Schematic representation of electron scattering and diffraction pattern.

the size of area aperture.

The main disadvantage of TEM is the destructive nature of this method. In order for electrons to pass through the specimen, the thin films have to be stripped from the substrates, or the substrates have to be thinned to less than 1000Å after the deposition of thin films.

The microscope which was used in this research work was a JEOL (JEL-7A)TEM with 80 kV electron accelerating voltage which corresponded to relative wavelength of 0.042Å. The Pb deposits on a self-supporting carbon film were mounted on specimen support grids after flotation on water. For a NaCl substrate the supporting carbon film was deposited on top of the Pb deposits. The NaCl substrate was then dissolved by water, and the floating film was mounted onto the support grid.

Neutralized Mg thin films could not be deposited onto the thin film carbon substrate or NaCl crystal substrate (see section 4.4.3 for details). Consequently, X-ray diffraction techniques were used for the investigation of Mg film structure. The X-ray diffraction technique is relatively easy and convenient because no vacuum system is necessary and precise control of focusing condition are not necessary [11, 12]. The diffraction patterns represent the superposition of thin film structure and substrate structure because of deep penetration of the X-ray.

Using an Enraf-Nonius (Diffractis 601) diffraction generator, a

diffraction pattern was obtained by the so-called pinhole photograph mode which utilizes monochromatic radiation to examine a polycrystalline specimens. Polaroid photographs were taken by grazing angle reflection of X-rays: the specimens were tilted 10° to the incident X-rays. Ni-filtered copper radiation (λ = 1.54Å) was used as a monochromatic X-ray source.

4.3 Pb^+ Ion Beam Deposition and Analysis of Deposits

Typical operational conditions for the Pb^+ ion beam deposition are given in Table 4.2.

total ion dosage:	0.25 Coulomb
ion current:	9μA - 12μA
bombardment time:	7 ∿ 55 hours
energy at extraction:	+ 4KeV
energy at deposition:	+ 24eV to 300eV
vacuum environment:	1×10^{-8} Torr

Table 4.2 Operational condition for Pb^+ beam deposition

For the purpose of this study the ion energy alone was intentionally varied in order to investigate the characteristics of the resulting deposits. With this particular ion beam deposition system, the maximum Pb^+ ion current of 9μ - 12μA necessitated deposition

times of 7 - 5.5 hours for a total dosage of 0.25 Coulombs for each coating, which was chosen as a standard value, because this value yields bulk density deposits of an area of 2mm x 25mm with a thickness of 1μm, if unity condensation of the ion beam occurs.

The incident Pb^+ ion beam was focused into a rectangular shape and deposited onto a substrate. The ion source and the ion beam transportation system were manually adjusted to obtain maximum ion current at the substrate, however, the stability of the system is such that infrequent adjustments are necessary for Pb^+ and Mg^+ ion beams.

The statistical nature of the Pb^+ deposition and analysis of deposits are shown in Table 4.3. The reproducibility of the films was excellent; the variation in measured thickness and width of the deposits for each deposition energy are within $\pm$ 10%. Consequently the reproducibility of this deposition method is considered to be adequate for various thin film applications.

4.3.1 Low Energy Pb^+ Ion Beam Deposition

The Pb deposits are characterized by two distinct visual features. In the central area where the ion current density is highest, a thick, gray deposit (area I) merges gradually into a thin reflective deposit (area II). Figure 4.3 shows variations of deposit width as a function of incident ion energy. The deposit width distribution corresponds to that of Figure 3-14 for an energy range less than 100eV. However, for the higher Pb^+ ion energy deposition (more than 150eV), only area II was observed. No deposits were observed at energies higher than 200eV, i.e., the self-sputtering dominated over the deposition.

Deposition Energy (eV)	Number of Pb films deposited on various substrates: Poco Graphite	SEM Sample holder	Carbon Thin films	NaCl Single Crystal	Number of Samples Analysed: RBS	SEM	TEM
24	4	2	2	2	3	2	2
48	5	3	2	2	4	2	2
72	4	3	2	2	3	2	2
121	2	2	2	2	2	2	2
169	2	-	-	-	2	-	-
217	1	-	-	-	-	-	-
266	1	-	-	-	-	-	-

Table 4.3. Statistical Nature of Pb^+ deposition and analysis of deposits.

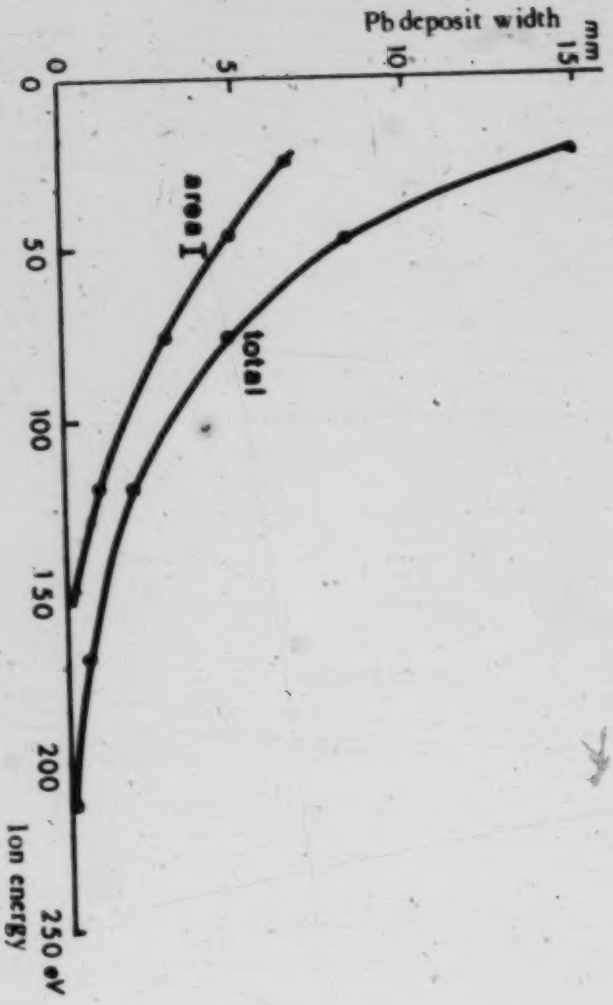

Figure 4.3 Pb deposit width as a function of incident ion energy.

The self-sputtering effect was monitored, as the deposition energy was increased, by observing the circular Pb deposits collected on the back of the decelerator plate situated 10mm in front of the substrate. The sputtered deposits were not seen below Pb^+ ion energies of 24eV. At 48eV, a small circular deposit was observed. This deposit increased in size as the ion energy increased, and above 200eV, the size of deposits were over 5cm in diameter.

A high energy self-sputtering study revealed that the self-sputtering yield of Pb is almost equal to that of Au (Figure 2.2). Also, the self-sputtering yield was found to be consistent with the noble-gas sputtering yield for low energy sputtering (Figure 2.3). Therefore, by combining this experimental observation of Pb self-sputtering with the low energy Au sputtering studies [15, 16], the self-sputtering threshold energy for Pb is considered to be roughly 24eV. The self-sputtering yield approaches unity at an incident energy of approximately 200eV.

Although no special cleaning technique was applied to the substrate surfaces, the adhesion of Pb films onto the substrates was strong. All Pb films passed the "scotch-tape test" [17]; surface carbon was stripped by the tape except in the area of the deposits. The main reasons for good film adhesion may be summarized as:

(1) substrate sputter-cleaning by the ion beam during deposition,

(2) provision of a high energy flux to the substrate surface by the energetic incident particles

(3) modification of the surface and interfacial structure due to the ion bombardment.

4.3.2 R.B.S. and S.E.M. Analysis

From three to nine RBS spectra and three surface topographies were obtained from different sites on each substrate in order to compare the characteristics of the deposits.

Impurity content

Figure 4.4 shows a spectrum obtained from the central area of a freshly-deposited film from a 48eV Pb^+ ion beam. High count statistics were taken to emphasize the substrate carbon edge with respect to the Pb peak and to search for possible impurity peaks. No detectable impurity species peaks were observed other than those of carbon and lead.

The sensitivity of the RBS techniques is about 10^{-2} - 10^{-1} monolayer for light mass atoms and 10^{-4}-10^{-3} monolayer for heavy mass atoms. Therefore, the impurity levels in the Pb film are less than 0.1 atomic % for heavy masses and less than 10 atomic % for light masses.

RBS analysis has been shown to detect impurities incorporated within thin film structures prepared by vacuum evaporation and sputter deposition [18]. In general, these impurities originated from the crucibles used in vacuum evaporation or from the supporting gas used during sputter deposition. Even when the limited sensitivity of the RBS techniques is considered, especially for low-mass impurities, the ion beam deposition technique produces a Pb deposit which is considerably purer than those obtained by using more conventional techniques.

The relative purity of the ion beam deposited Pb films is in the magnitude of 2 to 10 higher than films prepared by conventional methods and analyzed by RBS [18].

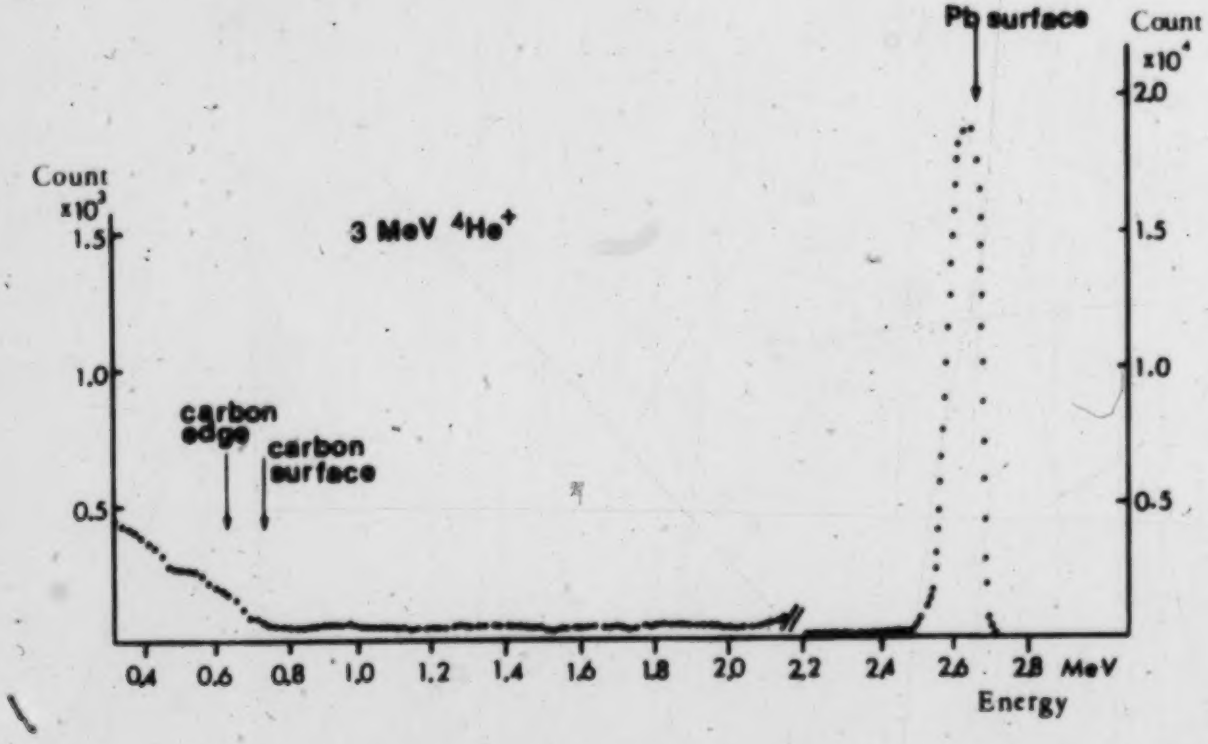

Figure 4.4 RBS spectrum of 48 eV Pb deposit

The Pb deposits are considered to consist of several Pb isotopes i.e. Pb^{204} Pb^{206}, Pb^{207} and Pb^{208}, because the velocity filter is not capable of separating isotopes of heavy ion beams (refer to Figure 3-9 and 3-12).

Pb Deposit Density and Thickness

Figure 4.5 shows the portion of the RBS spectra containing the yield from the center of the Pb deposits for a range of ion beam energies. A spectrum from bulk Pb is also shown for density comparison. By comparing the peak heights, the atomic density of the Pb deposits can be estimated.

All RBS analysis were carried out by using 2.8 eV $^4He^+$ ion beam. Electronics were adjusted so that the channel width δE= 2.87 KeV/ channel was obtained. The following factors were calculated for this energy in order to estimate film thickness;

the kinetic recoil factor $K_{Pb} = 0.9262$

the energy loss parameter $[S]_{Pb} = 61.8$ eV/Å

The electronic stopping powers were obtained from the available data table [19]. Table 4.4 shows the density, energy width at FWHM and corresponding average film thicknesses as a function of Pb deposition energy.

Pb^+ ion energy (eV)	film atomic density / bulk density (%)	Energy width of FWHM (KeV)	Film thickness (Å ± 200Å)
24	64	155	2500
48	97	115	1900
72	100	77.4	1300
121	80	51.6	850
169	35	31.5	500

Table 4.4 Density and thickness of Pb deposits

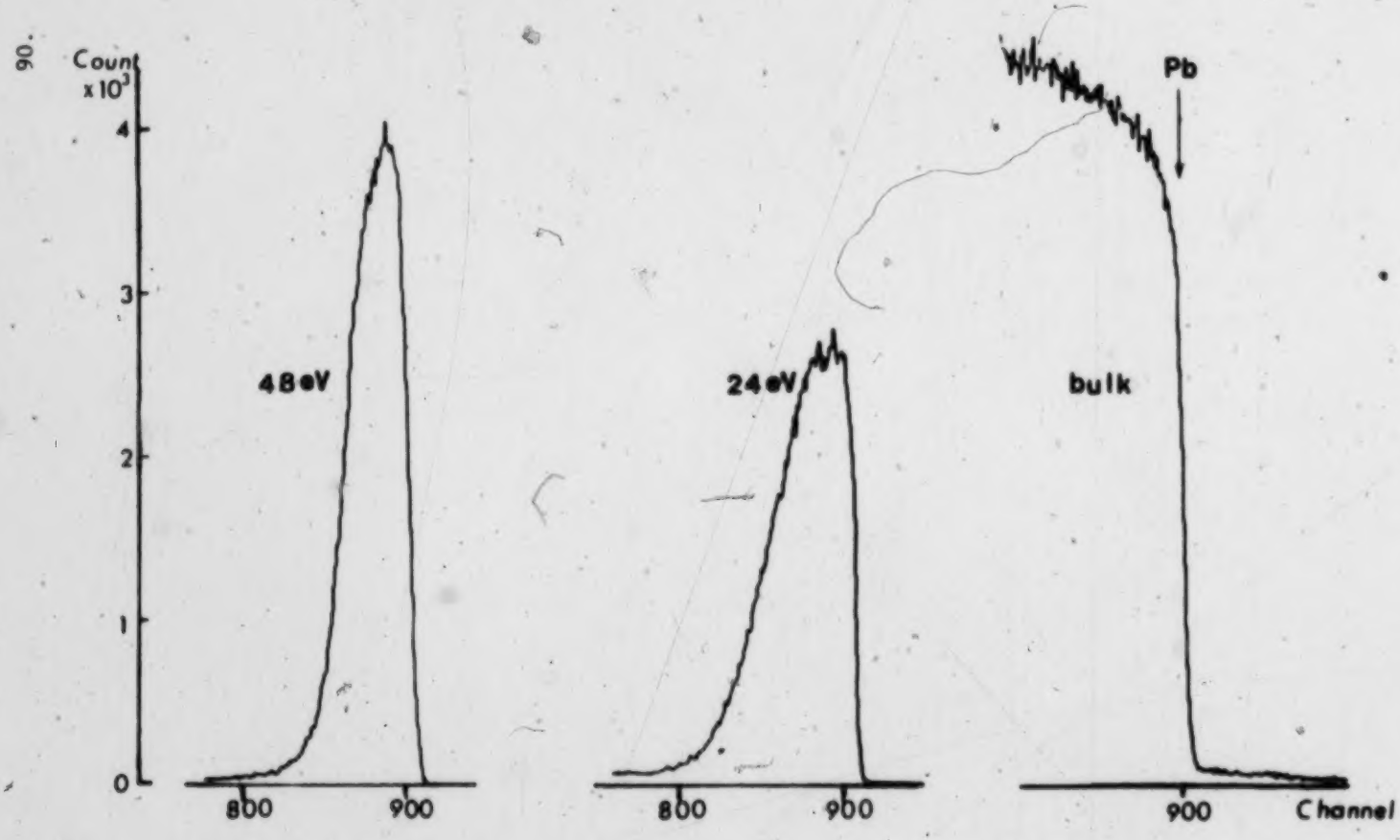

Figure 4.5 RBS spectra of center of Pb deposits.

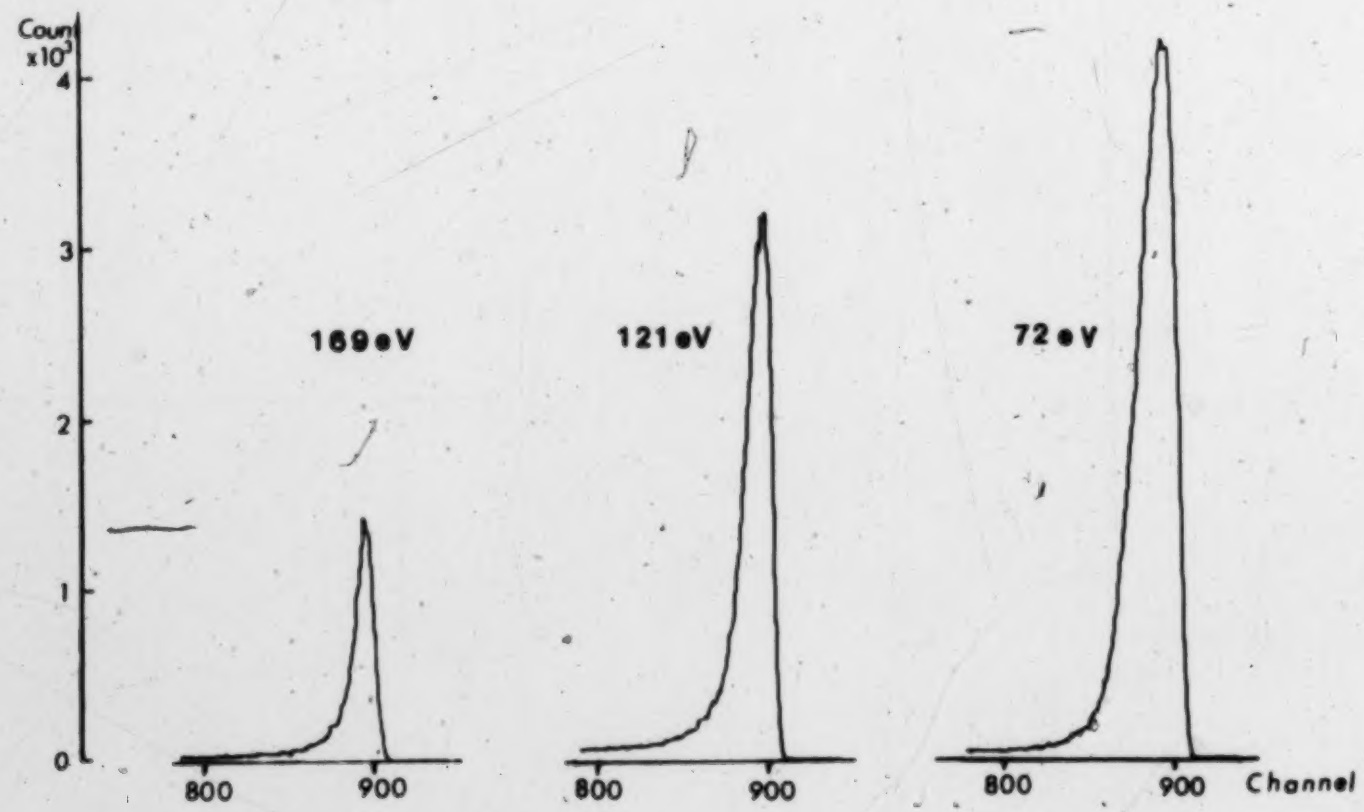

Figure 4.5 RBS spectra of center of Pb deposits.

At 24eV deposition, a relatively thick deposit with a low atomic density is obtained. Atomic density of deposits reaches bulk density at 48eV and 72eV, but deposit thicknesses decrease from their maximum at 24eV.

It is known that the backscattering yields are proportional to the number of atoms/cm^3 for a continuous film. However, this yield will decrease for discontinuous films, and the amount of the decrease in yield is proportional to the fraction of uncovered area [20]. The surface topography for 24eV deposit shows a thick film with deep channels (Figure 4.6(a)). Namely, for 24eV Pb^+ deposition, the deposit has to be a relatively thick film (more than 2500Å) before the total coverage of the substrate surface is achieved. On the other hand, for 48eV and 72eV Pb^+ deposition, full surface coverage is achieved with relatively thin films. In order to obtain totally continuous films, deposition of total 0.5C Pb^+ ion dosage was carried out for 24eV and 48eV. Both deposits showed the thick bulk density films; 48eV deposit (4000Å) was thicker than that of 24eV (3500Å) due to less spreading of the films.

For ion energies higher than 72eV, the effect of self-sputtering predominates over deposition and both thickness and atomic density decrease.

Scanning electron microscopy was used to visually inspect the area of interest. Figure 4.6(a) - (d) show SEM micrographs from area I for increasing energies. At 24eV the deposit shows a thick film feature with a gentle hill and valley surface. The deep channels

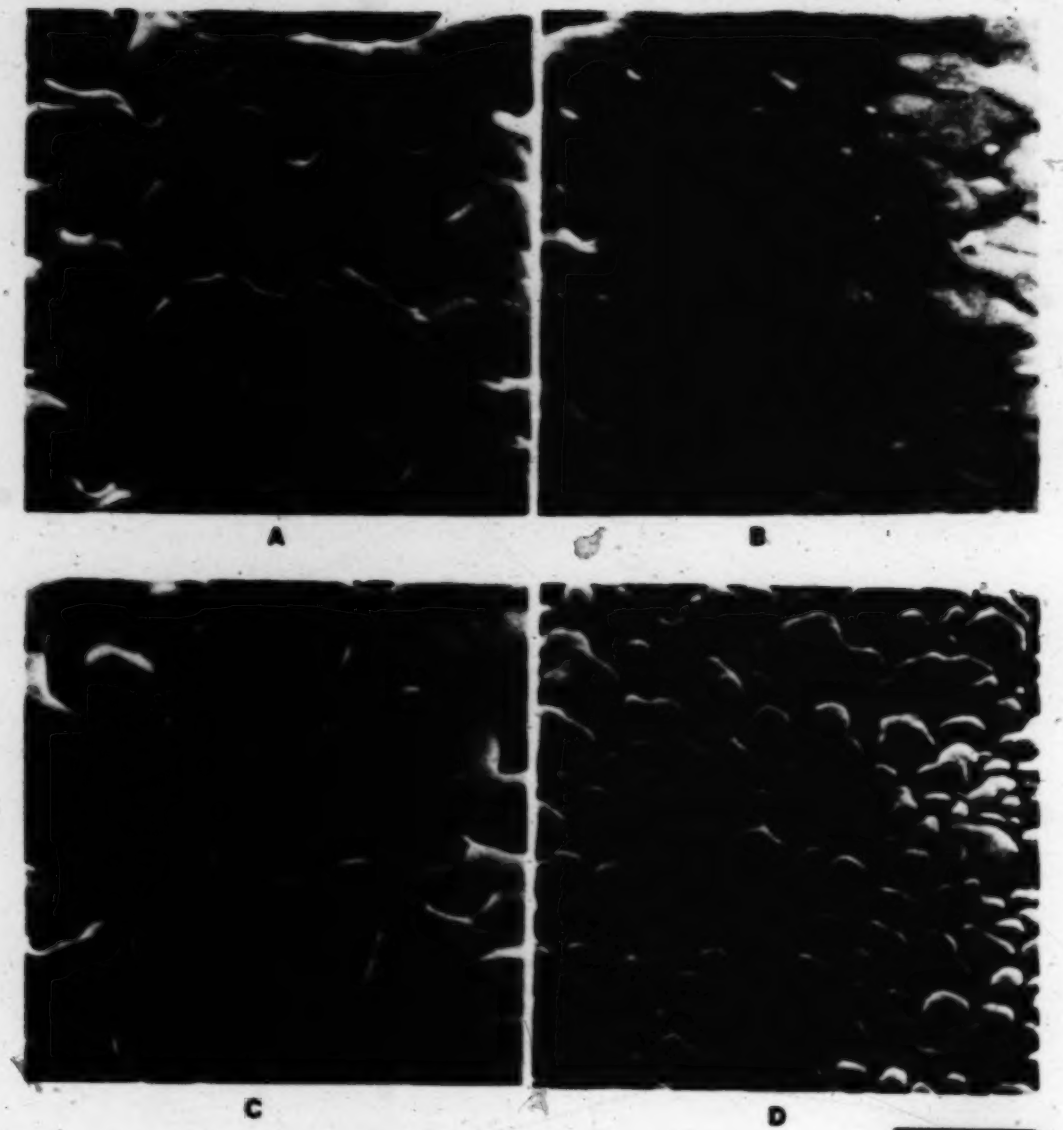

Figure 4.6 Surface topographs of the center of the Pb deposits, (a) 24 eV, (b) 48 eV, (c) 72 eV and (d) 121 eV deposition energies.

reaching to the carbon substrate are clearly seen. As the deposition energy is increased to 48eV, the surface becomes flat and continuous with large grains, similar to that of annealed and recrystallized films [21]. At 72eV the deposit shows the flat thin film feature with large holes. At 121eV the deposits are no longer continuous, showing a liquid-like coalescence state with the formation of flat-topped islands.

A second feature of the RBS spectra from the Pb peaks is the gradual decrease of the yield on the low energy edge of the peak, which is almost common for all peaks. This is thought to be caused by the non-uniformity of the film thickness, because 1) the incident $^4He^+$ ion beam (probe) diameter is roughly 2mm, and 2) the deposit distribution is roughly bell-shaped (Figure 3-14). Within a 2mm probe diameter, the film thickness is then assumed to be non-uniform, which results in a low yield on the low energy edge of the peak.

Deposit Thickness Distribution

The deposit thickness distribution across the face of the deposit was also investigated. Because of the spreading of the beam just before deposition due to space-charge expansion, the effect of ion dose and the deposition rate on film growth can also be approximated. Since the energy spread of the beam is, at maximum, only a few eV, the ion beam energy can be considered to be constant for the entire deposition area.

Figure 4.7 shows such a RBS scan across the face of the 48eV

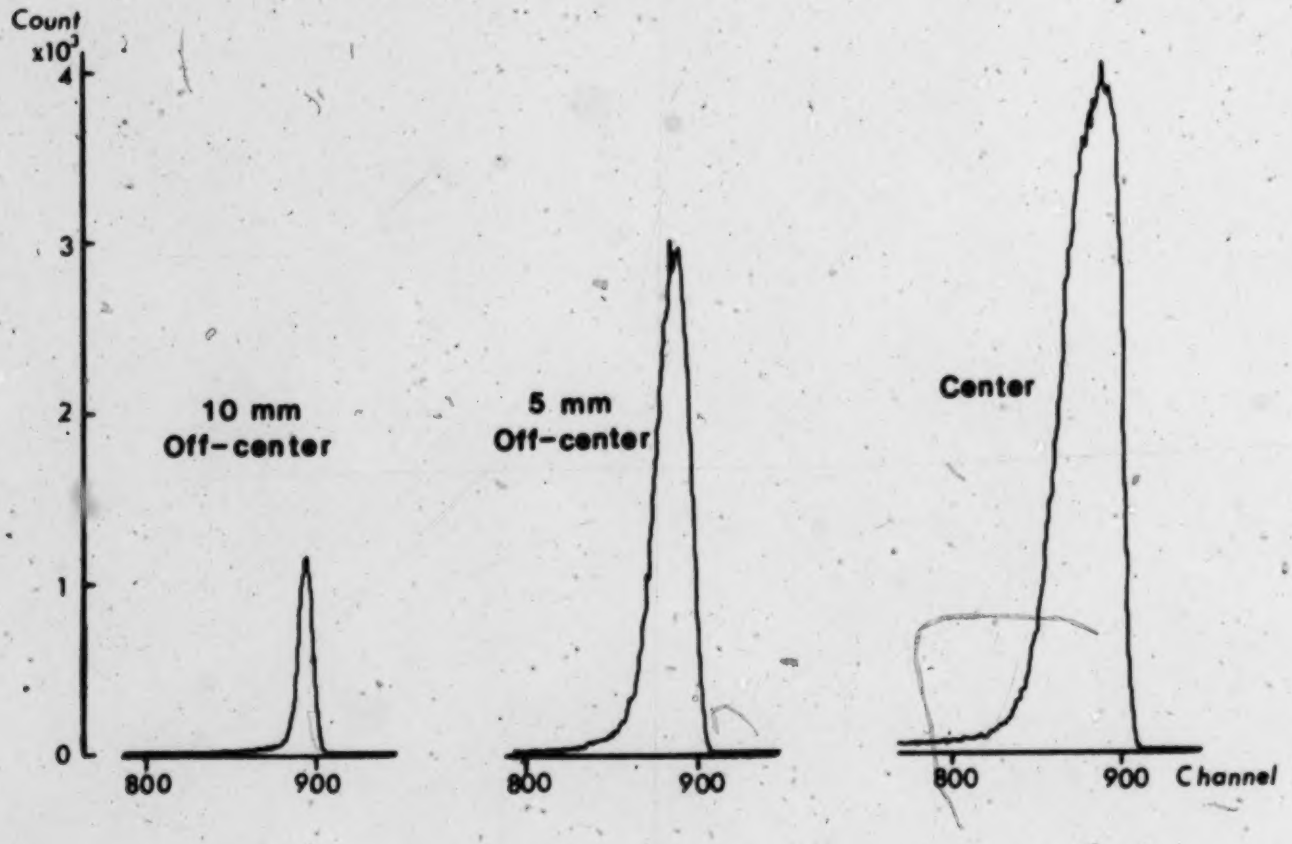

Figure 4.7 RBS scan of 48 eV Pb deposit.

deposit. Because space charge spreading is more severe at higher retardation potentials (low deposition energy), low energy deposits are wider in area than at higher energies. The RBS peaks reveal that the spreading is about a factor of ten wider than that of visual observation (Figure 4.2).

Figure 4.8 shows micrographs taken across the face of a 48eV deposit: (a) is from area I, (b) is from the transition between area I to area II and (c) is from area II. In area II, very thin deposits cover the whole area and the surface coverage is extensive at this stage. Figure 4.8 (b) shows the typical liquid like coalescence stage of film growth. This surface topography variation is common for each deposit at various energies. For low dosage, the surface is almost entirely covered by small islands of uniform size. As dosage increases, the islands increase in size, become flat-topped, and began to coalesce. At high dosage, an almost continuous film is obtained after the filling of channels and holes.

By combining both RBS and SEM data in the low dose areas (Figure 4.7 and 4.8), the deposit growth is characterized by an increase in height of the Pb peak rather than an increase in width, or by an increase in area coverage rather than an increase in thickness. However, the degree of the surface coverage and thickness is dependent on the incident ion energies. For 24eV, a rather thick film is required for total coverage, on the other hand for 48eV and 72eV, total coverage of the substrate surface can be achieved by relatively thin films.

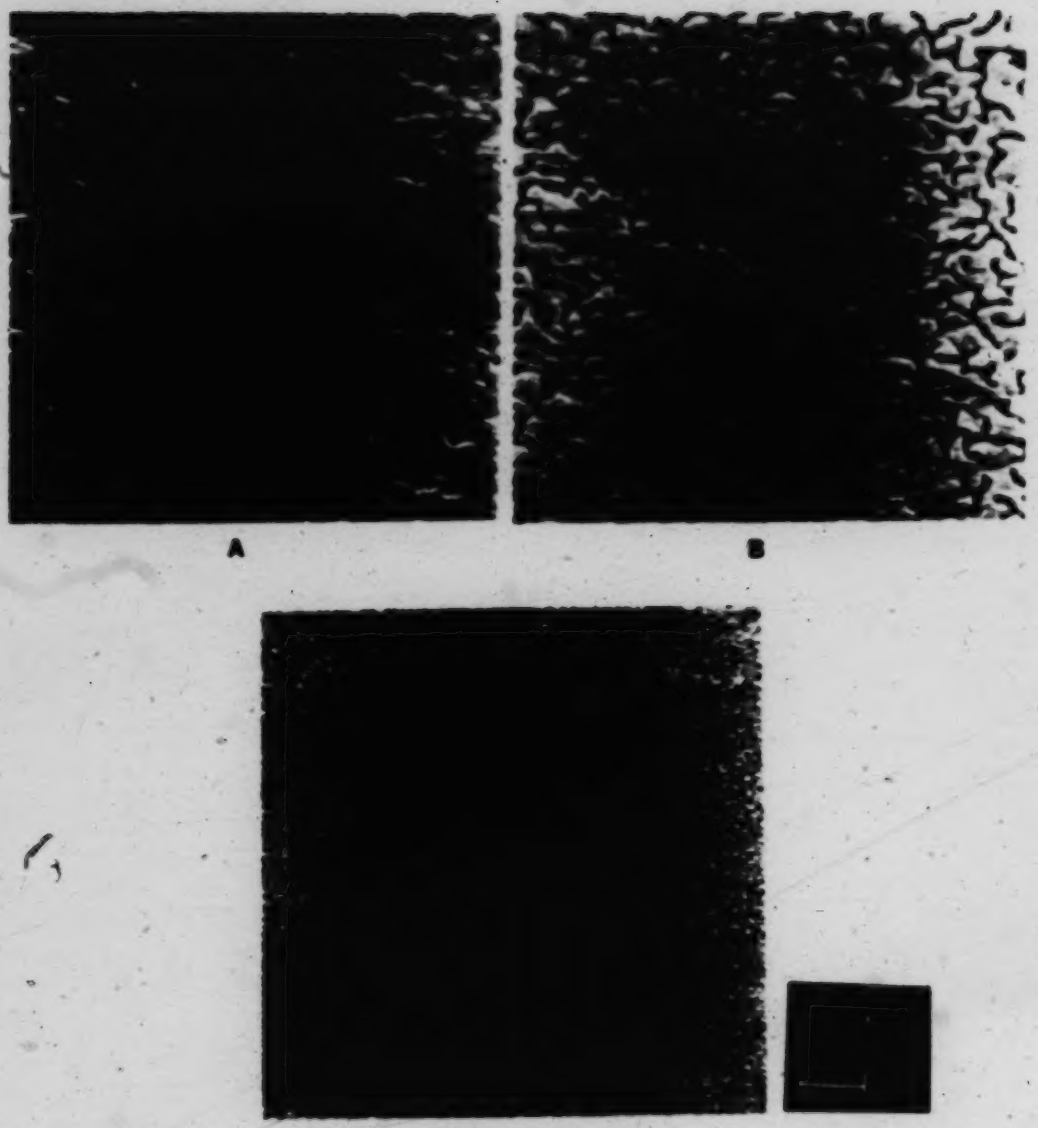

Figure 4.8 Surface topographs of 48 eV Pb deposit for various distance from deposition center, (a) deposition center, (b) 2 mm off-center, (c) 4 mm off-center.

4.3.3 TEM Analysis

In order to investigate the effect of the incident particle energies on the crystalline structure of the films transmission electron diffraction analysis was conducted by using TEM.

Thin carbon films and single crystal NaCl were used as substrates.

Figure 4.9 shows the diffraction pattern obtained from (a) carbon thin film, (b) 48eV Pb on C film and (c) 120eV Pb on C film. The substrate carbon film shows the typical amorphous structure. The 48eV Pb deposit shows the polycrystalline structure with a specific orientation. The 120eV deposit also shows the polycrystalline structure with specific orientations with larger grain sizes. Several crystalline orientations are dominant: this is clearly seen as bright rings on the diffraction pattern. (Figure 4.9 (c)).

This recrystallization of the deposit because of the incident energy increase is also clearly seen by Figure 4.10. These diffraction patterns were obtained from the Pb deposits on single crystal NaCl substrate with [100] orientation. At 24eV Pb deposit (Figure 4.10 (a)), the diffraction pattern indicates an amorphous structure. With increased deposition energy, f.c.c. structure with [100] orientation begins to appear on the diffraction pattern (Figure4.10(b)). At 120eV deposition, the diffraction pattern is similar to that of an epitaxial film. The f.c.c. structure with [100] orientation is dominant in this diffraction pattern. This structure is verified by indexing the diffraction pattern.

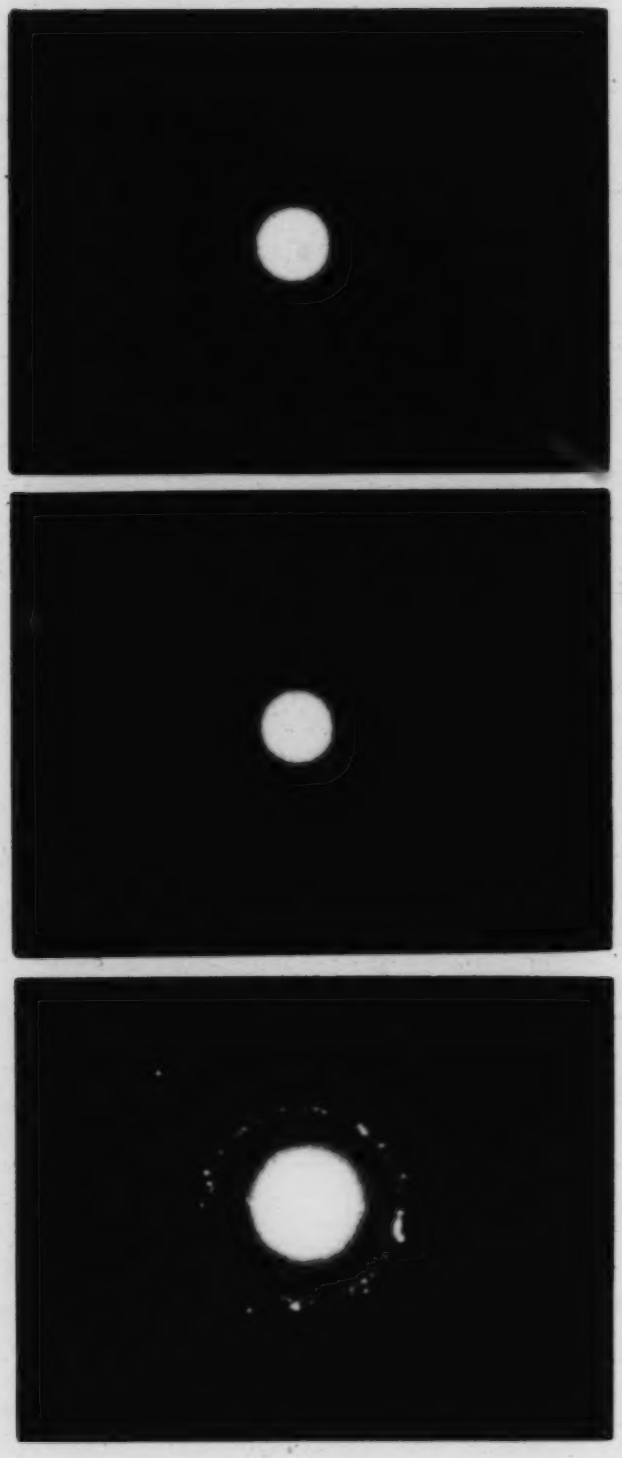

Figure 4.9 Electron diffraction patterns of (a) carbon thin film, (b) 48 eV Pb deposit on C film, and (c) 121 eV Pb deposit on C film.

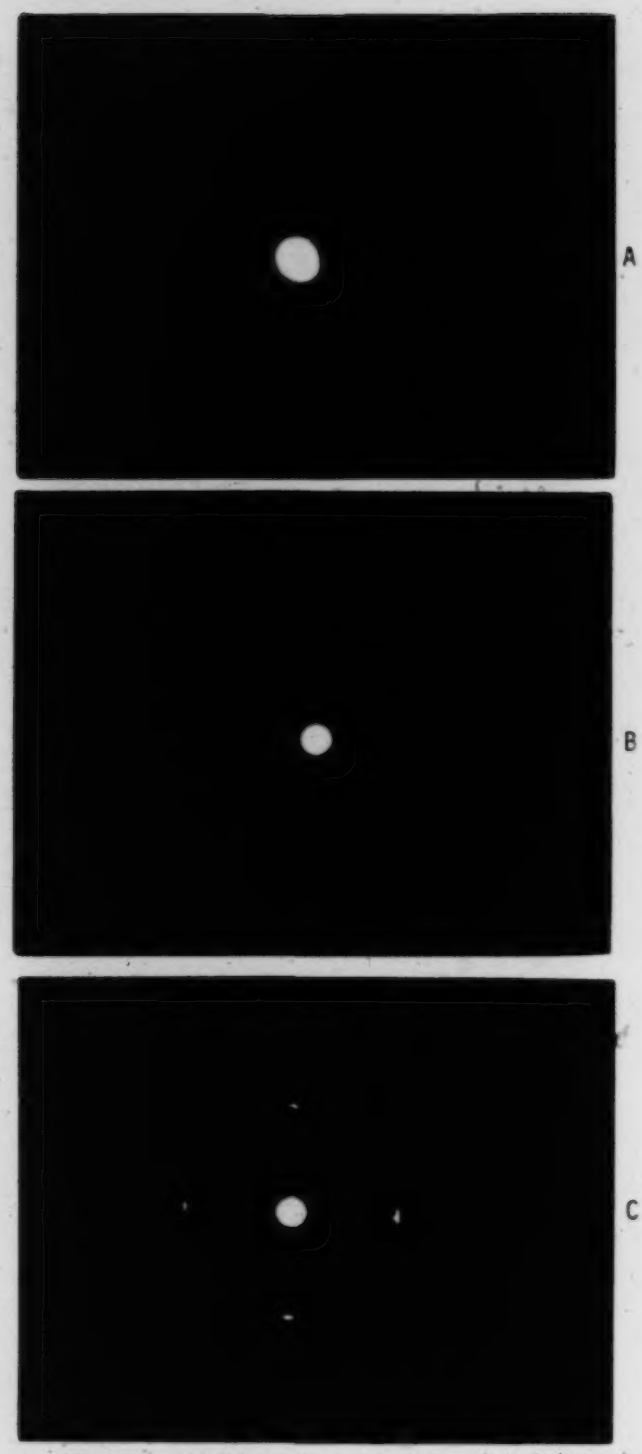

Figure 4.10 Electron diffraction patterns of (a) 24 eV Pb deposit on NaCl, (b) 48 eV Pb deposit on NaCl, and 121 eV Pb deposit on NaCl.

The d-spacing for diffraction spots is given as [22],

$$d = \frac{\lambda L}{R}$$

where λ : the wavelength of incident electron beam = 0.042 Å

L : camera length = 300mm

R : distance between the center and the diffracted spots

The shortest R_1 is 5.2mm, the

$$d_1 = 2.42\text{Å}$$

Now the miller indices of a cubic structure is given as:

$$\frac{1}{d_1^2} = \frac{h_1^2 + k_1^2 + \ell_1^2}{a^2}$$

where a is the lattice constant, and for Pb a = 4.95Å [23], then

$$h^2 + k^2 + \ell^2 = 4.$$

Therefore, the miller indices for those spots is:

$$\{ h_1 k_1 \ell_1 \} = (2,0,0)$$

The next nearest spots are also found to be:

$$\{ h_2 k_2 \ell_2 \} = (2,2,0)$$

Therefore, the dominant diffraction pattern is that of [100] orientation of f.c.c. crystal.

In Figure 4.10 (c), several distinct diffraction rings are observed inside the (2,0,0) Pb diffraction spots. These rings are speculated to be a result of either 1) NaCℓ crystal, present because of insufficient specimen washing, or 2) oxides of Pb.

The d-spacing of the innermost ring is found to be $d_1 \simeq 6\text{Å}$. If this diffraction ring were caused by NaCℓ crystal, which has a cubic structure, the smallest possible N-value from the miller indices is

$$N = h_1^2 + k_1^2 + \ell_1^2 = 3$$

Consequently the lattice constant will be about 10Å; however, the real lattice constant for NaCℓ is 5.63Å. Therefore, these diffraction rings are not from NaCℓ crystal, but are probably caused by the oxides of Pb film. The large lattice spacing (typically $5\text{Å} \sim 8\text{Å}$ [25]) of the lead oxides (orthorhombic or tetragonal structure) also supports the above statement. However, the precise indexing of the diffraction rings is rather difficult due to the nature of crystalline structure of the lead oxides.

The crystalline structure and grain size of the deposits depends on the energy of the incident ion beam; a higher order of crystalline orientation with large grain size is obtained by a higher energy deposition.

The main reasons for the recrystallization at high energy deposition are considered as follows:

1) provision of high energy flux to the substrate surface by the high energy incident particles
2) enhanced diffusion process due to high mobility of the adatoms
3) creation of defects on substrates, which in turn create preferred nucleation sites

4.4 Mg^+ Ion Beam Deposition and Analysis of Deposits

Typical operational conditions for Mg^+ ion beam deposition are given in Table 4.5

total ion dose:	0.25 Coulomb
ion current:	12μA - 15μA
bombardment time:	5.5 - 4 h.
energy of extraction:	+4KeV
energy of deposition:	+20eV to 500eV
vacuum environment:	5×10^{-8} Torr

Table 4.5 Operational condition for Mg+ ion beam deposition

The same total ion dosage as that of Pb was used for Mg^+ deposition. The ion energy alone was varied to investigate the film characteristics. The statistical nature of Mg^+ deposition and analysis of deposits are shown in Table 4.6.

The reproducibility of the Mg deposits was also excellent. The measured variation in thickness and width of Mg deposits are the same as that of Pb deposits. Consequently, the reproducibility of the Mg deposit are considered to be adequate for various thin film applications.

4.4.1 Low Energy Mg^+ Ion Beam Deposition

The Mg deposits are visually characterized by a silvery deposit on the carbon substrate. The depositions of 100eV or less exhibit double line deposits: i.e. a very thin deposit was observed beside the main deposits.

Deposition energy (eV)	Number of Mg films deposited on various substrates. POCO Graphite	SEM Samples holder	Carbon thin film	Number of samples analyzed. RBS	SEM	X-ray diffraction
24	4	2	-	2	2	2
48	4	1	1	3	1	1
72	4	1	-	2	1	1
100	2	1	1	2	1	2
120	4	-	-	2	-	-
150	2	1	1	1	1	1
170	3	-	-	2	-	-
217	3	1	-	1	1	-
300	2	-	-	1	-	-
500	1	-	-	1	-	-

Table 4.6. Statistical nature of Mg^+ deposition and analysis of deposits.

For 48eV and 24eV deposits, two line deposits are super-imposed on each other due to space charge spreading. Figure 4.11 shows deposit spreading due to the space-charge expansion. The low energy area of the curve is almost the same as that of Figure 4.3. At a higher energy range, particularly higher than 300eV, the deposits were clearly observed because of the low self-sputtering yield of Mg.

The self-sputtering effect was monitored by the same method described in section 4.3.1. The self-sputtering yield of Mg is roughly the same as that of Al (Figure 2.2). Therefore, as before, by combining the experimental observation of Mg self-sputtering with the existing data on low energy sputtering, the threshold energy for the self-sputtering of Mg is considered to be roughly 24eV. The self-sputtered yield approaches unity at an incident energy of approximately 500eV.

In contrast to Pb deposits, the adhesion of Mg deposits at low energies was rather weak. All Mg deposits less than 100eV failed the "scotch-tape" test. The deposits with 120eV or higher ion energy passed this test.

This variation of adhesion strength of Mg deposits with the carbon substrate cannot be simply explained by two body collision phenomena (Chapter 2). However, the average retained energy of Mg particles after the initial collision is about 55eV for the incident energy of 100eV, and about 70eV for the incident energy of 120eV (Figure 2.7). Therefore, Mg particles with incident energy of 100eV or lower have less possibility of making displacement of other substrate particles in further collisions. On the other hand, Mg particles with 120eV incident energy or higher can possibly make another displacement of substrate particles during the next collision. Consequently, Mg particles with 120 eV or higher

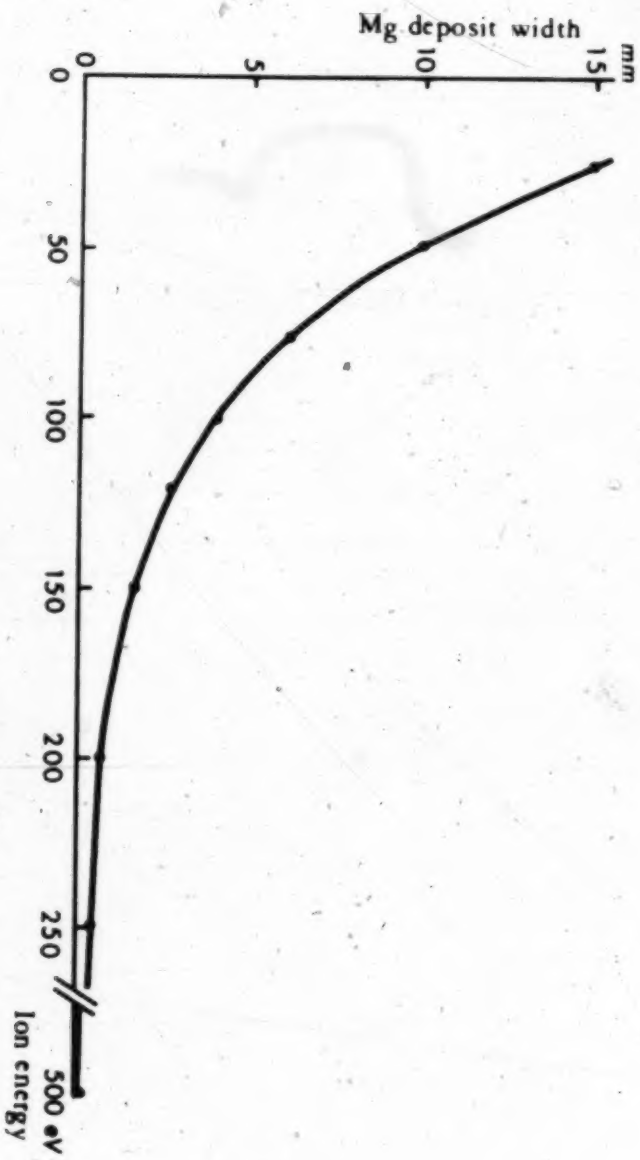

Figure 4.11 Mg deposit width as a function of incident ion energy.

incident energy have good possibility of penetrating a few atomic layers. It is also shown that the surface carbon of the substrate is loosely bonded. Therefore, Mg deposits with incident energy of 100eV or lower could be easily peeled off together with loosely bound surface carbon by the scotch tape. On the other hand, Mg deposits with 120eV or higher could be deeply anchored into the substrate and could have a stronger adhesion with the substrate.

4.4.2 RBS and SEM Analysis

Impurity Content

An oxygen peak was always observed in the RBS spectra even when Mg film was freshly deposited. This oxidization of Mg film was considered to be post-deposition oxidization for the following reasons.

1) The oxygen partial pressure was very low (less than 10^{-10} Torr) during deposition,

2) The RBS peak of oxygen was that of surface oxygen,

3) Mg is known to be easily oxidized at room temperature [24].

During the transportation of Mg deposits from the ion beam deposition system to the RBS system, or to the storage sytem the oxidization of Mg film by atmospheric oxygen probably took place very rapidly.

Except for oxygen peaks, there was no detectable impurity species in the RBS spectrum, consequently Mg deposits fabricated by the ion beam deposition method were considerably purer than those of conven-

tional deposition methods. The relative purity of Mg deposits are considered to be the same as the purity of Pb deposits.

Mg Deposit Density, Thickness and Composition

Figure 4.12 shows the portion of the RBS spectra containing the yield from the center of the Mg deposits for a range of ion beam energies.

Table 4.7 shows the density, energy width at FWHM and corresponding average film thickness. The kinetic recoil factor $K_{Mg} = 0.5171$ and the energy loss paramenter $[S]_{Mg} = 30.2$ eV/Å are used to calculate the average film thicknesses.

Mg^+ ion energy (eV)	film atomic density / bulk density (%)	energy width at FWHM (KeV)	average film thickness (Å ± 200Å)
24	83	57.4	1900
48	100	57.4	1900
100	67	57.4	1900
120	50	15	1400
170	17	-	-
300	15	-	-

Table 4.7 Density and thickness of Mg deposits

In order to obtain thicker deposits, the total ion dosage of

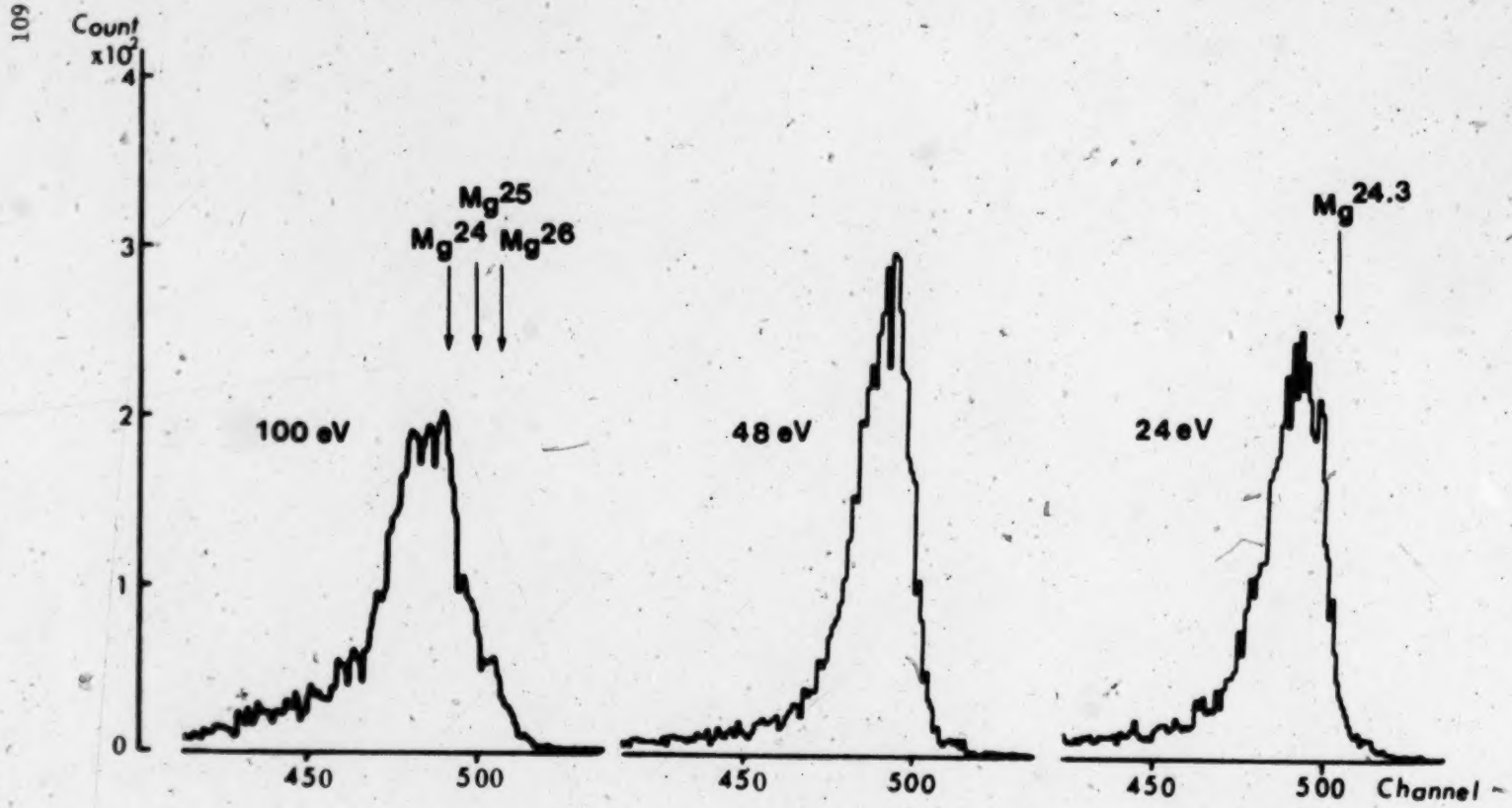

Figure 4.12 Rbs spectra of center of Mg deposits.

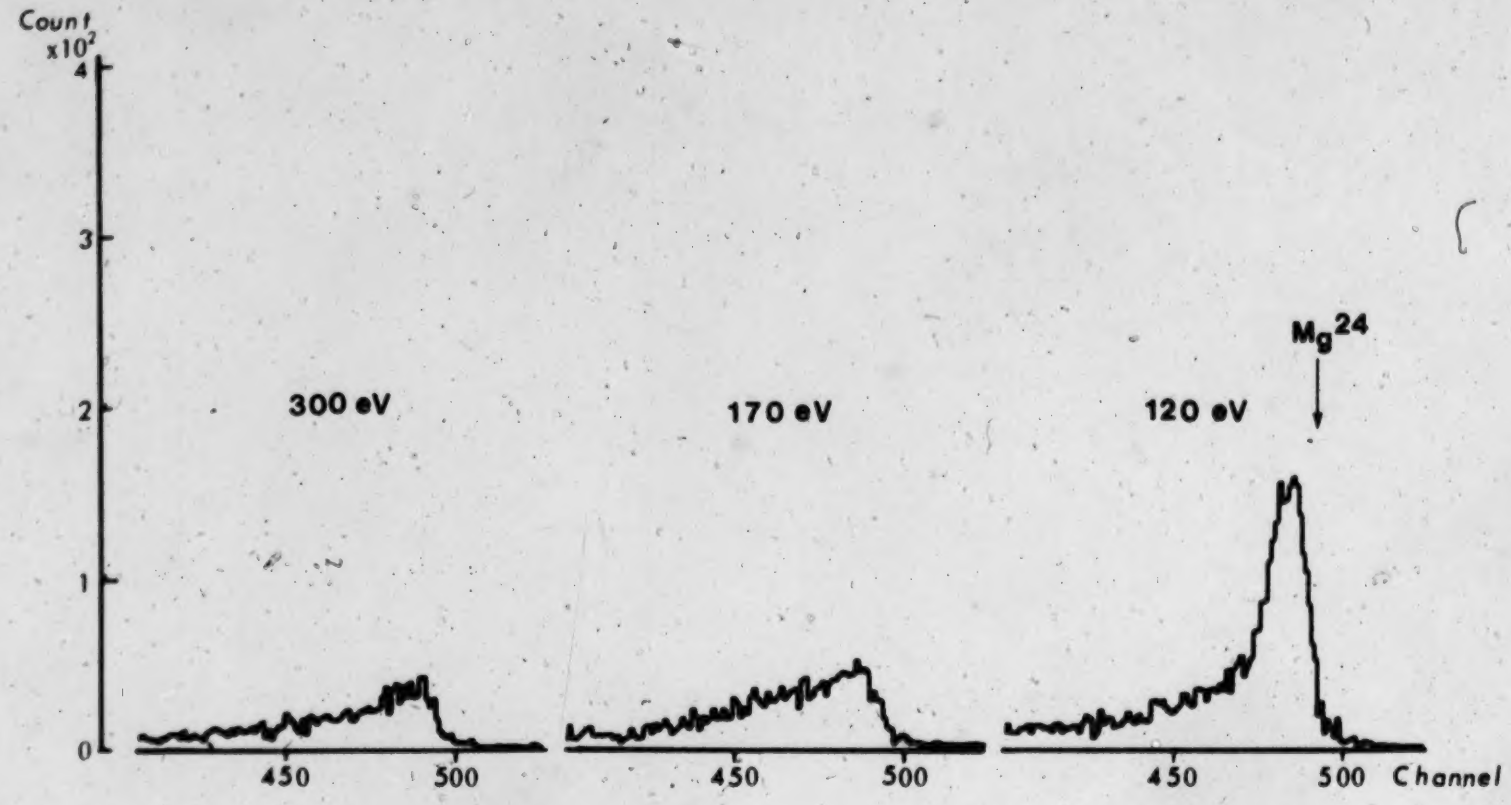

Figure 4.12 RBS spectra of center of Mg deposits.

0.5 Coulomb deposition was used at 24eV and 100eV. Both films yielded bulk density thick films: 3700Å thickness for 24eV deposit and 3300Å thickness for 100eV deposit. The decrease in thickness of film at 100eV is thought to be due to self-sputtering.

As previously described in section 4.4.1 the low energy Mg deposits are visually characterized by double line deposits. The double lines are though to result from the isotopes of Mg. The main deposition line consists of Mg^{24}, and the very thin deposition line consists of Mg^{25} and Mg^{26}. This effect is clearly seen on RBS spectra as a shift of Mg peaks. For low energy Mg deposition, Mg peaks appeared at channel 500 which corresponds to 1.44 MeV. At 100eV deposition, a peak maximum shifted to channel 494 which corresponds to 1.42 MeV, and the gradual decrease of the yield is observed on high energy edge of the Mg peak. At 120eV or higher energies, the Mg peaks appeared at channel 494 without the gradual decrease of yield on the high energy edge. 1.44 MeV corresponds to the kinetic recoil factor of 0.518 and 1.42 MeV corresponds to 0.510. These kinetic recoil factors correspond to target masses of 24.3 and 24.0 respectively. Therefore, the low energy Mg deposits (48eV and 24eV) consist of several isotopes of Mg with natural ratios. The 100eV deposit also consists of several isotopes with less heavy Mg. Deposits with energy higher than 100eV consist only of Mg^{24}.

At low energy deposition, the isotopes inter-mixed due to the space-charge expansion of the ion beams. Also, the optimization of

the deposition condition is achieved by adjusting the ion beam system so that the maximum ion current is obtained at the substrate. Therefore, the deposits at low energy probably contain several isotopes. However, at higher energy the space-charge spreading is reduced and the position of maximum ion current is shifted (Figure 3.14). Therefore, the optimum condition is obtained by choosing the ion beam of the highest intensity, i.e., Mg^{24} element (80% of total ion current). Hence, only Mg^{24} deposits are obtained at energies higher than 100eV.

The other feature of the RBS spectra of Mg peaks is the "tailing" of the yield on the low energy edge of the peak even for very small peaks which is significant for the higher energy deposition of 120eV or more. This is considered to be caused by the penetration of Mg particles into a carbon substrate, because 1) the RBS spectrum of a carbon edge exhibits a gradual increase of yield rather than a sharp increase and 2) surface topographies do not show deep channels or deep holes which are typical features of thick films.

As previously discussed, the binary collision model shows the strong possibility of deeper penetration of higher energy Mg particles into a carbon substrate. This penetration is also considered as a main reason for good adhesion of deposits with energy of 120eV or higher.

A visual inspection of the areas of interest was carried out by SEM. Figure 4.13 (a) - (d) show the surface topographies of the center of Mg deposits at various energies. At 24eV deposition, the surface topography shows a corrugated surface with pebble-like protrusions. As the deposition energy is increased, at 48eV the surface becomes flat

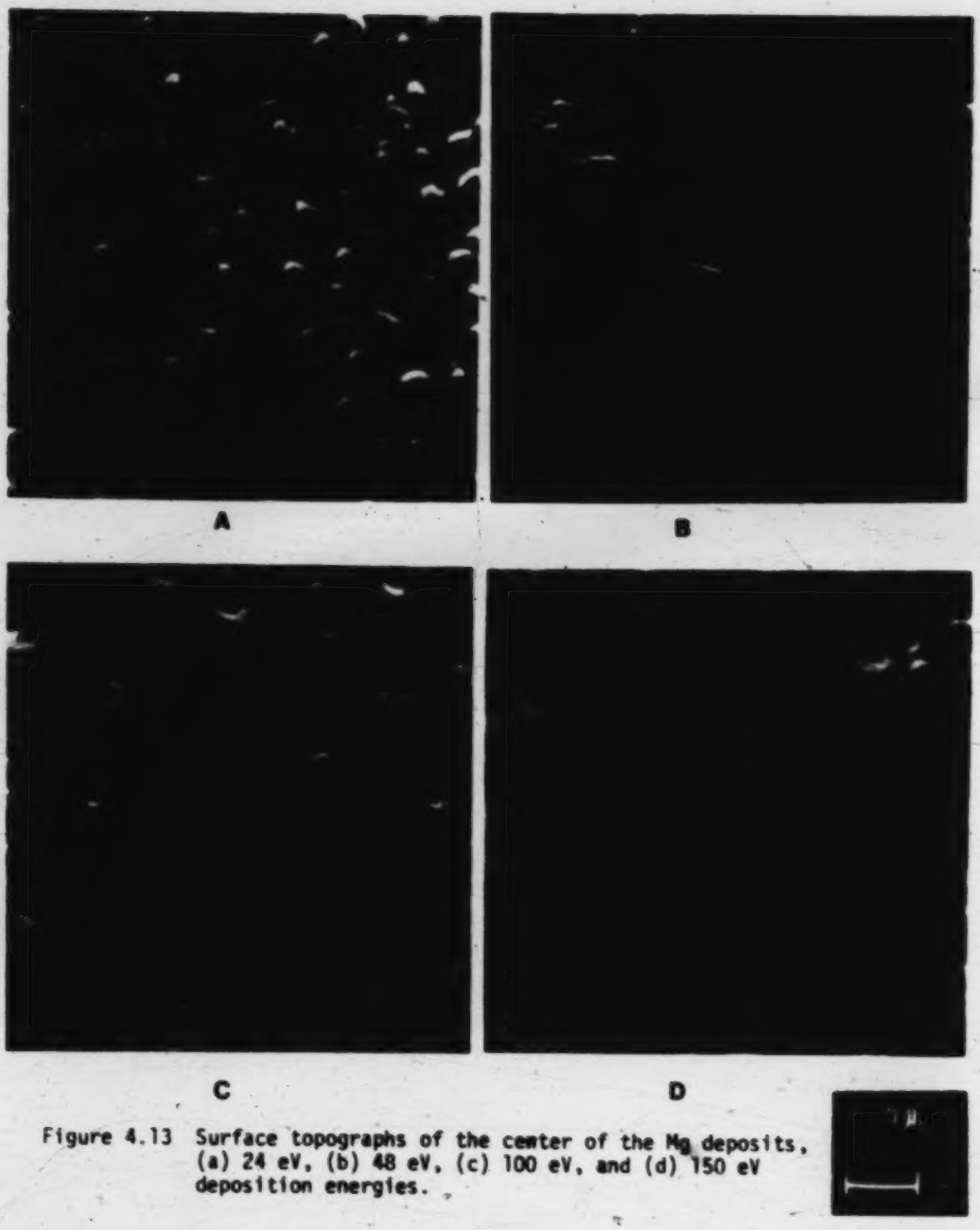

Figure 4.13 Surface topographs of the center of the Mg deposits, (a) 24 eV, (b) 48 eV, (c) 100 eV, and (d) 150 eV deposition energies.

with shallow craters. The deposit is continuous. At 100eV, deposit is still continuous, but deep craters and holes are clearly seen. The deposition at 150eV shows clear evidence of self-sputtering of deposits, with a surface topography resembling a lunar landscape with many sizes of shallow craters and holes.

Deposit Thickness Distribution

The effect of ion dosage on film growth can be approximated by investigating the deposit thickness distribution as mentioned previously in section 4.3.2.

The general features of the RBS spectra were the same as those of Pb deposits: more spreading at low energy deposition occurs because of the space-charge spreading.

Figure 4.14 shows scanning electron micrographs taken across the face of a 24eV deposit: (a) is from the deposit center, (b) is from 2mm off-center, and (c) is from 4 mm off-center. All surface topographies show the same corrugated surface structure with pebble-like protrusions. Only the spacing of protrusions vary with ion dosage. In the area of thicker deposits (higher ion dosage) the protrusions are further apart. The deposit obtained from 0.5 Coulomb total ion dosage had the same features, but protrusions were larger than that observed in a 0.25 Coulomb deposition.

Figure 4.15 shows the surface topographies of 100eV deposit taken from a) the deposition center, b) 2mm off-center and c) 4mm off-center. The surface topographies show completely different surface structures from those of 24eV. At higher ion dosage, a flat surface

A B

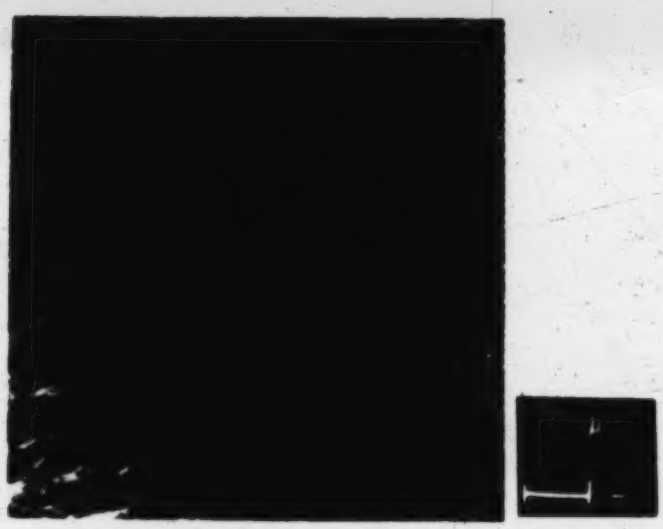

C

Figure 4.14 Surface topographs of 24 eV Mg deposit for various distance from deposition center, (a) deposition center, (b) 2 mm off-center, (c) 4 mm off-center.

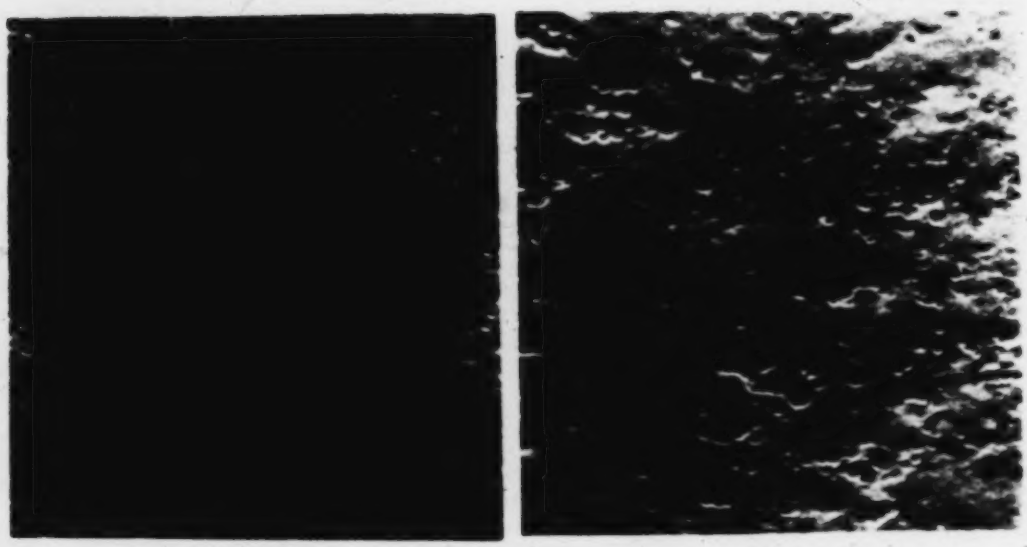

A B

C

Figure 4.15 Surface topographs of 100 eV Mg deposit for various distance from dedosition center, (a) deposition center, (b) 2 mm off-center,and (c) 4 mm off-center.

with few craters and holes is obtained. Decreasing ion dosage yields a wavy surface with many craters. At very low ion dosage, a very thin coating with a pitted surface is observed. This type of film growth was common for all other deposits except 24eV deposit.

From the above results, it can be concluded that the corrugated surface and surface growth was caused by 24eV incident ion energy rather than ion dosage variation, and that a relatively flat surface is obtained at deposition energy higher than 24eV.

4.4.3 X-ray Diffraction Analysis

When depositing an ion beam onto an insulator or highly resistive substrate, a thermal electron emission filament was required as described in section 3.2.3. The temperature of the whole substrate assembly, was about 100°C when the thermal filament was used for neutralization of surface charge build-ups.

Mg deposition onto a thin film carbon or single crystal NaCℓ was attempted by neutralizing the substrate surface with this thermal filament. However, no deposit or at most only very small area thin deposits at the center of the substrates were obtained due to the thermal re-evaporation of Mg deposits. Mg has a vapor pressure of 10^{-9} Torr at 150°C (Figure 1.1). The total pressure during deposition of the Mg ion beam was in the order of 10^{-8} Torr. The temperature of the substrate is probably higher than that of whole substrate assembly due to the filament-substrate configuration. Therefore, it is reasonable to speculate that Mg deposits were thermally re-evaporated by the substrate surface temperature of above 100°C.

In order to investigate the Mg film crystalline structure, the X-ray diffraction method was used. The diffraction pattern will include the film structure as well as the substrate structure because of deep penetration of X-ray.

Figure 4.16 shows the diffraction pattern of a) Poco Graphite substrate and b) a thick 100eV Mg deposit with the same substrate. The diffraction patterns obtained indicate the polycrystalline structure. There is no significant difference between a) and b). Because of the strong reflection spectrum from the substrate and the lack of adequate sensitivity of this analysis, the diffraction pattern from the Mg film cannot be distinguished from that of the substrate. Unequivocal information on the crystalline structure of the Mg deposits could not be obtained.

4.5 Conclusions

Pb^+ and Mg^+ ion beam depositions were successfully carried out by using the low energy ion beam deposition system.

Space-Charge Expansion and Self-Sputtering

The spreading of deposits due to the space-charge expansion of ion beams was found to be not a serious problem even for very low energy deposition. On the other hand, self-sputtering of deposits governs the deposit thickness, expecially for high sputtering yield materials such as Pb. This self-sputtering effect limits the range of possible deposition energies. For Pb, no deposits were observed at an energy of 200eV or higher. However, for low sputtering yield materials such

(A)

(B)

Figure 4.16 X-ray diffraction patterns of, (a) carbon substrate, (b) 100 eV Mg deposit on same substrate.

as Mg, the deposits were observed even for a 500eV deposition energy.

If only the space-charge expansion and self-sputtering is considered, the best deposition energy for Pb is about 50eV, and 100eV for Mg. These energies correspond to self-sputtering yields of about 0.1 to 0.2.

Adhesion

The adhesion of Pb deposits was strong even for 24eV deposition; on the other hand, only Mg deposits of 120eV or higher energy show strong adhesion to carbon substrates. Lower energy Mg deposits failed the "scotch-tape test." The strong adhesion of Pb deposits is speculated to be a result of surface damage of the substrate material and subsequent inter-mixing of deposits and substrate. The good adhesion of Mg deposits with higher energies is considered to be due to Mg particle penetration into the substrate surface.

Purity and Composition

The purity of Pb and Mg films has been shown within the sensitivity range of RBS analysis to be superior to that of films fabricated by conventional methods. However, the post-oxidization of Mg film was observed even for very carefully stored films.

The Pb films consist of several isotopes of Pb for all deposition energies. The lower energy deposited Mg films consists of several isotopes of Mg, but Mg films with higher energy deposition consist of only one isotope, i.e. Mg^{24}.

Thickness and Surface Structure

For the Pb films, the lowest energy (24eV) deposition yields the thickest films. However, there is evidence that film thickness increases without complete surface coverage at 24eV deposition. At 48eV deposition, the surface coverage is complete before the increase of film thickness. For a deposition energy of 120eV or higher, the surface coverage and film thickness decreases due to the self-sputtering of the deposits. The surface topography of 24eV deposits show thick film with gentle hilly-like features. At 48eV deposition, the surface of the deposit becomes flat and continuous with large grains, similar to that of recrystallized films. At 72eV deposition, the surface topography of the deposit shows a flat smooth film with big holes and channels. Both film thickness and complete surface coverage decreases as deposition energy is increased to approximately 100eV.

For Mg deposition, the film thicknesses are the same for 24eV, 48eV and 100eV deposition.

The micrograph of 24eV deposit shows a corrugated surface with pebble-like protrusions. The deposits of 48eV and 100eV have a flat surface with shallow craters.

As the deposition energy increases, surface topography shows the effect of self-sputtering and "lunar-surface" like features are obvious. Also, the RBS spectrum shows evidence of Mg particle penetration into the substrate at high energy deposition.

Film Growth

For both Pb and Mg deposition, the general tendency in film growth processes is towards an increase in area coverage rather than an increase in thickness. However, the degree of the surface coverage and thickness is dependent on the incident ion energy.

For Pb deposition, films with thicknesses more than 2500Å are required for total surface coverage for 24eV deposition. For 48eV and higher total coverage can be achieved by films less than 2000Å thickness.

For Mg deposition, a corrugated surface is obtained even for thick films at 24eV deposition, and good surface coverage was achieved with relatively thin films for energies up to 100eV. For 48eV and 100eV deposits, thin films with wavy surfaces are observed at low ion dosages. With an increase of ion dosage, thin flat films were obtained.

Crystalline Structure

The crystalline structure of the Pb deposits exhibits an incident ion energy dependence. For lower energy deposition, the deposit has an amorphous or polycrystalline structure. At a deposition energy of 120 eV, the deposit shows a definite orientation. When the substrate is a carbon thin film, a polycrystalline structure is obtained. For a single crystal NaCℓ substrate, the Pb deposit is almost an epitaxial film. A f.c.c. structure with [100] orientation is the dominant deposit crystal structure.

The investigation of crystalline structure of Mg film was conducted by X-ray diffraction. Because of a strong diffraction pattern due to the carbon graphite substrate, a detailed diffraction pattern from Mg films was not obtained.

Chapter 5

Limitation of Present System

The limitations of the present low energy ion beam deposition system can be divided into two categories: 1) limitations due to the nature of the deposition method, itself, and 2) limitations due to the system.

5.1 Limitations Due to the Nature of Deposition Method

Limitations which belong to this category are the self-sputtering effect and slow deposition rate.

The self-sputtering effect limits the range of the deposition energy for obtaining thick films. Especially for high sputtering yield materials such as Pb, Au and Ag, this is a serious problem when a thick film at a high energy of deposition is desirable. There is no absolute solution which overcomes this limitation, however the alternation of energy with a certain time interval might be one solution to minimize the self-sputtering effect. A thick film with strong adhesion and more orientated crystalline structure can be obtained by optimizing the deposition time interval for low and high incident particle energies.

Another limitation, the slow deposition rate, is also fundamental. Even if a mA range ion beam is employed, the deposition rate of the film is much lower than that of vacuum evaporation. There is no solution for this problem until an ion source which produces ampere range ion beams is available.

5.2 Limitations Due to the System

Limitations which belong to this category are ion species, ion current density, and substrate materials.

In the present ion source, only a limited number of ions of solid materials with sufficient ion current density have been obtained as mentioned in section 3.2.2 A. It has been rather difficult to obtain sufficient ion current density beams from high vaporization temperature materials such as Ag,Cu. The main difficulty arises from the condensation of vapor between the furnace and the ion source (see Figure 3-7). This problem may be solved by the combination of a furnace and an ion source into one unit. Figure 5-1 shows a schematic of the planned modified ion source. The main body of the ion source consists of Boron nitride or Alumina. Therefore, operational temperatures up to 2000°C are possible. The distance between the furnace and ion source is physically minimized to avoid vapor condensation. For low vaporization temperature materials, only the discharge filament may be required to obtain sufficient vapor pressure for discharge. The materials with vaporization temperatures up to approximately 1500°C can be used as charge materials by operating a furnace filament. Therefore the ion beams of practically every material except some refractory metals can probably be obtained by this ion source design (see Figure 1.1).

All depositions achieved in this research work were carried out by ion beams of up to tens of microamps. The increase of the total ion current and consequently the increase in deposition rate can be achieved by 1) the increase in extraction voltage, 2) increase in anode hole size and 3) adaptation of other ion sources.

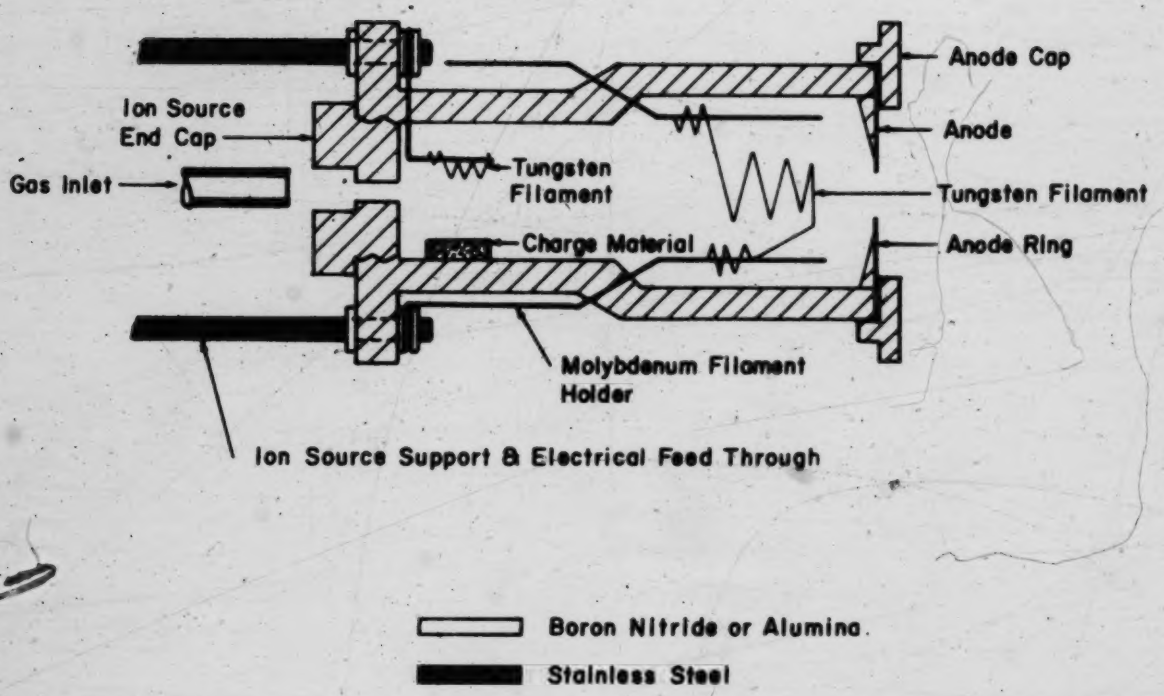

Figure 5.1 Plug-in ion source combined with furnace.

By combining 1) and 2), it might be possible to obtain an ion current in the mA range. But obviously higher pumping speed is required in the ion beam transportation chamber because of bigger conductance of an anode hole.

Other ion sources such as duoplasmatron and sputtering ion source can produce mA solid ion beams. However those ion sources have disadvantages, especially larger energy spread (10 to 50 eV) and higher cost per ion current as compared to the present low voltage arc discharge ion source [1].

The deceleration and deposition of high energy mA ion beams from an electromagnetic isotope separator is the other method used to obtain a high ion current beam deposition [2]. However, this method requires a precise deceleration system. The energy spread of the ion beam will be large, and the cost per ion beam will be high. Most important, the high cost ion implanter or electromagnetic isotope separator is not standard equipment in most laboratories.

When depositing ion beams onto an insulating surface, neutralization of the surface is required to avoid charge build-up. A thermal electron emission filament was used in the present system. However, for Mg deposition the temperature rise of the substrate, due to the thermal filament, induced the re-evaporation of deposits. This problem can be solved by 1) the inclusion of a low energy electron gun which provides sufficient electron beams to neutralize the substrate surface during deposition, and/or 2) cooling the sub-

strate by cooling water or liquid nitrogen circulation. Either 1) or 2) can be achieved by a slight modification of the substrate system.

5.3 Conclusions

The self-sputtering effect and slow deposition rate are ultimate limitations in the low energy ion beam deposition method. Limitations due to the system, itself, can be solved with modification to the ion source and to the substrate system.

The low energy ion beam deposition method and the present system are superior to the conventional deposition systems even with these limitations, if the resulting film characteristics such as purity, adhesion, etc. are of prime importance.

Chapter 6

Conclusions

This chapter summarizes the present study of low energy ion beam deposition of metallic thin films. First the system and the results of Pb and Mg deposition are described. The advantages of the low energy ion beam deposition method compared to the conventional deposition methods is then summarized.

6.1 Low Energy Ion Beam Deposition System

The system, which was designed and constructed, satisfies all required design criteria in order to produce homogeneous thin films with precise control of the deposition parameters.

The operational characteristics of the system are as follows:

Vacuum Condition: 10^{-7} to 10^{-8} Torr at the ion beam transportation chamber

10^{-8} to 10^{-9} Torr at the substrate chamber

Ion Species: Gas and solid ion beams

Ion Energy: +10eV to 4KeV

Ion Current: Up to 20μA

Ion source operational time: up to 100 hours with one charge

Mass Separation: $\frac{M}{\Delta M} \simeq 10$ at the substrate

Mass Selection: $1 \sim 600$ a.m.u.

Substrate: metal, semiconductor and insulator with various sizes and shapes

Deposition time: 4 hours to 7 hours for 0.25 Coulomb total ion dosage.

6.2 Pb^+ and Mg^+ Ion Beam Deposition

Deposition of Pb^+ and Mg^+ ion beams were successfully carried out by using the low energy ion beam deposition technique.

The main interest of this research work was the investigation of the relationships between the incident particle energies and consequent film characteristics. If only space-charge expansion and self-sputtering are considered, the optimum deposition energy in terms of deposition time for Pb is about 50 eV and 100 eV for Mg.

For adhesion, all energies used were found to be satisfactory for Pb but only energies of 120 eV or higher resulted in good adhesion of Mg films.

For film thickness and surface coverage, the best deposition energy is about 50 eV for Pb. For Mg films, the energy range between 50 eV and 100 eV is the most desirable.

For film crystalline structure, higher energy deposition yielded a more orientated crystalline structure for Pb deposits.

A significant effect of variations of ion dose rate was not observed in this research work.

6.3 Advantages of the Low Energy Ion Beam Deposition System

The most important advantage of this deposition system is the precise controllability of deposition parameters. To the author's knowledge, this deposition system is presently the best method avail-

able for investigating variation of characteristics due to changes in deposition parameters. Consequently, this deposition system allows precise control of the film characteristics for specific applications.

The deposits obtained by the present system also show superior film characteristics as compared to that of conventional deposition systems. The main characteristics are as follows:

1) strong adhesion for higher energy deposition,
2) good surface coverage, no shadowing effect,
3) pure homogenous films,
4) oriented crystalline structured films deposited at higher deposition energies.

References

CHAPTER 1

[1] See Appendix 1

[2] L. Holland, Vacuum Deposition of Thin Films, (John Wiley and Sons, N.Y., 1958).

[3] K.L. Chopra, Thin Film Phenomena, (McGraw-Hill N.Y., 1969).

[4] L.I. Maissel and R. Glang, Handbook of Thin Film Technology, (McGraw-Hill, N.Y., 1970).

[5] D.M. Mattox,"Sputtering Deposition and Ion Plating Technology," A.V.S. Thin Film Division Report, (1973).

[6] J.N. Coburn, E.W. Eckstein and E. Kay., "A Mass Spectrometric Study of Neutral-Sputtered Species in an RF Glow Discharge Sputtering System," J. Vac. Sci. Technol., 12, 151, (1975).

[7] E. Kay, "Analysis of Gas Incorporation in Thin Films," J. Vac. Sci. Technol., 7, 317, (1970).

[8] D.V. Morgan and R.P. Gittins, "An Investigation of the Stoichiometry and Impurity Content of Thin Silicon Oxide Films Using Rutherford Scattering of MeV α-Particles," Phys. Stat. Sol. A13, 517, (1972).

[9] H.L. Caswell, "Ultra-High Vacuum Evaporators and Residual Gas Analysis," in Physics of Thin Films, Vol. 1, ed. G. Hass, (Academic Press, N.Y. 1963).

[10] J.S. Colligon, W.A. Grant, J.S. Williams and R.P.W. Lawson, "Deposition of Thin Films by Retardation of an Isotope Separator Beam," Proc. of the International Conference on the Application of Ion Beams to Metals, University of Warwick, September (1975).

[11] A.R. Wolter, "Ion Beam Deposition of Metal Films," Proc. of 4th Microelectronics Symposium, St. Louis Section of IEEE, 2A-1, (1965).

[12] A.R. Wolter, "Metallic Ion Deposition," in Proc. of 2nd International Conference on Electron and Ion Beam Science and Technology, ed., R. Bakish, (American Institute of Mining, Metallurgical and Petroleum Engineers, N.Y., 1969).

[13] B.A. Probyn, "A Low-Energy Ion Source for the Deposition of Chromium," J. Phys. D., 1, 457 (1968).

[14] R.E. Honig and D.A. Kramer, R.C.A. Review 30, 285, (1969).

[15] Loc. cit. [2] Chapter 1 "Vacuum Evaporation."

[16] R. Glang, "Vacuum Evaporation," Loc. cit. [4], Chapter 1.

[17] L.I. Maissel, "Application of Sputtering to the Deposition of Films," Loc. cit. [4], Chapter 4.

[18] L.I. Maissel, "The Deposition of Thin Films by Cathode Sputtering," in Physics of Thin Films, Vol. 3, eds., G. Hass and R.F. Thun, (Academic Press, N.Y. 1966).

[19] W. Laznovsky, "Advances in Low Energy Ion Beam Technology," Research/Development, 26, 47 (1975).

[20] P.H. Schmidt, R.N. Castellano and E.G. Spencer, "Deposition and Evaluation of Thin Films by DC Ion Beam Sputtering," Solid State Technol. 15, 27 (1972).

[21] D.M. Mattox, "Fundamentals of Ion Plating," J. Vac. Sci. Technol. 10, 47 (1973).

[22] D.L. Chambers and D.C. Carmichael, "Electron Beam Techniques for Ion Plating," Research/Development, 32 (May, 1971).

[23] Y. Enomota and K. Matsubara, "Structure and Mechanical Properties of Ion-plated Thick Films," J. Vac. Sci. Technol. 12, 827 (1975).

[24] J. Chin and N.B. Elsner, "Preparation of Si_3N_4 Coatings by Ion Plating," J. Vac. Sci. Technol. 12, 821 (1975).

[25] P. Glaser, A.R. Herman and G. Vago, "Ion Evaporation," Thin Solid Films, 32, 69 (1976).

[26] T. Takagi, I. Yamada and A. Sasaki, "Ionized-cluster Beam Deposition," J. Vac. Sci. Technol., 12, 1128 (1975).

[27] Y. Murayama, "Thin Film Formation of In_2O_3, TiN and TaN by RF Reactive Ion Plating," J. Vac. Sci. Technol., 12, 818 (1975).

[28] Y. Murayama, "Structure of Ga As and GaP Thin Films Formed by RF Ion-Beam Epitaxy," J. Vac. Sci. Technol., 12, 876 (1975).

[29] S. Aisenberg and R.W. Chabot, "Physics of Ion Plating and Ion Beam Deposition," J. Vac. Sci. Technol., 10, 104 (1973).

[30] S. Aisenberg and R.W. Chabot, "Ion-Beam Deposition of Thin Films of Diamond -like Carbon," J. App. Phys. 42, 2953 (1971).

CHAPTER 2

[1] G. Carter and J.S. Colligon, Ion Bombardment of Solids, (Heineman, London, 1969).

[2] M. Kaminsky, Atomic and Ionic Impact Phenomena on Metal Surfaces, (Springer, Berlin, 1965).

[3] M.W. Thompson, Defects and Radiation Damage in Metals, (Cambridge University Press, Cambridge, 1969).

[4] R.S. Nelson, The Observation of Atomic Collisions in Crystalline Solids, (North-Holland, Amsterdam, 1968).

[5] L.T. Chadderton, Radiation Damage in Crystals (Methuen, London, 1965).

[6] G. Dearnaley, "Ion Bombardment and Implantation," in Reports on Progress in Physics, Vol. 32, 405, (Academic Press, New York, 1969).

[7] P.A. Redhead, J.P. Hobson and E.V. Kornelsen, The Physical Basis of Ultra-High Vacuum, (Chapman and Hall, London, 1968).

[8] Loc. cit. [2], Chapter 12, "Neutralization of Ions on Metal Surfaces," p. 263.

[9] H.D. Hagstrum, "Auger Ejection of Electrons from Tungsten by Noble Gas Ions," Phys. Rev. 104, 317 (1956).

[10] H.D. Hagstrum, "Auger Ejection of Electrons from Molybdenum by Noble Gas Ions," Phys. Rev. 104, 672, (1956).

[11] Loc. cit. [1], Chapter 7, "Sputtering," p. 310.

[12] Loc. cit. [2], Chapter 10, "Sputtering of Metal Surfaces by Ion Bombardment," p. 142.

[13] O.E. Almén and G. Bruce, "Sputtering Experiments in the High Energy Region," Nucl. Instr. Meth., 11, 279 (1961).

[14] W.H. Hayward and A.R. Wolter, "Sputtering Yield Measurements with Low-Energy Metal Ion Beams," J. Appl. Phys, 40, 2911 (1969).

[15] Loc. cit. [1] Chapter 7, "The Penetration of Ions."

[16] E.V. Kornelsen, R. Brown, J.A. Davies, B. Domeij and G.R. Piercy, "Penetration of Heavy Ions of KeV Energies into Monocrystalline Tungsten," Phys. Rev. 136A, 849 (1964).

[17] J.A. Venables, "Low Energy Ion Bombardment of Solids," in Atomic Collision Phenomena in Solids, eds., D.W. Palmer, M.W. Thompson, P.D. Townsend, 132 (North-Holland, Amsterdam, 1970).

[18] Loc. cit. [1], Chapter 2, "Collision Between Atoms," p. 13.

[19] Loc. cit. [5], Chapter 6, "The Atomic Interaction Potential, p. 914.

[20] A.A. Abrahamson, "Born-Mayer Type Interatomic Potential for Neutral Ground-State Atom with Z=2, to z=105," Phys. Rev. 178, 76 (1969).

[21] G. Carter, "Ion Reflection, Penetration, and Entrapment in Solids," J. Vac. Sci. and Technol., 7, 31 (1970).

[22] H.H. Andersen and P. Sigmund, "A Simple Nonobinary Scattering Model Applicable to Atomic Collisions in Crystals at Low Energies," Mat.-fys. Medd, 34, No. 15 (1966).

[23] C. Kittel, Intro to Solid State Physics, 4th ed. Chapter 5, (John Wiley and Son, N.Y., 1971).

CHAPTER 3

[1] G. Lewin, Fundamentals of Vacuum Science and Technology, Chapter 3, "Surface Effects," p. 23, (McGraw-Hill, New York, 1965).

[2] C.M. Van Atta, Vacuum Science and Engineering, Chapter 1, "The Nature and Behavior of Gases," (McGraw-Hill, New York, 1965).

[3] R.G. Wilson and G.R. Brewer, Ion Beams with Application to Ion Implantation," Chapter 2, "Ionization Phenomena and Ion Sources," p. 11, (John Wiley and Sons, New York, 1973).

[4] R. Hatter, "Beam with Space-Charge," in Focusing of Charged Particles, Vol. II, ed. A. Septier, Chapter 3.1, p. 3, (Academic Press, New York, 1967).

[5] S.L. Hollway, "The Optimum Space-Charge-Controlled Focus of an Electron Beam," Aust. J. of Sci. Res. A5, 430 (1952).

[6] Loc. cit. [3] Chapter 3, "Ion-Beam Formation and Transport,"

[7] Colutron Ion Source Manual, Colutron Corporation, Boulder, Colorado.

[8] Loc. cit. [2] Chapter 2, "Gas Flow."

[9] D.P. Smith, "Analysis of Surface Composition with Low-Energy Backscattered Ions," Surface Sci., 25, 171 (1971).

[10] H.W. Werner, "Theoretical and Experimental Aspects of Secondary Ion Mass Spectrometry," Vacuum 24, 493 (1974).

[11] J.S. Colligon, "Surface Compositional Analysis Using Low Energy Ion Bombardment Induced Emission Processes," Vacuum, 24, 373 (1974)

[12] L. Wahlin, "The Colutron Mark II, A Velocity Filter Isotope Separator," Nucl. Instr. Meth. 38, 133 (1965).

[13] L. Wahlin, "The Colutron, A Zero Deflection Isotope Separator," Nucl. Inst. Metho. 27, 55 (1964).

[14] M. Menzinger and L. Wahlin, "High Intensity, Low Energy Spread Ion Source for Chemical Accelerators," Rev. Sci. Inst. 40, 102 (1969).

[15] L. Wahlin and F. Chernow, "The University Colorado Ion Implanter," Record of 10th Symposium on Electron, Ion and Laser Beam Technology, ed., L. Marton, 189, (San Fransisco Press, SFO, 1969).

[16] S.C. Brown, Basic Data of Plasma Physics,(John Wiley and Sons, New York, 1959).

[17] H.C. Madan, "Thin Film Deposition by Ion Beams," M.Eng. Report, University of Alberta (1973).

[18] K.J. Hanszen and R. Lauer, "Electrostatic Lenses," Loc. cit. [4], Vol. I, Chapter 2.2, p. 251.

[19] B. Elbek, M.C. Olesen and O. Skilbreid, "Inelastic Scattering From Separated Lutecium Isotopes," Nuclear Physics 10, 294 (1959).

[20] I. Bergström, F.Brown, J.A. Davies, J.S. Gieger, R.L. Graham and R. Kelly, "On the Electromagnetic Separator Method of Preparing Radioactive Sources for Precision β-spectroscopy," Nucl. Inst. Methods, 12, 249 (1963).

[21] J.A. Simpson, "Design of Retarding Field Energy Analyzers," Rev. of Sci. Inst. 32, 1283 (1961).

[22] M.M. MacNaughton, "The Focal Properties and Spherical Aberration Constants of Aperture Electron Lenses," Proc. Phys. Soc. (London), B65, 590 (1952).

[23] A.R. Wolter, "Ion-Beam Deposition of Metal Films," Proc. 4th Microelectronics Symp. St. Louis Section of IEEE, 2A-1 (1965).

[24] Poco Graphite Catalog, Poco Graphite Inc. Texas.

[25] P.J. Goodhew, "Specimen Preparation in Material Science," in Practical Methods in Electron Microscopy, Vol. 1, ed., A.M. Glauert, (North-Holland, Amsterdam, 1972).

[26] D.E. Bradley, "Replica and Shadowing Techniques," in Techniques for Electron Microscopy, ed., D. Kay, (Blackwell Scientific, Oxford, 1967).

CHAPTER 4

[1] M.A. Nicolet, J.W. Mayer, and I.V. Mitchell, "Micro-analysis of Materials by Backscattering Spectrometry," Science 177, 841 (1972).

[2] W.K. Chu, J.W. Mayer, M.A. Nicolet, T.M. Buck, G. Amsel and F. Eisen, "Principles and Application of Ion Beam Techniques for the Analysis of Solids and Thin Films," Thin Solid Films 17, 1 (1973).

[3] S.T. Picraux, E.P. EerNisse and F.L. Vook, eds., Applications of Ion Beams to Metals, (Plenum Press, N.Y. 1974).

[4] W.K. Chu, J.W. Mayer, M.A. Nicolet, S.V. Campisano and E. Kimini, "Backscattering Analysis," in Handbook on Ion Beam Analysis (will be published)

[5] J.R. Cameron, "Elastic Scattering of Alpha-particles by Oxygen," Phys. Rev. 90, 839 (1953).

[6] R.W. Hill, "Elastic Scattering of Alpha-particles by Carbon," Phys. Rev. 90, 845 (1953).

[7] Ortec Quality Assurance Data, Oak Ridge, Tenn.

[8] R.E. Thun, "Structure of Thin Filmsy in Physics of Thin Films, Vol. 1, ed., G. Hass, 187 (Academic Press, N.Y. 1963).

[9] P.B. Hirsch, .A. Howie, R.B. Nicholson, D.W. Pashley and M.J. Whelan, Electron Microscopy of Thin Crystals, (Butterworths, London, 1965).

[10] B.E.P. Beeston, "An Introduction to Electron Diffraction," in Practical Methods in Electron Microscopy, Vol. 1, ed., A.M. Glauert, 213 (North-Holland, Amsterdam, 1972).

[11] L.V. Azaroff, Elements of X-Ray Crystallography, 346, (McGraw-Hill, N.Y. 1968).

[12] B.D. Cullity, Elements of X-Ray Diffraction, 163 (Addison-Wesley, N.Y. 1956).

[13] J.I. Goldstein and H. Yakiwitz, eds., Practical Scanning Electron Microscopy, (Plenum, N.Y. 1975).

[14] O.C. Wells, Scanning Electron Microscopy, (McGraw-Hill, N.Y. 1974).

[15] G.K. Wehner, "Low Energy Sputtering Studies," in Ion Bombardment; Theory and Applications, ed., J.J. Trillat, 261, (Gordon and Breach, N.Y. 1964).

[16] J.S. Colligon and R.N. Bramban, "Low Energy Sputtering of Gold," in Atomic Collision Phenomena in Solids, eds., D.W. Palmer, M.W. Thompson and P.D. Townsend, 258 (North-Holland, Amsterdam, 1970).

[17] D.S. Campbell, "Mechanical Properties of Thin Films," in Handbook of Thin Film Technology, Chapter 12.

[18] D.V. Morgan and R.P. Gittins, "An Investigation of the Stoichiometry and Impurity Content of Thin Silicon Oxide Films Using Rutherford Backscattering of MeV α-particles," Phys. Stat. Sol. (a)13, 517 (1972).

[19] L.C. Northcliffe and R.F. Schilling, "Range and Stopping-Power Table for Heavy Ions," Nuclear Data Tables, A7, 233 (1970).

[20] O. Meyer, H. Mann and G. Linker, "Observation of Film Growth Process by Means of Backscattering Techniques," Appl. Phys. Lett., 20, 259 (1972).

[21] J.V. Sanders, "Structure of Evaporated Metal Films," in Chemisorption and Reactions on Metal Films, ed., J.R. Anderson, Chapter 1, (Academic Press, London 1971).

[22] Loc. cit. [10], Chapter 4, "Analysis of the Electron Diffraction Pattern," p. 223.

[23] J.D.H. Donnary and G. Donnary, eds., Crystal Data Determinative Tables, (American Crystallographic Association, Washington, D.C. 1963).

[24] I.M. Ritchie, "The Oxidation of Evaporated Metal Films," Loc. cit. [20], Vol. 2, Chapter 10, 257.

[25] W.B. Pearson, A Handbook of Lattice Spacings and Structures of Metals and Alloys, Vol. 2, (Pergamon, London, 1967).

CHAPTER 5

[1] R.G. Wilson and G.R. Brewer, Ion Beams with Application to Ion Implantation, Chapter 2, 11 (John Wiley and Sons, N.Y. 1973).

[2] J.H. Freeman, W. Temple, D. Beanland and G.A. Gard, "Ion Beam Studies - Pt. I: The Retardation of Ion Beams to Very Low Energies in an Implantation Accelerator," AERE Report 8287 (February 1976).

Appendix

High Power Laser Optical Materials and Their Damage Thresholds.

1. Introduction

2. High Power IR Laser Window Materials.

   2.1 Single Crystal Alkali-halide Window Materials.

   2.2 Single Crystal II - VI, III - V and IV Semiconductor Window Materials.

   2.3 Chalcogenide Glass IR-window Materials.

   2.4 Polycrystalline IR Window Materials.

3. Damage Thresholds for High Power IR Laser Windows.

4. High Power IR Laser Mirror Materials.

5. Damage Threshold for High Power IR Mirrors.

6. Conclusion.

Bibliography

References

1. Introduction

In the development of high power lasers, especially infrared (IR) lasers, the damage of optical material is the fundamental limitation of high power CW or pulsed laser performance. Raising the damage thresholds of optical materials, primarily windows and mirrors, increase the system reliability and efficiency.

At present alkali-halides and semiconductors are the most suitable materials for high power IR laser window applications. For high power IR laser mirror applications, carefully polished and coated copper or molybdenum exhibits the highest damage thresholds. The individual materials will be considered in detail in the following chapters.

At this point, the laser-induced damage mechanism has not been completely understood. The ultimate or intrinsic strength is related to a thermal and /or an avalanche processes[1,2]. However, in many situations, optical materials exhibit lower damage thresholds than the intrinsic strength because of various extrinsic influences[3,4]. Two major extrinsic factors have been identified: field enhancement caused by mechanical imperfections such as pits and scratches[5-9], and impurities being absorbed on the surface[10-14]. Only surfaces free of defects and impurities can achieve the same intrinsic damage level as impurity free bulk materials.

2. High Power IR Laser Window Materials.

The development of pulsed and CW high power IR lasers required nearly lossless reflection from mirrors and nearly reflectionless and lossless transmission through windows. Moreover, for high power

IR laser windows, optical distortion of the laser beam during operation usually becomes unacceptable well before the mechanical failure of windows.

The significance of a large number of mechanical and optical properties for high power IR laser window materials has been discussed by Sparks[14-17], Bendow[18-21] and others[22,23]. For a complete characterization of high power IR laser window materials, the following data should be obtained:

1. optical spectrum, including the determination of the band gap and optical phonon carrier,
2. index of refraction n and its temperature coefficient dn/dT, both in the wavelength region around 10.6μm,
3. residual optical absorption coefficient β in transparent regions,
4. light scattering characteristics and large-scale optical homogeneity,
5. density, specific heat and melting point,
6. thermal conductivity and thermal expansion,
7. hardness and resistance to abrasion and moisture,
8. yield and fracture strength,
9. elastic moduli and photo-elastic constants,
10. electric dc conductivity,
11. resistance to radiation-induced optical damage.

From the guideline given by Sparks and others, few types of materials transmit well enough at 10.6μm to be used as high power IR

laser windows. Namely, single crystal alkali-halides, single crystal II-VI, III-V and VI semiconductors, chalcogenide glass and polycrystalline materials. Table 1 shows the advantages and disadvantages of materials for use at 10.6μm[24]. Table 2[15] shows the minimum window thickness under pressure p = 7.3 psi and Table 3[15] shows the useful figure of merit for pulsed mode in 10 cm diameter windows for possible high power IR laser window materials. From these theoretical and experimental results, the most promising materials for high power IR laser windows are found among the alkali-halides (KCℓ, NaCℓ) and semiconductors) ZnSe, CdTe, GaAs). Also, high power IR laser window materials will need anti-reflection (AR) coatings. In addition to AR coatings, several of the promising materials will need protective coatings against the deleterious effects of the atmosphere, especially of water vapor.

There are numerous other engineering problems in the window design besides the development of suitable window materials. Mechanical details of mounting; the manner of cooling the window surfaces and rims; the protection of the optical windows during periods when no laser beam is transmitted; the question of segmenting the window area; aerodynamic loading; the maintenance of a controlled-temperature profile; the single pulse, pulse train, of the quasi-continuous mode of power transmission. These are all important aspects of the high power IR laser window problems.

2.1 Single Crystal Alkali-Halide Window Materials.

The main advantages of alkali-halides are their low intrinsic absorption and their availability in sufficiently pure and large sizes. The main disadvantage of the pure ionic single crystal materials lie in their mechanical properties. In addition, some material candidates

Table 1

Advantages and disadvantages of materials for use at 10.6μm

materials	low expected absorption coefficient	low measured absorption coefficient	low optical distortion	great mechanical strength	low water absorption	large ΔT_o	thermal conductivity	available in large size	small required thickness	high power coating available
Ge	F	P	F	G	G	P	G	F	G	P
GaAs	F	F	F	G	G	P	G	P	G	P
ZnSe	G	F	F	G	G	F	F	P	F	P
CdTe	G	F	F	F	G	P	P	P	F	P
KBr	G	F	G	F*	P	G	P	G	F*	P
KCl	G	G	G	F*	P	G	P	G	F*	P
Tl(Br,I)	U	F	F	F	G	F	P	G	F*	P
$Ge_{28}Sb_1Se_{60}$ glass	F	P	F	G	G	P	P	G	G	P
As_2Se_3 glass	F	P	F	G	G	P	P	G	G	P

G: Good

F: Fair

P: Poor

U: Unknown

* doped materials

Table 2

Minimum Window Thickness

Material	Fracture $10^{-2}\ell_f/D$	Pressure-induced optical distortion $10^{-2}\ell_o/D$ D = 1 cm	D = 10 cm	D = 100 cm
ZnSe	3.00	1.23	1.96	3.10
CdTe	8.03	1.66	2.63	4.17
GaAs	1.65	1.26	2.00	3.18
Ge	2.01	1.24	1.96	3.10
KCℓ	12.9	1.40	2.21	3.51
KBr	18.5	1.49	2.36	3.74
NaCℓ	12.5	1.25	1.99	3.15
KRS-5(TlBr-TlI)	3.80	2.23	3.53	5.60
$Ge_{28}Sb_{12}Se_{60}$glass	4.27	1.84	2.92	4.63

Table 3

Figures of merit for pulse mode in 10 cm diameter windows

Material	Measured values of β in cm^{-1}	Thermally induced optical distortion: Thermal fracture I_t kW/cm^2	Limited by pressure fracture I_f kW/cm^2	limited by pressure distortion I_o kW/cm^2	For one cm. I_{1cm} kW/cm^2
ZnSe	$5x10^{-3}$	20.4	3.76	5.76	1.13
KCℓ	$4.8x10^{-4}$	3.02	37.8	220.	48.8
CdTe	$1.5x10^{-3}$	14.6	1.07	3.25	0.859
NaCℓ	$1.3x10^{-3}$	0.971	23.1	145.	29.0
GaAs	$5x10^{-3}$	40.5	1.15	0.949	0.190
KRS-5	$5x10^{-3}$	3.62	0.377	0.406	0.143
$Ge_{28}Sb_{12}Se_{60}$	0.02	1.56	0.171	0.251	0.073
Ge	0.025	4.9	0.149	0.154	0.030
KBr	$4x10^{-3}$	0.144	3.75	29.6	6.98

for use at 10.6 m are hygroscopic and need a protective coating against atmospheric attack. Yong[25] had shown that NaCℓ, tightly sealed with a vitreous coat of As_2S_3, can be remarkably stable. This is a convenient match for small windows as the thermal expansion coefficient for As_2S_3 ($25 \times 10^{-6}/°C$) is just a little less than that for NaCℓ ($31 \times 10^{-6}/°C$). These vitreous coatings also serve as a protective against color center formation by UV radiation and may serve as the high index component of an AR coating (BaF_2 is commonly used as the low index component).

In order to overcome poor mechanical properties of these ionic crystals, several methods of strengthening these methods include: a mixture of cations or anions, solid solution formation, use of systems with solid-solid immiscibility, and polycrystalline formation. The crystals are strengthened by about an order of magnitude by the addition of certain ions with an unknown effect on the absorptivity.[26]

The most promising material for a window at 10.6 μm appears to be a single crystal KCℓ strengthened with addition of Sr, orientated in certain crystal directions normal to the window face and completely coated with $\lambda/4$ films of As_2S_3 or As_2Se_3. Possible alternatives are the systems KBr:Sr and NaCℓ:Ca, similarly orientated and coated.

2.2 Single Crystal II-VI, III-V and IV Semiconductor Window Materials.

The main disadvantages of these types of semiconductors are their narrow band gaps which make them susceptible to thermal runaway or avalanche impact ionization at low levels of laser radiation. In order to keep the free carrier absorption low at room temperature, energy gap should be very roughly greater than 0.7eV. The value of energy gap tends to increase as the masses of the elements in the crystal decrease

and as the amount of ionic bonding increases. The mechanical and chemical properties of materials (strength, hardness, hygroscopicity, etc.) tend to be better for crystals containing light masses and for those with small amounts of ionic bonding. The masses of the elements in the crystal must not be too light or the lattice absorption will be too large. They also must not be too heavy or the free carrier absorption will be too large and they will have poor physical and thermal properties. This relationship is shown in Table 4.

From this point of view, the most promising semiconductor materials for high power IR laser windows are CdTe, ZnSe, GaAs and Ge. These materials also show the good figure of merit (refer to Table 3).

Table 4

Summary of trends of material properties

materials containing light masses	ionic bounded materials
high lattice absorption.	low lattice absorption.
low free-carrier absorption	low free-carrier absorption.
good mechanical, chemical and thermal properties.	poor mechanical, chemical and thermal properties.

One of the greatest disadvantages of most II-VI, III-V and VI semiconductor materials is that they are not available as large single crystals. Also AR coatings are especially important for semiconductor materials, because the large value of their refractive index gives rise to large reflection losses[28,29].

One of the exceptional semiconductor materials for high power IR laser windows is diamond which has good physical, chemical and

thermal properties. Douglas-Hamilton and Hoag[30] showed the superior properties of diamond for high power IR laser window application. Table 5 illustrates the properties of diamond. The main disadvantages of diamond are the difficulty to obtain sufficient size, and its prohibitive price. This prevents the further applications of diamonds for high power IR laser windows.

2.3 Chalcogenid Glass IR Window Materials.

In addition to the absorption at 10.6μm due to oxide impurities[31], homogenous chalcogenide glasses posses a number of inherent drawbacks as high power IR laser windows, especially: low strength, low thermal conductivities, and high coefficients of thermal expansion.

Table 5

Physical and Optical Properties of Diamond

Refractive Index (8-13μ)	2.41	Hardness(Knoop 50 gm)	9800
Transmission (8-13μ)	>70%	Density (gm/cc)	3.5
Absorption @ 10.6μ	10^{-3}/mm	Flexural Strength(psi)	700,000
Thermal Expansion ($x10^{-6}$/°C)	1.05	Young's Modulus(psi$x10^{6}$)	100
Thermal Conductivity(cgs)	22.8W	Electrical Resistivity(ohm-cm)	$>10^{15}\Omega$
Specific Heat (C:J/cm^3°K)	1.56		

Although chalcogenide glasses have a number of disadvantages, they should remain candidates for both bulk and coatings for high power IR laser windows, because of the ease of fabrication of large sizes and the lack of reactivity with atmosphere.

2.4 Polycrystalline IR Window Materials.

In general, the fine grain sized polycrystalline materials have much better tensile strength. Single crystals of the materials potentially useful as high power IR laser windows can be significantly weaker than fine grain polycrystalline counterparts because of dislocation blocking. The difference in strength may be an order of magnitude between the two. The successful production of strengthened polycrystalline KCℓ (in excess of 9000 psi) by grain size control has been reported [33].

However, for a given compound in polycrystalline form as compared to single crystal form, absorption is expected to be greater for polycrystalline form, other properties being equal. The main reasons for this effect are: the free-carrier problem at grain boundaries and increased impurity concentration.[33]

3. Damage Thresholds for High Power IR Laser Windows.

At the 1973 Damage Symposium, a few reports on damage measurements of high power IR windows were published for the first time. To evaluate the damage thresholds of windows in terms of a few basic physical principles is very difficult, because of the multitude of laser characteristics and the multitude of component structures used. Lasers operated at CW, pulsed and various repetition rates produced different effects in amorphous, polycrystalline and single crystal materials depending upon the presence or absence of coatings on surface of different microscopic structures. For defect and impurity free surfaces, damage thresholds, in terms of the amplitude of the electric field, were identical to bulk values. This intrinsic strength was achieved under pulsed conditions regardless of crystalline

orientation. However, when these same materials were subjected to high power CW loading, definite orientation effects were noted.

For either pulsed or CW irradiation, alloys or mixtures of two materials tend to damage at a level for the two individual components. Essentially, in all cases coatings reduces damage resistance compared to the bare surfaces.

Hughes Research Laboratories reported detailed results on three prime candidate high power 10.6μm laser window materials, namely KCℓ, ZnSe and CdTe. Their results are shown in Table 6[34]. Laser used in their experiments is uv-preionized TEA laser, operating TEM00 and emitting pulses of 600 nsec duration. Their primary conclusions are:

1. the damages occurred primarily at the surface for KCℓ and CdTe, but in the bulk for ZnSe,
2. the failure within ZnSe was initiated at voids surrounded by Zn, or a Zn rich ZnSe region,
3. damage thresholds were generally lower for coated windows than for uncoated windows,
4. KCℓ exhibited the highest damage thresholds while CdTe did the lowest.

Davit[35] reported on damage to Ge, KCℓ amd NaCℓ from TEM00, 75n-sec pulsed CO_2 laser. He noted that in these materials damage always occurs at the surface, and may or may not be accompanied by a plasma. In addition, he observed plasma formation without damage. If this is the case one may be able to clean surfaces by slowly raising the laser radiation levels and thus remove deleterious particles. Single shot damage on Ge surface occurred at 13 J/cm^2, while 100 irradiations at 7.5 J/cm^2 produced no visible damage.

Similar results were obtained when employing good AR coatings. For the alkali-halides he observed a general dissipation of plasma breakdown over the first 50 exposures at 7.5 J/cm^2. For these same materials he observed no difference in damage levels between the <111> and <100> crystal faces.

Posen, et. al. investigated the interaction of an intense CW 10.6μm CO_2 laser with single crystals of KCℓ, KBr and alloy ALQLOY ($KC\ell_{0.33}$-$KBr_{0.67}$) as a function of crystal orientation. They found a definite relationship between crystal orientations, and damage levels. Their results are shown in Table 7[36]. This difference is due to the relatively long term thermal interaction in the CW case as opposed to the transient processes in the case of pulsed damage. The controlling failure mechanism with coated windows is probably the initiation of plastic deformation in the weaker elements of either the coatings or the substrates.

4. High Power IR Laser Mirror Materials.

The basic requirements for high power IR laser mirrors are: high reflectivity, high damage thresholds and good thermal and mechanical properties.

Table 6

Damage Thresholds of KCℓ, ZnSe and CdTe

Substrate	coatings	bulk absorption /cm	coating absorption %/surface	damage thresholds J/cm^2
KCℓ	none	0.0007	-	>75
	As_2S_3/ThF_4	0.00096	0.19	31
	ThF_4/As_2S_3	0.0015	0.80	10-6
ZnSe	none	0.02	-	5.6
	none	0.009	-	41
	BaF_2/ZnS	0.0041	0.27	27
CdTe	none	0.0034	-	2.6
	CdTe	-	~2	1.2

Table 7

Damage thresholds of KCℓ, KBr and ALQLOY

Substrate	orientation	coatings	damage thresholds KW/cm^2
KCℓ	<110>	none	>38
	<111>	none	>38
	<100>	none	>38
	<110>	12μGe	14.5
	<111>	12μGe	14.6
	<100>	12μGe	5.1
KBr	<100>	none	>38
ALQLOY	<110>	none	>38
	<111>	none	>38
	<100>	none	28.5

At this point the candidate substrate materials for high power IR mirrors are established and damage experiments have been carried out. Presently the main problem is the substrate finish of the substrate materials and suitable coating materials and methods.

The high reflectivity can potentially be produced in a number of different ways. The super-polished[37] or diamond machined[38] metal surfaces achieve 98% reflectivity. The vacuum evaporated or sputtered films of a number of different metals can achieve higher reflectivity[39-41]. In the case of silver, however, a protective dielectric coating must be applied to provide protection against

atmospheric degradation. When reflectivities greater than 99% are required, multilayer dielectric films are necessary[42-44].

In the past, uncoated mirrors of beryllium-copper or molybdenum have exhibited the highest damage thresholds, therefore they have been prefered to low absorption but more easily damaged coated metal mirrors. The lowest absorption metallic coatings were obtained by depositing silver in UHV environment on substrate having surface roughness less than 20Å rms[39,40]. However, such coatings can reduce the damage thresholds of conventionally polished bare metal mirrors by as much as a factor of 2.

The most practical design for high power IR laser mirror applications is the enhanced metallic reflector which consists of a metal layer coated with pairs of alternating, quarter wavelength thick, low and high refractive index dielectrics. In principle this type of mirror can have a reflectivity approaching 100% as have been achieved in pure dielectric multilayers[45]. However, the choice of dielectric layers for use in high power IR laser mirror coatings is very difficult. For optimum performance one wants the largest possible refractive index ratio between the two materials. As shown in the former chapter, the choice of low refractive index materials are limited by the fact that most of the materials with low absorption, such as alkali-halides, have poor physical properties. The choice of high refractive index materials is also limited by the fact that the highest index materials, such as Ge, are semiconductors with small bandgaps.

5. Damage Thresholds for High Power IR Mirrors.

Hughes Research Laboratories have conducted continuous damage experiments for high power IR mirrors. At the 1972 Damage Symposium, Wang, et. al. reported the measurements of damage threshold values of various substrate (Mo, Cu, Ni quartz, etc), metal films (Au, Ag and Cu) and dielectric coated mirrors by using a multimode, pulsed CO_2 laser. The mirror samples were exposed to 10.6μm pulses of 1 to 10μ sec duration with energy fluxes of up to 200 J/cm^2. Their results are shown in Table 8[46]. For uncoated metal mirrors, Cu or Mo had the highest damage threshold values because of their high thermal conductivities. Copper was observed to fail through localized melting and oxidation which resulted in noticeable discolorations and enhanced diffused scattering.

Since the absorption coefficient of thin films of Cu or Ag is generally lower than that of simple refractory substrates, improvements in damage resistance might be expected by employing low loss metallic films over a substrate, thus lowering the absorbed energy[47]. However, such coatings did not effectively increase damage thresholds as shown in Table 8. The reasons for this effect is the imperfect surface and coating conditions such as defects and impurities. The copper coatings upon copper substrates exhibited the best resistance to damage. Gold and molybdenum substrates exhibited similar results. The presence of a dielectric overcoating, which allows easier handling and cleaning of metal mirrors, reduces the threshold values moderately.

Table 8

Damage thresholds for various mirrors

substrate	coatings	Absorption %	Damage* threshold (J/cm^2)	Pulse length (μsec)
Cu	none	∿2	>140	10
Mo	none	∿2	>140	2
Electroless Ni	none	8.6	10∿30	1
Cu	sputtered Cu	∿2	>140	10
Cu	vacuum dep.Cu	∿1	∿140	10
Cu	Ag/ThF_4	∿1	40∿70	10
Mo/blaze	Au(50μ)	∿1.5	∿75	10
Mo	vacuum dep.Cu	∿1	75∿140	10
Electroless Ni	Ag	0.7	20-40	2
Quartz	Ag/ThF_4	∿1	∿10	2
Electroless Ni	$Cu/ThF_4/CdTe^{(2)}$	0.5	10	2
Electroless Ni	$Ag/ThF_4/CdTe^{(6)}$	0.2	10	8
Mo	$Cu/ThF_4/CdTe^{(2)}$	0.5	10	10

* ± 30%

They also tested the dielectric enhanced multilayer mirrors which have the potential for the lowest absorption and thus the possibility for very high incident energy fluxes. However, these multilayer mirrors have material limitations stemming from either poor bonding, residual stresses, or thermal expansion induced stress. In addition to these limitations, there is damage by localized pitting due to inhomogeneous thin films. This thin film inhomogeneity mechanism limits performance of this type of mirror to well below the performance of simple metal mirrors. It is expected that removal of inhomogeneous materials from thin films will considerably improve their performance for laser damage. With the provision that the expected low absorption of the dielectric enhanced multilayer mirrors can be maintained uniformly over the surface, the ultimate performance of these mirrors may be far superior to metal reflectors, especially at short pulse-length.

In their next experiment, Wang, et. al.[48] used a pulsed (gain switched) CO_2 laser with controlled transverse modes and TEM00 operation. The pulse length was 0.6μ sec. They investigated the damage susceptibility of bare metal mirrors and $CdTe/ThF_4$, ZnTe/ZnS and $As_2S_3/KC\ell$ dielectric enhanced metal mirrors. They concluded that under their experimental conditions, failure in narrow band gap II-VI semiconductors, such as CdTe or ZnTe, is characterized by avalanche impact ionization at very low radiation levels. Microscopic examination showed that threshold damage was characterized by microcraters, probably due to impurities or other defects. Films characterized by high absorption values failed at low illumination

levels through a cracking and separation of the films, while for low absorption coatings, damage sensitivity was greatly reduced and the failure was characterized by an initial dislocation and subsequent appearance of interference patterns within the films.

In general bare metal mirrors of Cu and Mo damaged at 35 J/cm^2, while narrow band gap II-VI semiconductors like CdTe and ZnTe exhibited damage thresholds of only 1-2 J/cm^2. Conversely, wide band gap dielectrics such as As_2S_3, KCℓ and ThF_4 did not fail until 30-65 J/cm^2 exposure levels were reached. Unlike previously reported results in the multimode measurements, these single mode exposures showed damage levels less than multimode exposures. The absorption coefficients, particularly for coated mirrors, were of utmost importance in controlling the resulting damage levels.

In their most recent experiments, Soileau and Wang investigated the damage thresholds for metal mirrors with various surface treatments. They used the same laser system described previously. Their results are shown in Table 9[49]. They concluded that a significant change in damage thresholds can occur when unconventional substrate and/or coating processes are used, and that it may be possible to produce very low absorption metal mirrors without compromising the catastrophic failure threshold for high flux radiation levels. The dispersion-hardened sputtered copper, the dispersion-hardened sputtered copper coated with rf sputtered silver and the uncoated diamond machined copper mirrors showed the highest damage threshold values. They mentioned that the sputtering coatings behaved as if they were heavily cold worked and also the diamond machined copper showed evidence of

Table 9

Damage thresholds for metal mirrors

substrate	coating	reflectance %	damage threshold J/cm^2
Dispersion hardened sputtered Cu on OFHCCu	none	0.9846	127
	evaporated Ag	0.99±0.002	63
	rf.sputter Ag	0.9879	103
	rf sputter Ag	0.99	63
Diamond machined OFHC Cu	none	0.9908	103
	evaporated Ag	0.99±0.002	<34
OFHC Cu	none	0.9835	34
Mo	none	0.9788	43
BeCu*	none	0.9801	51

* superpolished

cold working.

6. Conclusion

The most promising materials for high power IR laser windows are found among the alkali-halides (KCℓ, KBr, and NaCℓ) strengthened by ion doping, polycrystalline formation, etc., and semiconductors (ZnSe, CdTe, GaAs) produced by high-purity methods.

The most promising mirrors for high power IR laser applications are the dispersion-hardened sputtered Cu, and the sputtered coatings with highly purified thin films.

The use of refined polishing or machining techniques can raise the surface damage thresholds to the bulk damage thresholds.

In thin film coatings, the list of parameters that can influence the damage threshold is very long. Composition, defect concentration, structure, residual stress, scattering, absorption, angle of incidence, and substrate material are some of the factors that may influence the values obtained. In general, narrow band gap semiconductors exhibit very low thresholds, while wide band gap dielectrics often exhibit high damage thresholds.

Bibliography

Laser Induced Damage

1. "Laser Induced Damage in Optical Materials: 1973", A.J. Glass and A.H. Guenther, Eds. NBS Spec. Pub. 387, (U.S. GPO, Washington, D.C., 1974).

2. "Laser Induced Damage in Optical Materials: 1972", A.J. Glass and A.H. Guenther, Eds. NBS Spec. Pub. 372, (U.S. GPO, Washington, D.C., 1973).

3. "Damge in Laser Materials: 1971", A.J. Glass and A.H. Guenther, Eds. NBS Spec. Pub. 356, (U.S. GPO, Washington, D.C., 1972).

High Power IR Laser Window Materials

4. "High Power Infrared Laser Windows", N. Bloemberger, National Materials Avisory Board Pub. NMAB-292, (National Academy of Science, Washington, D.C., 1972).

There are excellent up-to-date articles for High Power IR optical materials which are only available to U.S. Government agencies.

"Conference on High Power Infrared Laser Window Materials", C.A. Pitha, Ed. AFCRL-TR-73-0372 (I) (II), (Air Force Cambridge Research Lab., Bedford, Mass. 1973).

"Third Conference on High Power Infrared Laser Window Materials", C.A. Pitha, H. Posen and A. Armington, Eds. AFCRL-TR-74-0085 (I) (II) (III), (Air Force Cambridge Research Lab., Bedford, Mass., 1974).

Thin Film Optics

5. Thin Film Optical Filter, H.A. MacLeod, (Adam Hilger, London, England, 1969).

6. Thin Film Physics, Vol. 1 - Vol. 6, G. Hass, Ed., (Academic Press, New York, 1963-1971).

References

1. D.W. Fradin, E. Yablonovitch and M. Bass, Appl. Optics, 12, 700, (1973).

2. M. Bass and H.H. Bennett, IEEE J. of Quantum Electronics, QE-8, 338, (1972).

3. A.J. Glass and A.H. Guenther, Appl. Optics, 13, 74, (1974).

4. A.J. Glass and A.H. Guenther, Appl. Optics, 12, 637, (1973).

5. R.R. Austin, R. Michaud, A.H. Guenther, and J. Putman, Appl. Optics, 12, 665, (1973).

6. D.W. Fradin and M.Bass, Appl. Phys. Lett., 22, 157, (1973).

7. L.G. DeShazer, B.E. Newman and K.M. Keung, Appl. Phys. Lett., 23, 607, (1973).

8. N. Bloembergen, Appl. Optics, 12, 661, (1973).

9. R.R. Austin, R.C. Michaud, A.H. Guenther, J.M. Putman and R. Harniman, in Bib. 2, p. 135.

10. D. Milan, R.A. Bradburry and M. Bass, Appl. Phys. Lett., 23, 654, (1973).

11. N.L. Boling and G. Dubé, Appl. Phys. Lett., 23, 658, (1973).

12. C.J. Duther, Appl. Phys. Lett. 24, 5, (1974).

13. R.W. Hopper and D.R. Uhlmann, J. of Appl. Phys., 41, 4023, (1970).

14. M. Sparks and C.J. Duther, J. of Appl. Phys., 44, 3038, (1973).

15. M. Sparks, in Bib. 2, p. 172.

16. M. Sparks and M. Cottis, J. of Appl. Phys. 44, 787, (1973).

17. M. Sparks, J. of Appl. Phys. 42, 5029, (1971).

18. B. Bendow, Appl. Phys. Lett. 23, 133, (1973).

19. B. Bendow and P.D. Gianino, Appl. Optics, 12, 710, (1973).

20. B. Bendow, S.C. Ying and S.P. Yukon, Phys. Rev. B, 8, 1679, (1973).

21. B. Bendow and P.D. Gianio, Appl. Phys. 2, 1,(1973).

22. F. Horrigon, C. Klein, R. Rudko and D. Wilson, Microwave Mag., Laser Tech. Section, 68, (1969).

23. J.R. Jasperse and P.D. Gianino, J. of Appl. Phys. 43, 1686, (1972).

24. N. Bloemberger, in Bib. 4, p. 65 a.

25. P.A. Young, Thin Solid Films, 6, 423, (1970).

26. N. Bloembergen, in Bib. 4, p. 72 a.

27. N. Bloembergen, in Bib. 4, p. 89 a, p. 90 a.

28. J.T. Cox and G. Hass, in Bib. 6, Vol. 2, p. 239, (1964).

29. J.E. Rudisill, M. Branstein and A.J. Brausten, Appl. Optics, 13, 2075, (1974).

30. D.H. Douglas-Hamilton and E.D. Hoag, J. of Optical Soc. America, 64, 36, (1974).

31. J.A. Savage and S. Nielsen, Infrared Phys. 5, 195, (1965).

32. N. Bloembergen, in Bib. 4, p. 99 a.

33. P.A. Miles, D.N. Readey and T. Newbert, AFCRL-TR-73-0758, (U.S. Dept. of Commerce, Springfield, Va. 1974).

34. A.I. Braustein, V. Wang, M. Braustein, R.E. Rudisill and J. Wada, in Bib. 1.

35. J. Pavit, in Bib. 1.

36. H. Posen, J. Bruce, J. Comer and A. Armington, in Bib. 1.

37. S. Holmes, A. Klugman and P. Kratz, Appl. Optics, 12, 1743, (1973).

38. T.T. Saito and L.B. Simmons, Appl. Optics, 13, 2647, (1974).

39. J.M. Bennett and E.J. Ashley, Appl. Optics, 4, 221, (1965).

40. H.E. Bennett, J.M. Bennett, E.J. Ashley and R.J. Motyka, Phys. Rev. 165, 775, (1968).

41. H.E. Bennett and J.M. Bennett, in Bib. 6, Vol. 4, 1, (1967).

42. K.H. Behrndt and D.W. Doughty, J. of Vac. Sci. Tech., 4, 199, (1967).

43. K.H. Behrndt and D.W. Doughty, J. of Vac. Sci. Tech., 3, 264, (1966).

44. D.L. Perry, Appl. Optics, 4, 987, (1965).

45. A.I. Braustein and M. Branstein, J. of Vac. Sci. Tech. 8, 412, (1971).

46. V. Wang, A.I. Braustein, M. Branstein and J. Wada, in Bib. 2, p. 183.

47. H.E. Bennett, in Bib. 3, p. 153.

48. V. Wang, A.I. Braustein, M. Branstein, J.E. Rudisill and J. Wada, in Bib. 1.

49. M.J. Soileau and V. Wang, Appl. Optics, 13, 1286, (1974).